

MOLECULAR DYNAMICS SIMULATION STUDIES OF
TAILORED NANOSTRUCTURED POLYMERS

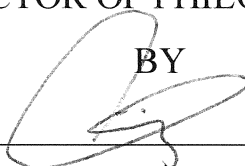
AN ABSTRACT

SUBMITTED ON THE FOURTH DAY OF JUNE 2014
TO THE DEPARTMENT OF CHEMICAL AND BIOMOLECULAR
ENGINEERING
IN PARTIAL FULFILLMENT OF THE REQUIREMENTS
OF THE SCHOOL OF SCIENCE AND ENGINEERING
OF TULANE UNIVERSITY
FOR THE DEGREE

OF

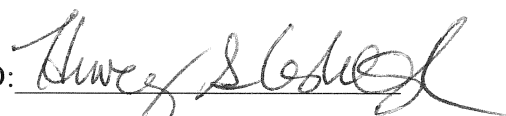
DOCTOR OF PHILOSOPHY

BY



(LIXIN LIU)

APPROVED:

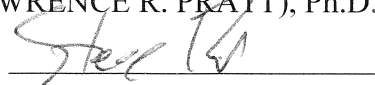


(HENRY S. ASHBAUGH), Ph.D.

DIRECTOR



(LAWRENCE R. PRATT), Ph.D.



(STEVEN W. RICK), Ph.D.



(NOSHIR S. PESIKA), Ph.D.

Abstract

With recent advancements in the synthesis and characterization of polymeric materials, scientists are able to create multi-scale novel polymers with various cases of chemical functionalities, diversified topologies, as well as cross-linking networks. Due to those remarkable achievements, there are a broad range of possible applications of smart polymers in catalysis, in environmental remediation, and especially in drug-delivery. Because of rising interest in developing therapeutic drug binding to specific treating target, polymer chemists are in particular interests in design and engineering the drug delivery materials to be not only bio-compatible, but also to be capable of self-assembly at various in-vivo physiological stimulus. Both experimental and theoretical work indicate that the thermodynamic properties relating to the hydrophobic effect play an important role in determining self-assembly process. At the same time, computational simulation and modeling are powerful instruments to contribute to microscopic thermodynamics' understanding toward self-assembly phenomenon. Along with statistical approaches, constructing empirical model based on simulation results would also help predict for further development of tailored nano-structured materials. My Research mainly focused on investigating physical and chemical characteristics of polymer materials through molecular dynamics simulation and probing the fundamental thermodynamic driving force of self-assembly behavior. We tried to surmount technological obstacles in computational chemistry and build an efficient scheme to

identify the physical and chemical Feature of molecules, to reproduce underlying properties, to understand the origin of thermodynamic signatures, and to speed up current trial and error process in screening new materials.

One of the challenges confronted by MD simulation studies is the force fields' fidelity while simulating hydrophobic hydration's temperature dependence. To address this shortcoming, we re-parameterized a standard simulation potential that permits modeling linear and branched alkenes to reproduce their experimental aqueous solubility at atmospheric pressure based on Trappe UA potential and TIP4P/2005 water model.

As we were improving force field's fidelity, we also performed Replica Exchange MD (REMD) simulations to study the thermal collapse behavior of N-isopropylacryamide (NIPAM) homopolymer in aqueous solution. The characterized radius of gyration change as a mapping of temperature manifested good accordance with experimental outcomes. Paralleling coil-to-globule transition of NIPAM with cold denaturation of proteins, free energy driving thermal collapse can be extracted and fitted with empirical models in determining more thermodynamic properties. Hydrophobic groups' and hydrophilic groups' contributions to thermal-responsive behavior were evaluated respectively to assess the main effect.

With the experience of studying the temperature induced phase transition of polymeric material, we performed REDS2 MD simulations to probe its topologies and resulting prominent solvent-dependencies. Radius of gyration and instantaneous liquid surface analysis addressed the discrepancies between hypothesis based on initial design and reality implied by simulation results. PMF calculations intuitively resembled the polymer's capsulation and release of guest molecule in different environments.

MOLECULAR DYNAMICS SIMULATION STUDIES OF
TAILORED NANOSTRUCTURED POLYMERS

A DISSERTATION

SUBMITTED ON THE FOURTH DAY OF JUNE 2014

TO THE DEPARTMENT OF CHEMICAL AND BIOMOLECULAR
ENGINEERING

IN PARTIAL FULFILLMENT OF THE REQUIREMENTS
OF THE SCHOOL OF SCIENCE AND ENGINEERING

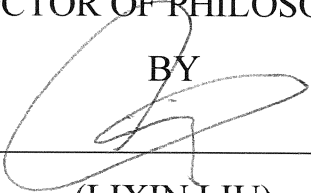
OF TULANE UNIVERSITY

FOR THE DEGREE

OF


DOCTOR OF PHILOSOPHY

BY

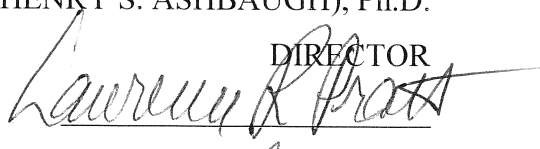


(LIXIN LIU)

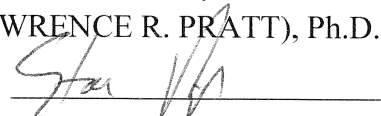
APPROVED:




(HENRY S. ASHBAUGH), Ph.D.

DIRECTOR


(LAWRENCE R. PRATT), Ph.D.



(STEVEN W. RICK), Ph.D.

(NOSHIR S. PESIKA), Ph.D.

©Copyright by Lixin Liu 2014

All Rights Reserved

Acknowledgments

I would like to send my deepest gratitude to my dissertation advisor Dr. Henry S. Ashbaugh. It was my fortune to study thermodynamics and conduct research under his supervision. His insightful suggestion and guidance always lead my work on the right track and accomplished. Most important things I learnt from him are critical thinking about the science, the rigorous attitude toward engineering questions, optimism and sense of humor toward life. Above all, Dr. Ashbaugh's education shapes me from a fresh undergraduate to a doctoral student with specialized in research, which will gain tremendous benefits in my future life.

I would like to send many thanks to Prof. Lawrence R. Pratt. Within joining in his statistical mechanics class, I obtained a new perspective to understand thermodynamics and molecular modeling. Also the discussion with him during the prospectus indeed rectified a lot of my current work and his suggestion to my research plan is inspiring me to investigate more about the correlation between experiment and modeling.

I owe my gratitude to Prof. Steven W. Rick. Within a close collaboration with his groups and extensive discussion with him, I acquired the essential assistance and theoretical knowledge to complete the third project. He is always kind and patient to explain my curiosities and provide inspiring ideas.

I would also like to send many thanks to Prof. Noshir S. Pesika. Not only his suggestion to me provides a lot of novel thinking refreshing my research but also his attitude that follows one's interests to conduct research motivates my work.

By this chance, I would also like to send my thanks to Prof. Scott M. Grayson, who had provided valuable ideas and advice from synthesis perspectives. In addition, I would like to send special thanks to Dr. Sreeja Parameswaran who contributed significantly for QM simulation and shared MD simulation duties. Moreover, I owe my gratitude to her excellent proof and polishing work of our paper and reports.

I would also like to acknowledge research funding support from Louisiana Board of Regent and National Science foundation

During my study at Tulane, I had a good time working together with my research group, including Ashish Sangwai, Pradeep Venkataraman, Piyush Wanjari, Lalit Surampudi, Bin Meng. It was joyful to be among them chatting about life in graduate school, holding discussions about our research, and exchanging scientific thoughts and ideas.

Finally, I owe countless thanks to my mother, my father and my Family members in Qing Huang Dao, whose support in life and heart gave me strength and motivation all these years. Without their deepest love, the completion of this dissertation and my doctoral degree wouldn't be possible.

Table of Contents

Acknowledgement	iii
List of Figures.....	viii
List of Tables.....	xv
Chapter 0.....	1
Introduction.....	1
Chapter 1	11
Optimization of Linear and Branched Alkane Interactions with Water to Simulate Hydrophobic Hydration	11
1.1 Introduction.....	11
1.2 Methodology	19
1.2.1 Simulation Methods	19
1.2.2 Excess Free Energy Calculation	19
1.2.3 Optimization Schemes	22

1.2.4 Calculation of Excess free energy, entropy and enthalpy and Heat Capacity	25
1.2.5 Partial Molar Volume.....	26
1.3 Simulation Results	27
1.4 Concluding Remarks.....	35
Chapter 2.....	37
Probe the Thermo-responsive Behavior of N-isopropylacrylamide (NIPAM).....	37
2.1 Introduction.....	37
2.2 Simulation Methods	43
2.2.1 Basic Simulations Technique.....	43
2.2.2 Details of Analysis	45
2.3 Results and Discussion	45
2.3.1 Radius of Gyration.....	45
2.3.2 Coil-to-globule two-state transition	49
2.3.3 Free energy of coil-to-globule transition	51
2.3.4 Simulation of Polyacrylamide.....	56

2.3.5 Hydrogen bond number	59
2.3.6 Isopropyl group of NIPAM.....	63
2.3 Conclusion	66
Chapter 3	69
Simulations of Linear and Cyclic Amphiphilic Polymers as potential Drug Delivery material	69
3.1 Introduction.....	69
3.2 Replica Exchange Simulation with Dynamical Scaling	78
3.3 Materials and Simulation Methods	84
3.4 Results and Discussion	85
3.4.1 Structure of Linear and Cyclic Polymers in Solvents of Varying Polarity	85
3.4.2 Radii of Gyration	87
3.4.3 Density distribution function	91
3.4.4 Instantaneous Liquid Surface.....	94
3.4.5 Capacity to Deliver Hydrophobic and Hydrophilic Moieties.....	99
3.5 Conclusion	106

Chapter 4	108
Design of Tailored Polymer via Molecular Simulation.	108
4.1 Introduction	108
4.2 Application and Validation of Proposed Design	115
4.2.1 Methods and Materials	115
4.2.2 Structural Results: Radius of Gyration	117
4.2.3 Structural Results: Hydrogen Bonding Effect	120
4.2.4 Structural Results: Density Distribution Function	122
4.2.5 Structural Results: Instantaneous Liquid Surface	124
4.3 Conclusion	126
Chapter 5	129
Conclusion and future work.....	129
List of Reference	134
Biography.....	142

List of Figures

Figure 0.1 A micro-state representation of molecules' Self-Assembly (SA) driven by thermodynamic equilibrium ⁴	3
Figure 0.2 A block copolymer and possible self-assembled materials it can form taken from literature 7.	5
Figure 1.1 Thermodynamic signatures of hydrophobic hydration.....	14
Figure 1.2 Simulating hydrophobic hydration free energy of methane-water system over a temperature range from 250~370K.....	16
Figure 1.3 a Schematic of the temperature dependence of $\mu_{ex}/k_B T$ calculated using the amid equation.....	18
Figure 1.4 Optimization Scheme for obtained preliminary optimal united atoms' Lenard-Jones parameters sets.....	24
Figure 1.5 Hydration free energies of ethane, butane, and neopentane at atmospheric pressure as function of temperature..	29
Figure 1.6. Alkane carbon group/water oxygen radial distribution functions for propane and isobutene at 300 K.....	32

Figure 2.1 Schematic representation of dimensional changes in polymeric solutions at surfaces and interfaces, in polymeric gels and polymer solid resulting from physical or chemical stimuli by Liu et.al ⁴⁵	38
Figure 2.2 Average radius of gyration of NIPAM homopolymer in different length.	47
Figure 2.3 Probability distribution of R_g at selected temperature (280K, 300K, 357K)...	49
Figure 2.4 Probability distribution of various length NIPAM homopolymers as function of temperature	51
Figure 2.5 Free energy of 80mers NIPAM as function of temperature	53
Figure 2.6 Free energies of 40mers NIPAM as function of temperature.....	55
Figure 2.7 Radius of gyration as function of temperature for 80mers PAM and 40mers PAM.....	58
Figure 2.8 Probability distribution of R_g for 80mers PAM (A) and 40mers PAM (B).	59
Figure 2.9 Hydrogen bond number of 80mers NIPAM.....	60
Figure 2.10 hydrogen bond number as function of temperature for 80mers PAM.....	62
Figure 2.11 Fraction of hydrogen bonding as function of temperature	63

Figure 2.12 Radial distribution function of C2-C2 pair at selected temperature.....	66
Figure 3.1 Mechanisms of polymeric micelles encapsulating drug transporting ⁷¹	70
Figure 3.2 Demonstration of Critical Micelle Concentration (CMC) dependence of surfactant.....	71
Figure 3.3 The variety of dendrimer used in biology. A few examples of the types of dendrimer chemistries used in biological applications.	72
Figure 3.4 Chemical structures of the linear and cyclic homopolymer amphiphilic monomers.....	74
Figure 3.5 Schematic illustration of the side chain distribution about the cyclic amphiphilic polymer in water and toluene.....	76
Figure 3.6 the demonstrating system size dependence of probability distribution of potential energy within neighbor thermal ensembles.	79
Figure 3.7 Probability distribution of potential energy for six separating replicas.....	80
Figure 3.8 Left Figure shows seven replicas are required to fill in the potential energy barrier, right figure demonstrated a wide distributed scaling replica large enough to fill in the gap.....	82

Figure 3.9 Replicas Exchange Simulation with Driven Scaling (REDS2) ensures six replicas exchange their information sufficiently.....	83
Figure 3.10 Radius of gyration of alkyl arms as a function of time: blue line represents the data obtained from classical simulation. The red line represents the data obtained from REDS2 simulation.....	84
Figure 3.11 Representative simulation snapshots of the linear and cyclic amphiphilic polymers in water and toluene at 300 K after 20ns.....	87
Figure 3.12 Radius-of-gyration probability distributions for the linear and cyclic polymers and their constituent groups in water (a) and toluene (b) at 300 K.....	90
Figure 3.13 Heavy atom density (not include hydrogen) as function of distance from the cyclic polymer center-of-mass for the polymer backbone, alkyl arm, PEO arm units in water (a), toluene (b), and water/toluene mixed (c) solvents at 300 K.	93
Figure 3.14 A simple demonstration of instantaneous liquid surface construction. Simulated system was coarse-grained into small cells.	95
Figure 3.15 Demonstration of mapping density function surrounding cyclic polymers system (right) through projection at the center of system.....	96
Figure 3.16 Demonstration of distribution of PEO arms' atom for cyclic polymer in water system as function of instantaneous liquid surface distance.....	97

Figure 3.17 Instantaneous solvent interface-side chain heavy atom distance distribution functions for the PEO and alkyl heavy arms for the linear (a) and cyclic (b) polymers in water and toluene at 300 K..	99
Figure 3.18 Schematic demonstration of neighbor list methods.....	101
Figure 3.19 Schematic demonstration of linked-list algorithms.	102
Figure 3.20 Argon excess chemical potential as a function of distance from the cyclic polymer center-of-mass in water and toluene at 300K.	103
Figure 3.21 Argon excess chemical potential as function of distance from the linear polymer center-of-mass in water and toluene at 300K.	104
Figure 3.22 Uptake mixing immiscible solvents by polymer: cyan balls represent heavy atoms of alkyl arms, red balls represent heavy atoms of PEO arms.	106
Figure 4.1 Mean-field phase diagram for conformationally symmetric diblock melts Phase are labeled L (lamellae), H (hexagonal cylinders), Q_{Ia3d} (bicontinuous Ia3d cubic), Q_{Im3m} (bcc spheres), CPS (close-packed spheres), and DIS (disordered) obtained from Matsen and Bates's Unified Weak and Strong Segregation Theory.	113
Figure 4.2 Two strategies potentially to designate polymer in strengthening arms' self-assembly structure.....	114

Figure 4.3 Demonstrating snapshots of modified cyclic polymer in toluene (left) and in water (right).	119
Figure 4.4 The radius-of-gyration distribution of modified cyclic polymer in toluene (above) and water (below)	120
Figure 4.5 Rotating angels of two vectors were analyzed between the last 4 to 6 atoms and last 3 atoms.....	122
Figure 4.6 Heavy atom densities as function of distance from the cyclic polymer center-of-mass for the polymer backbone, alkyl arms, PEO arm unit, Chloride, NH_3^+ in toluene (top), in water (bottom).	124
Figure 4.7 Probability distribution of distance for PEO (blue) and ALK (red): Top results are from cyclic polymer in water solution, bottom results are from cyclic polymer in a toluene solution.	126
Figure 5.1 The hierarchy of modeling methods plot for the range of length and time scales illustrated with the multiscale phenomenology of quantum dots obtained from the heteroepitaxial growth of InAs on GaAs(001).....	131
Figure 5.2 The Radius of Gyration as a function of harmonic potential strength for single chain 7mers polymer.	133

List of Tables

Table 1.1. Cross alkane site/water oxygen Lennard-Jones interaction parameters for the TraPPE-UA and HH-Alkane models.	31
Table 1.2 Solute partial molar volume of various linear and branched alkanes obtained through experiment, TraPPE-UA and HH-Alkane.	34
Table 2.1 Various system's solvent number	44
Table 2.2 OPLS-AA partial charge distribution of monomer atoms	44
Table 2.3 Least square fitting parameter of equation 2.2 used to describe free energy	53
Table 3.1 Various simulated polymer system size.....	85
Table 3.2 Average Radii of Gyration of the Linear and Cyclic Amphiphilic Polymers, Their Backbones, the Hydrophobic Alkyl Arms, and the Hydrophilic PEO Arms in Water and Toluene at 300 K.....	88
Table 4.1 Modified RESP charges of PEO units. Right picture shows the atom number and connections.....	117

Table 4.2 Average Radii of Gyration of the Modified and Original Cyclic Amphiphilic Polymers, Their Backbones, the Hydrophobic Alkyl Arms, and the Hydrophilic PEO Arms in water and Toluene at 300 K	118
---	-----

Chapter 0

Introduction

Improving material performance has been an essential problem since the Stone Age. The dominant materials used to build are even applied to define the culture period (Stone, Iron, and Bronze Ages) which are more than decades. Revolutionary technology development was accelerated after the steam engine was invented. Materials were required to keep stride with the fast-paced industrialization process, motivating chemists' endeavors in acquiring the general rule to guide the success of delivering desired properties as well as discovering suitable composite and synthesis pathways. Albeit most experimental works were established on numerous trial and error efforts, research along guidance of the theory has faced a great deal of successful stories. In the last three decades, silicon material development drove semi-conductor industry's booming subsequently leading research of either soft material or hard material striding into the nano-level¹. Significance of nanotechnology is not limited to special properties displayed in the microscopic perspective. It also relies on validated theoretical concepts especially emerging molecular theories evolved from classical science or engineering fundamentals². Therefore accompanying with the further understanding it is believed that "tailored materials"

would play an important role in constructing and processing the future composite and integrated materials, which achieves great agreement between theory and experiment.

One of the most promising research areas correlating with nanotechnology and molecular level theoretical studies is molecular self-assembly³. Self-assembly is ubiquitous in nature and is a spontaneous process transform of a macroscopic or microscopic structure from disordered state to a hierarchical structure. Such a spontaneous process is driven by thermodynamic equilibrium conversion determined by non-bonded interactions within a nano-structure as Figure 1 demonstrates⁴. In other words, the relationship between reaction coordinate and free energy is a quantitative manifestation of self-assembly driving force. Reaching a minimized state through overcoming the energy barrier has been considered as a priority for completing such a process just like other normal chemical interactions .

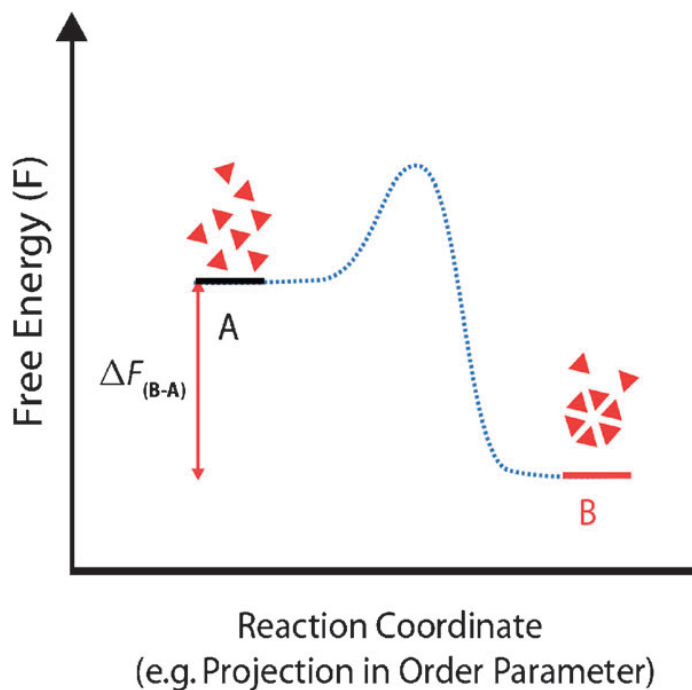


Figure 0.1. A micro-state representation of molecules' Self-Assembly (SA) driven by thermodynamic equilibrium⁴

Like all the other functional materials, self-assembly materials also can be categorized as hard and soft matter. Hard matter's self-assembly weren't able to be considered as Brownian movement, therefore gravitational contributions need to be taken account of, though self-assembly is still a free energy minimization process. Either experimental observation or theoretical observation has confirmed SA thermodynamic significance is originated from the subtle interplay between enthalpy (gravitational and cohesive contributions) and entropy (translational and vibrational contributions) in self-assembly actually thus ultimately determining the phase transition of the hard material such as granular crystal⁵. Apart from extensive interests of physicists and material scientist in SA

of hard matter, chemical engineering and chemistry research groups have exhibited more interests in the soft matter including, polymers, proteins, DNA, lipid membranes, etc. The complexity of quantifying self-assembly related properties is enhanced for soft matter which is not only due to various chemistries of carbohydrates but also due to the high flexibility of architectures built upon weak and isotropic interactions, generally subjected to the phase segregation under solvating in incompatible solvents. Generally speaking, SA soft materials are more like liquid without strong long-range interaction and local symmetry with having ubiquitous presence in nature and many applications. Bilayers are commonly found in cells and organisms for transportation or sieving of ions and electrolytes⁶. Vesicles and micelles are constituted of amphiphiles and have potential applications including drug/gene delivery, nano-particle carrier, environment-friendly detergent used in daily health care, and surfactants used in oil-industry to alleviate corrosion of metals. Moreover, my Ph.D. studies focus on another impacting category of SA materials: the polymeric materials with amphiphilic characters which are known to form a wide variety of self-assembled architectures as Figure h 2 indicates⁷. A typical example which has been widely studied is the self-assembly of block co-polymer driven by the immiscibility of the incompatible blocks. Three key aspects are ascribed to affect the macroscopic behavior of self-assembly of polymers: chemical composition, molecular

architecture (single molecular chain) and super molecular architecture (multiple polymer chains' organization).

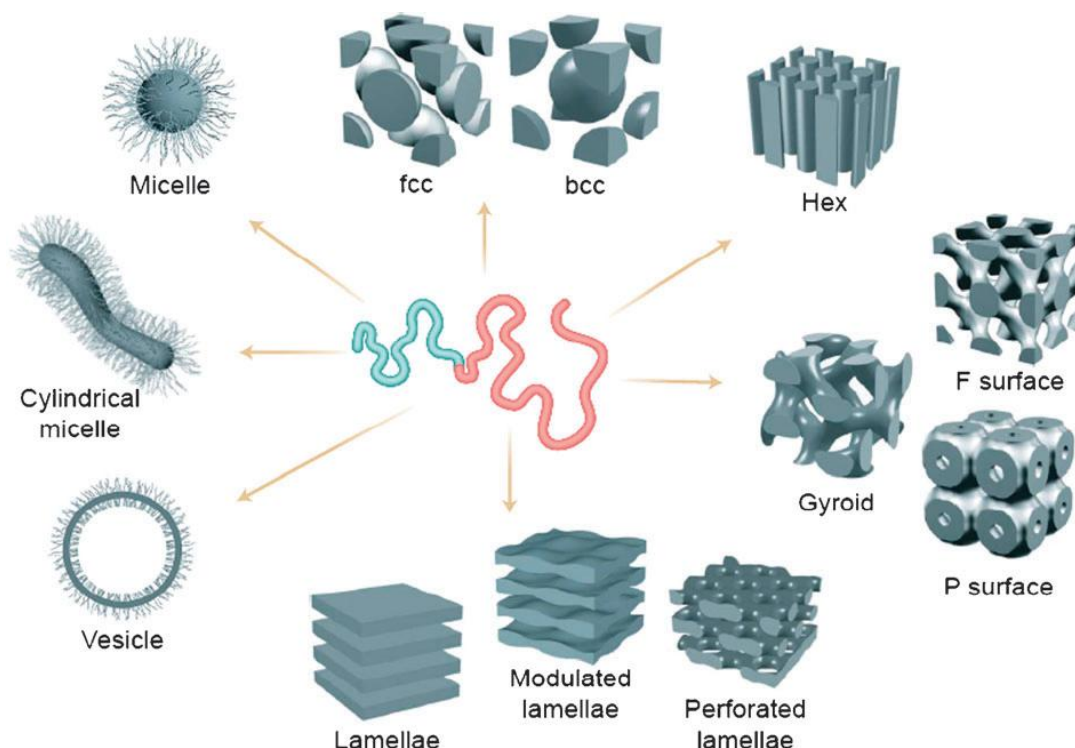


Figure 0.2 A block copolymer and possible self-assembled materials it can form taken from literature 7.

As development of high-resolution microscopy and sophisticated methods harnessed by scientists, experimental studies have ceaselessly discovered novel self-assembly polymeric materials. However, due to the limitation of the time recording and observational scope, current research technique can't satisfy the curiosity intended to probe molecular details. On the other hand, conventional models and theoretical works were established from classical methodologies and analytical solutions. The bridge between theoretical studies and experimental work has not been successfully built until

computational simulation emerging as long as computer science and technology advancing. Computers will readily perform repeated and time-consuming mathematical calculation efficiently. What's more, updating algorithms actually provide strong support for large-scale simulation and modeling. Among various methodologies, Monte Carlo simulation (MC) and Molecular Dynamics (MD) Simulation are both most widely accepted tools. Monte Carlo simulation was accomplished through random walking scheme and comparing the current move with the previous move under acceptance defined by the Boltzmann distribution ($P = \exp(-\Delta U_{\text{potential}})$). Typically MC techniques such as molecule docking⁸ and Simulated Annealing⁹ were generally applied into studies of protein folding or Drug-Ligand binding though it's not an explicit description of system for most cases. Contemporarily Molecular Dynamic Simulation was invented to provide validation of liquid theoretical equations which is used to be solved through numerical approximation. The first proper MD simulation was reported in 1956 by Alder and Wainwright at livermore¹⁰², who studied the dynamics of an assembly of hard spheres. The first MD simulation of a model for a more realistic material was described in 1959 by the group led by Vineyard at Brookhaven, who simulated radiation damage in crystalline Cooper. Eventually the first MD simulation of a real liquid (argon) was reported in 1964 by Rahman at Argonne¹⁰. Since then Molecular dynamics simulation

was widely accepted as a powerful tool to study the solution system. Whereas there's any hardly change for the basic algorithm for MD simulation.

More or less an MD simulation shared a lot of common features with real-experiment.

We select a model system consisting of N particles and solve Newton's equations of motion for this system until it reaches an equilibrium state. Simulation produced atoms' positions (potential energy) and momentum information (kinetic energy) along the time advancing (dynamically). Sufficient simulated time will ensure an observable quantity average over many fluctuations¹⁰³. Basically, expect the quantum effect determining material (radiated element or heavy noble gas); MD simulation took advantage of its simplicity of its algorithm and flexibility to exchange information for parallel computing implementation to enable studies for the large-scale macromolecule solution system's thermophysical properties. Especially in chemical engineering field, thermodynamics is always considered as one of the three fundamentals. A large number of analytical models to describe a pure substance or mixture were developed within experimental measuring. To extend further understanding of Bulk properties, Statistical Mechanics was introduced as a language of translating microscopic or instantaneous information derived from MD simulation to a numerical counterpart of experimental measurement. Specifically, statistical weight of Boltzmann energetic state usually is quantified through the partition function of potential energy which is usually derived based on instant momentum and

configuration. Integration of partition function will produce thermal ensemble at specific condition, such as a canonical ensemble (N, V, T), isothermal-isobaric ensemble (N, P, T) or grand canonical ensemble (μ , N, T). The ensemble average A value can be estimated like following equation indicating,

$$\langle A \rangle = \frac{\sum_i \exp\left(-\frac{H_i}{k_B T}\right) A(p^N, q^N) dp^N dq^N}{\sum_j \exp\left(-\frac{H_j}{k_B T}\right) dp^N dq^N} \quad (0.1)$$

In terms Classical Quantum Mechanics, H_i (Hamiltonian) usually consisted two parts: the kinetic part and the potential energy part denoted in the following equation,

$$H_i = K_i(P^i) + V_N(q^i) \quad (0.2)$$

Correspondingly, the thermal average is also dependent of momentum p and position q which is usually denoted as $A(p^N, q^N)$. Incorporating with statistical mechanics, fluid modeling and thermophysical properties with computer simulation implemented either from integration of motion equation (MD) or random sampling data (MC) surely unveiled the molecular origin of thermodynamics. In addition, along such validated statistic mechanics approach an empirical model constructed based on simulation results would also assign prediction for untouched state and probe uncertain properties, implying significance for further development of tailored nano-structured material. Using simulation results to express validated statistical mechanics theory in investigating

polymer system, several groups and researchers have made exciting advances. Dickman and Hall¹¹ applied well-known Flory-Huggins approach to develop a accurate equation of state describing fluids composed of chain molecules. Monte Carlo Simulation techniques were used to reproduce hard-sphere's chain association configuration and contribute consistent results with several statistical mechanics theories. Ghonasgi and Chapman have also conducted studies of modeling chain fluid (polymer fluidic state) with the Statistical Associated Fluid Theory (SAFT) equation of state. The agreement of molecular simulation and theory prediction consolidated approximation of pair correlation function to the radial distribution function for a fluid of sphere¹². Ashbaugh and Paulaitis examined the potential origin of the LCST behavior of Poly (ethylene oxide) in aqueous solution by applying the information theory to study the monomer group of PEO. Supported by Flory-Huggins theory and Canonical Ensemble Monte Carlo Simulation, main contribution from hydrophobic interaction and less substantial contribution from ether group were validated to lead underlying LCST behavior of PEO through decomposing of excess chemical potential¹³. Whereas MD simulations were seldom used for polymer solution modeling even though both atomistic and coarse-grained dynamic simulations were proved to be a quite successful technique in modeling biomolecular system such as protein, or bioassemblies such as lipid layer. On the other hand, Polymer systems' self assembly triggered either by pressure, temperature,

ions' attraction (salt effect) or complex blending with other hydrophobic moieties required high amount of molecular-level investigation such as their hydrogen bonding networks, Van Der Waals force contribution, long-range electrostatic interaction etc. Molecular Dynamics Simulation earns a winning point comparing with other simulation methods due to its recognition of molecular motion in angstrom-level detail and femto-second resolution. Continuing developments of molecular force fields for various atom types made MD simulation readily arranged. Implementation of parallel computing algorithms made large system simulation feasibly achieved. Therefore, to extend MD simulation's application in polymer system and corresponding theoretical development, my research mainly focused on investigating physical and chemical features of polymer materials in polar or non-polar environments under various ensembles. Starting from the force fields' optimization of simple alkane to complex amphiphilic cyclic polymer structure, my studies have unfolded a progressing scheme to understand the self-assembly phenomenon from the chemical origin of its associated behavior in polymer true solution. We attempted to overcome technical obstacles in computational chemistry and build a well-organized plan that to identify the physical and chemical features of molecules, to reproduce underlying properties, to understand the origin of the thermodynamic signatures, to speed up current trial and error process in screening new materials.

Chapter 1

Optimization of Linear and Branched Alkane Interactions with Water to Simulate Hydrophobic Hydration

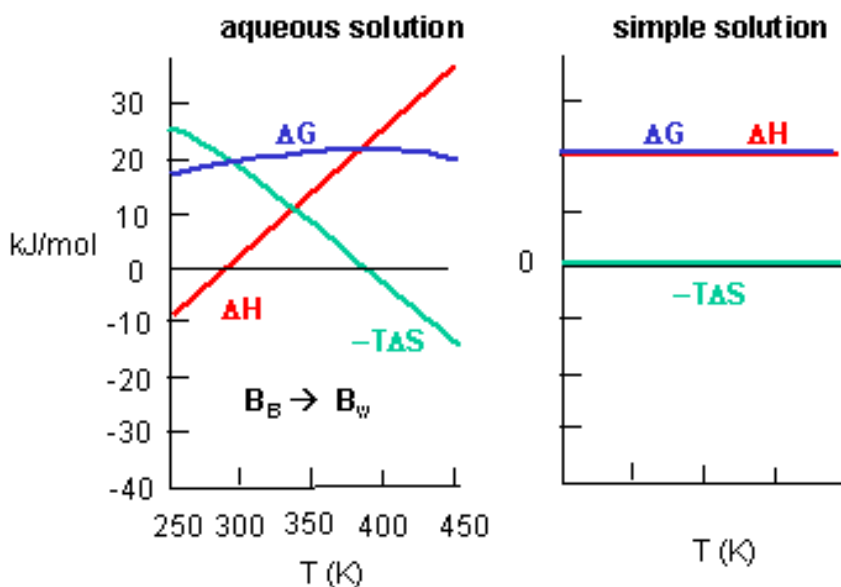
1.1 Introduction

Oil and water doesn't mix is a both well-known and refreshing topic discussed extensively by chemical engineering and chemistry community. What make such phenomenon more important is that meager solubility of hydrocarbon in water has been widely believed to be the driving force of general self-assembly process such as protein folding (sometimes protein denaturation) surfactants micellization¹⁴ or membranes and complex mesophases in surfactant solutions. Subsequently, such uncomfortable coexistence phenomenon is usually denoted as hydrophobic effect. Like all the thermodynamic definition, both intensive and extensive physical properties are correlated with the free energy of hydrophobic interaction. Temperature dependencies to the underlying thermodynamic contributions to the free energy is always an interesting research theme. Meanwhile modeling

temperature dependences of hydrophobic hydration is always considered as a research significance with complexities. Hummer et.al developed information theory based on simplest hard-sphere model and integrated temperature and cavity density function into the free energy interpretation.^{15, 16} Application of information theory model provided a quantitative understanding of hydrophobic effects both on temperature and pressure¹⁷. Proximity approximation in predicting of water structure around hydrophobic solutes was main contribution to the temperature driven exclusion of water molecules and it's also potentially extending its prediction of water structure and hydration thermodynamic properties from simple carbon to more complex clusters of hydrophobic solutes¹⁸. In terms of simulation aspect, Paschek examined five different water models to investigate the temperature dependence on hydrophobic hydration of non-polar solutes and they concluded density effect was an important requirement for water model to describe hydrophobic effect correctly¹⁹. Within emerging of TIP4P-EW water model, Krouskop further confirmed Paschek's posited by hypothesis that modeling correct density resulted in correctly modeling the solubility of hydrophobic solutes²⁰. Guard and Ashbaugh have investigated the temperature dependence of hydrophobic hydration with single-site HGS water model. The most important factor determining hydration thermodynamics of hydrophobic solutes was found out to be the temperature dependence of the bulk density of water²¹. Pascheck consecutively studied the solute-polarization affected the

temperature dependence of hydrophobic hydration. They concluded that solute polarizability was affecting solvation entropy more strongly than solvation enthalpy and such increasing entropic effects were due to locally increased solute-water interaction causing hydrophobic solutes to penetrate water solvation-cage more strongly, thus perturbing the hydrophobic solvation shell²². Based on previous work, a lot of other studies also were involved in testing the fidelity of model and searching the feasible scheme to solve inconsistency between simulation and experimental results²³. Speaking of the thermodynamic fundamentals, at ambient temperature the dissolution of hydrophobic species from the gas phase is favored by negative enthalpic contributions to the free energy, but these are overwhelmed by unfavorable negative entropic contributions. At higher temperatures hydration is entropically favored, but disfavored by dominant positive enthalpy. The changing roles of enthalpy and entropy in opposing non-polar solute hydration are indicative of a large, positive heat capacity increment. Collectively, these thermodynamic properties have been identified as signatures of hydrophobic hydration. One example is indicated by Figure 1.1. Benzene was transferred from simple solution to an aqueous solution accompanying with the prominent thermodynamic properties varying: Free energy increased parabolically and reached a maxim peak at about 350K. The enthalpic part increased from the negative side to the

positive side, however negative entropic part oppositely descended from positive to negative.



Privalov and Gill (1988) Adv. Protein Chem. 39, 191

Figure 1.1 Thermodynamic signatures of hydrophobic hydration. Thermodynamic features for a simple solution of benzene is insensitive of temperature, but benzene in aqueous solution manifest temperature dependence after transfer solutes from pure solution to water.

Flowing from information theory analysis of the dissolution of non-interacting, excluded volume solutes, simulation and modeling studies have shown the characteristic thermodynamic signatures of hydrophobic hydration arise in large part from anomalous equation-of-state properties of liquid water at ambient pressure, such as the temperature of maximum density just above melting and the comparatively temperature insensitive

isothermal compressibility of water relative to organic solvents¹⁵. Since each simulation model reproduces the density of water along the saturation curve with varying degrees of success, it has been concluded that the greater the fidelity of the water model to the experimental equation-of-state is the more accurate the description of hydrophobic hydration is. Of the available classical water models which treat water as a rigid body with partial charges and Lennard-Jones (LJ) groups distributed among a collection of interacting sites, the TIP4P/2005 water model has been found to provide both the most accurate description of liquid water at ambient pressures²⁴. Ashbaugh et.al²⁵ have assessed different water model's fidelity to simulate hydrophobic hydration of united atom methane in aqueous solution and conclude the TIP4P/2005 water model reproduced the most accurate description of hydrophobic hydration's temperature dependence closely followed in accuracy by TIP4P-Ew model²⁶ as Figure 1.2 shows. At ambient conditions, however, non-polarizable simulations of simple non-polar gas hydration tend to under-predict their aqueous solubility. The discrepancy will reduce the simulation's accuracy in describing larger bio-polymer system mainly consisted of atoms, motivating us to constantly update and develop the simulated system. Taking polarization effects into account, either through a re-parameterization of solute/water LJ interactions²⁷ or inclusion of solute polarizability can correct the discrepancies^{22 23}.

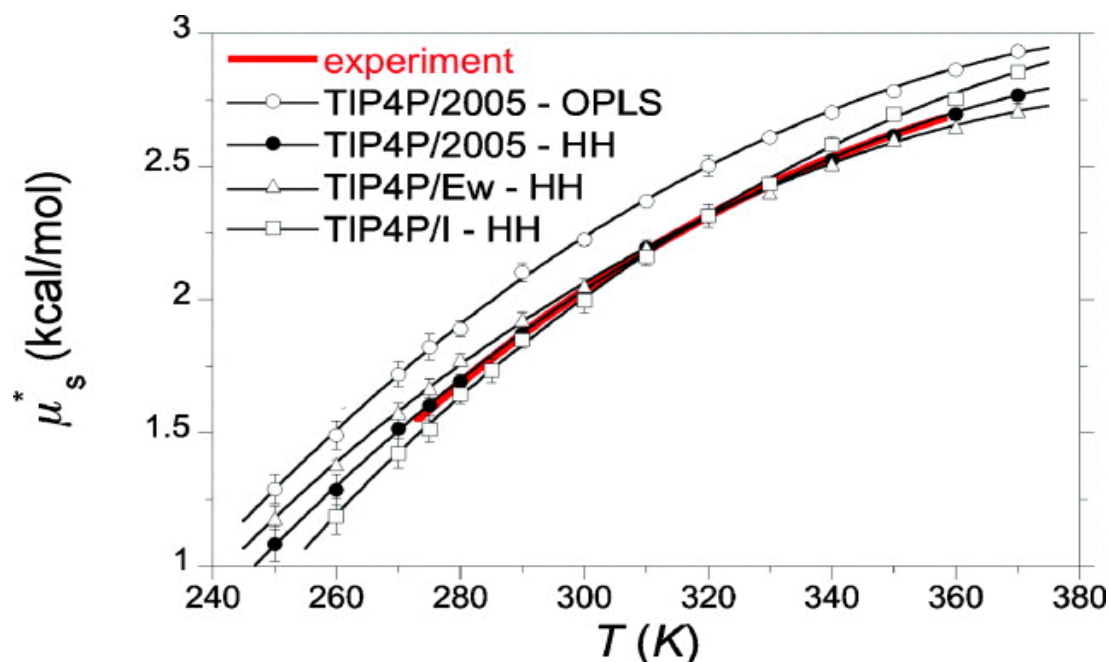


Figure 1.2 Simulating hydrophobic hydration free energy of methane-water system over a temperature range from 250~370K. Comparative results suggest TIP4P/2005 water model provide the best description of experiment value among several TIP4P water models by Ashbaugh et.al²⁶.

More specifically, free energy can be correlated with density function $\rho(T, VP)$, or in other word the equation-of-state, through perturbation theory. As Figure 1.3 shows, Introducing a weak-attractive terms C to the perturbation equation of hard sphere fluids will shift the solubility curve downwards vertically and reach a minimum at higher temperature, in which C is a positive value depending on the strengths of solute-water interaction. Therefore, one of the research focuses to resolve the discrepancy between experimental value and theoretical prediction is turning the variation of interacting parameters within the solute and water. Molecular simulation is extensively considered as

a powerful tool to provide accurate validation for molecular theoretical studies such as Statistical Associating Fluid Theory (SAFT)²⁸ or Information Theory describing hydrophobic effect¹⁶. However, simulation results of the dissolution of the normal alkanes at ambient conditions tended to under-predict their aqueous solubility. It may be anticipated that, similar to simple, non-polar gases, the polarization effect between water and the hydrocarbon are unaccounted for in these simulations. To address this shortcoming, we reparameterize a standard simulation potential that permits modeling any of the linear and branched alkanes. TIP4P/2005 water model was adopted in this development work in force field because of its high fidelity of describing liquid water's melting curve. In addition, we used the transferable potentials for phase equilibria united-atom model (TraPPE-UA)²⁹ to describe non-polar substance. Because TraPPE potential have been testified to be a well-developed model in predicting vapor-liquid phase diagrams for pure alkanes over a wide temperature range. Very few studies so far combined these two force fields which respectively, have been regarded as best models in reproducing the pure component behavior. Hereby we applied TIP4P/2005 and TraPPE-UA model to study the temperature dependence of hydrocarbons' solubilities. In which solubilities were calculated over a broad temperature range permitting a simultaneous analysis of the enthalpic, entropic, and heat capacity contributions to the hydration free energies that are characteristic of hydrophobic hydration. Also, we

optimized Lenard-Jones interacts site's parameters to pull down the difference between simulation results and experimental results over a range of temperature (270K ~ 370K). Within analysis of partial molar volume and radial distribution functions, the optimized parameters sets are validated in describing rightful water structure around hydrophobic solutes.

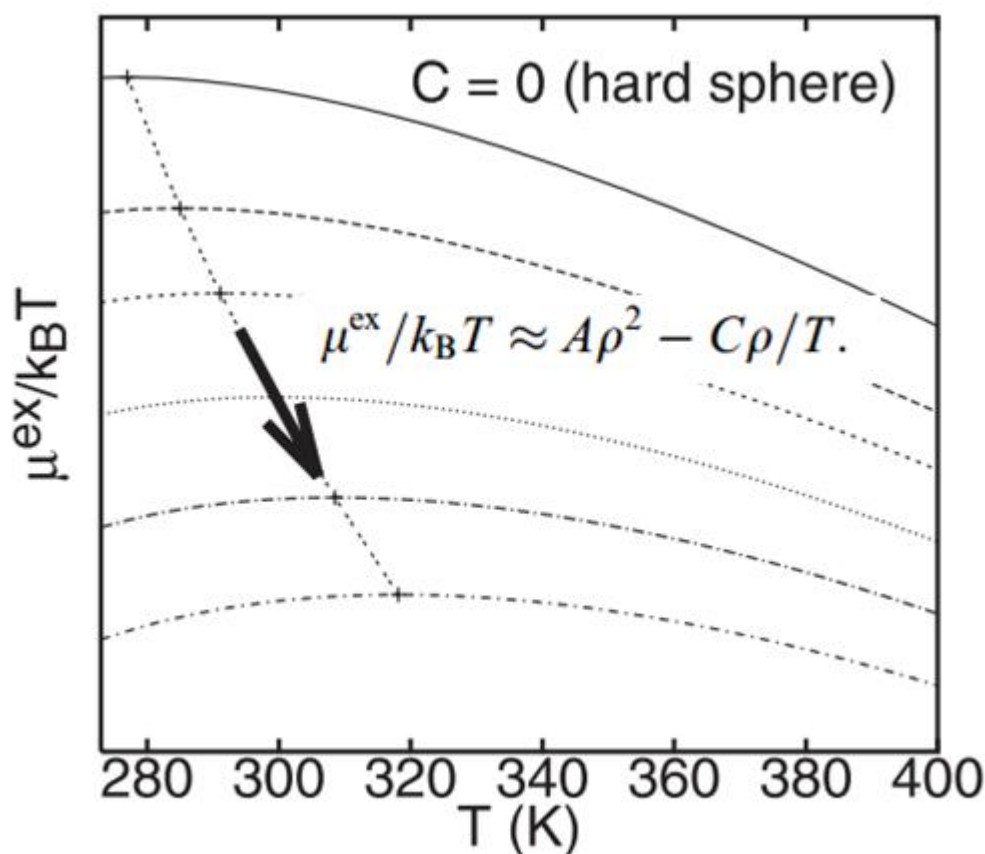


Figure 1.3 a Schematic of the temperature dependence of $\mu^{\text{ex}}/k_B T$ calculated using the amid equation. The $C = 0$ curve on top corresponds to $\rho^2(T)$. A dotted line with thick arrow shows the increase in the solubility minimum temperature with increasing strength C of attractive interactions¹⁷.

1.2 Methodology

1.2.1 Simulation Methods

Alkane hydration simulations were performed using GROMACS 4 molecular dynamics simulation package³⁰. Simulations were conducted in the isothermal isobaric ensemble for a single alkane in a bath of 400 water molecules. Simulations were conducted over a series of temperatures from 270 K to 370 K in 10 K increments at atmospheric pressure. The temperature and pressure were maintained using the Nose-Hoover thermostat³¹ and Parrinello-Rahman barostat³², respectively. A 2fs time step was used to integrate the equation of motion. LJ interactions were evaluated out to 9 Å, and standard long-range corrections were applied to the energy and pressure. Particle mesh Ewald summation³³ was used to evaluate electrostatic interactions. Water was modeled using TIP4P/2005 potential²⁴, which provides one of the most accurate description of water's equations-of-state over the liquid regime at atmospheric pressure of the available classical fixed charge models. The TraPPE-UA potential³⁴, which is optimized to reproduce pure alkane phase diagrams was used as the basis to simulate linear and branched alkanes. The linear constraint solver (LINCS) algorithm³⁵ was used to constrain the geometry of water and fix the carbon-carbon bond lengths.

1.2.2 Excess Free Energy Calculation

Basically when we talked about simulated hydrophobic specie's solubility, it usually referred the concentration of solute at infinite dilution in aqueous (aq) solution. The excess free energy is related to the concentration ratio of solute at infinite dilution in aqueous (aq) solution relative to that in an ideal gas (ig) at equivalent temperatures and pressure. Such ratio is usually defined as Ostwald coefficient and the relationship is described in following equation 1.1:

$$\frac{\rho_s(aq)}{\rho_s(ig)} = \exp(-\beta\mu_s^{ex}) \quad (1.1)$$

where $\rho_s(x)$ is the solute concentration in phase x , and $\beta^{-1}=kT$ is the product of Boltzmann's constant and the temperature. Thus, the excess hydration free energy, which reflects intermolecular interactions in solution, is central to resolving aqueous solubility of alkane at infinite dilution were determined using thermodynamic integration as implemented in GROMACS³⁰. In this approach, the free energy is determined as the work associated with growing the solute into solution via a coupling parameter, λ , which is a slowly growing parameter to turn on solute/solvent interaction. Specifically perturbation parameter λ is embedded into the Lenard-Jones inter-molecular potential calculating algorithms. The derivative of the hydration free energy with respect to the coupling parameter was evaluated from simulation at values of λ from 0.0 (uncoupled) to 1.0 (fully coupled) in increments of 0.1 according to equation 1.2, at where H is the

system Hamiltonian and the angled brackets $\langle \dots \rangle_{N,P,T,\lambda}$ indicate the isothermal-isobaric simulation average at fixed λ .

$$\frac{\partial \mu^{ex}}{\partial \lambda} = \left\langle \frac{\partial H}{\partial \lambda} \right\rangle_{N,P,T,\lambda} \quad (1.2)$$

Average at each value of λ was performed over 10ns after 1 ns of equilibration. The excess hydration free energy was subsequently determined by integration of $\partial \mu_s^{ex} / \partial \lambda$ using Simpson's rule. Alkane LJ interactions were coupled to the solvent using the "soft core" method implemented in GROMACS to circumvent the singularity introduced into the free energy integral by linear potential scaling³⁶.

Alkane site-water interactions were optimized to minimize the mean square difference between simulation and experimental hydration free energies of methane, ethane, propane, butane, isobutane, and neopentane over a range of temperatures at atmospheric pressure. The selected alkanes include the complete set of carbon interaction sites (i.e, CH₄, CH₃, CH₂, CH and C) necessary to describe any linear or branched alkane. As noted above, the TraPPE-UA model served as the basis for optimizing cross alkane-water interactions for reproducing the hydration free energy. Cross solute site-water interactions between TraPPE-UA alkanes and TIP4P/2005 water were determined using Lorentz-Berthelot combining rules for the LJ diameter and well depths according to following equations⁸⁶:

$$\sigma_{iw}^{TraPPE} = \frac{\sigma_{ii}^{Trap} + \sigma_{ww}}{2} \quad (1.3)$$

$$\varepsilon_{iw}^{TraPPE} = \frac{\varepsilon_{ii}^{TraPPE} + \varepsilon_{ww}}{2} \quad (1.4)$$

1.2.3 Optimization Schemes

To begin the optimization process, simulations were performed using σ_{iw}^{TraPPE} and $\varepsilon_{iw}^{TraPPE}$ to determine the excess free energy as function of temperature. Previous studies have shown that methane-water interaction's temperature dependence can be reproduced whereas with obvious variation from experimental value³⁷, we also derived coherent results for ethane, propane, butane and neopentane that excess free energy are uniformly higher than experimental value. Therefore a preliminary optimization will focus on the adjustment of non-bond Lenard-Jones parameter sets σ_{iw}^{TraPPE} and $\varepsilon_{iw}^{TraPPE}$. Intuitively there are vast combinations of these two-parameter subsequently resulting mainly two challenges: 1. How to test the pre-optimized parameter without running simulation time by time? 2. How to search reasonable parameter with physical underlying meaning?

To tackle the first emerging problem, a preliminary optimization was performed by modification of the alkane site interactions with water by evaluating the hydration free energy differences between that for modified σ'_{iw} and ε'_{iw} and those determined using σ_{iw}^{TraPPE} and $\varepsilon_{iw}^{TraPPE}$. The perturbation formula⁸⁷,

$$\Delta\mu_s^{ex} = -kT \ln \langle \exp \left[-\beta [H_{optimized} - H_{TraPPE}] \right] \rangle_{TraPPE} \quad (1.5)$$

was used to estimate the hydration free energies of the modified interaction model and subsequently minimize the root mean square difference with experiment. In this expression, the Hamiltonian H_x is evaluated for $x = \text{optimized or TraPPE-UA interactions}$ over configurations generated for the fully coupled TraPPE-UA alkane in water $\langle \dots \rangle_{\text{TraPPE}}$. Using such formula, we can directly obtain an approximate difference between modified parameters and original TraPPE parameters and then further compare with the experimental value until they reached consistencies preliminarily over initial setting temperature range. Even though there still exists slight configurational variance between new parameters and TraPPE, single molecule's contribution to the fluctuation only deliver minor influence of a spacious box of 400 water molecules. In addition, after generating preliminary optimal value of σ'_{iw} and ϵ'_{iw} , free energies were reevaluated from simulations with the new parameter sets to affirm the optimization procedure described above and slight modifications were made if necessary to tune the model's accuracy. Figure 1.4 indicated the scheme used by us.

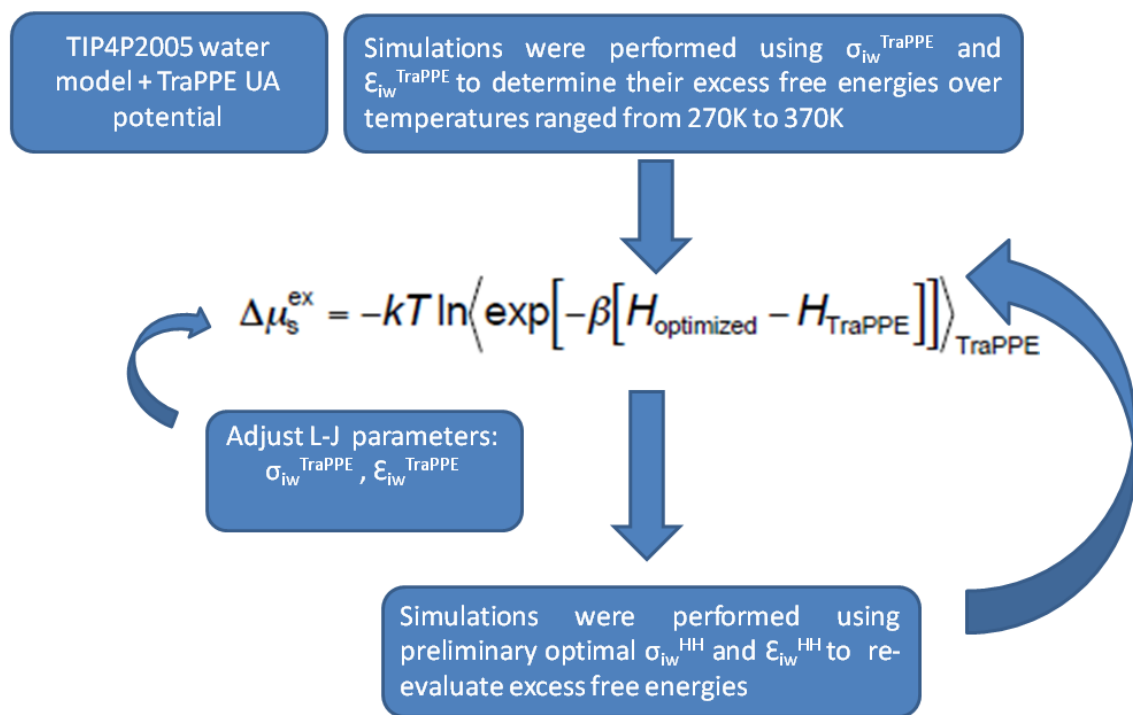


Figure 1.4 Optimization Scheme for the obtained preliminary optimal united atoms' Lenard-Jones parameters sets.

Secondly, the searching scale of optimal parameters sets should be narrowed down and should be in accordance with chemo-physical properties especially water structure. More challengingly, a simultaneous fitting of LJ diameters and well depths of the cross alone site/water interactions is complicated by the fact that the root mean square deviation between simulation and experiment is shallow in the vicinity of the optimal fit, potentially leading to physically unrealistic interaction parameters. Specifically, small changes in the solute interaction site diameter of a few percent can have a significantly larger effect on the solute partial molar volume since the excluded volume is expected to

increase as the diameter cubed. Furthermore, it has been observed from previous simulations of simple non-polar gas hydration that the LJ well depth is the most sensitive variable for obtaining agreement with experiment. Therefore, to minimize changes in the solute excluded volume, we constrain our fitting by varying the LJ well depth while fixing the thermal radius r_{iw}^{therm} , of each site at 300 K to that obtained for the unmodified TraPPE-UA interactions. The thermal radius is defined as the intermolecular separation at which the repulsive Week-Chandler-Anderson³⁸ portion of the LJ potential is equal to kT and is given as³⁹

$$r_{iw}^{therm} = \sigma_{iw} \left[\frac{2}{1 + \sqrt{\frac{kT}{\epsilon_{iw}}}} \right]^{1/6} = \sigma_{iw}^{TraPPE} \left[\frac{2}{1 + \sqrt{\frac{kT}{\epsilon_{iw}^{TraPPE}}}} \right]^{1/6} \quad (1.6)$$

By fixing the thermal radii, optimal fits are obtained within the statistical accuracy of the simulations while maintaining physically reasonable sizes for each site. The bond lengths, bond bending interactions, and dihedral interactions were fixed to that of the unmodified TraPPE-UA potential. The appropriate results will listed in the following chapters.

1.2.4 Calculation of Excess Free Energy, Entropy and Enthalpy and Heat Capacity

The excess hydration thermodynamic contributions to the hydration free energy can be extracted from our simulation results by assuming the hydration heat capacity increment

($c_s^{ex} = \delta h_s^{ex} / \delta T |_P = T \delta s_s^{ex} / \delta T |_P$) is independent of temperature. It follows that the hydration enthalpy, entropy and free energy are

$$h_s^{ex} = h_{s,0}^{ex} + c_s^{ex} (T - T_0) \quad (1.7)$$

$$s_s^{ex} = s_{s,0}^{ex} + c_s^{ex} \ln\left(\frac{T}{T_0}\right) \quad (1.8)$$

$$\mu_s^{ex} = (h_{s,0}^{ex} - T_0 s_{s,0}^{ex}) + (c_s^{ex} - s_{s,0}^{ex}) (T - T_0) - c_s^{ex} T \ln\left(\frac{T}{T_0}\right) \quad (1.9)$$

Respectively, in these expressions, T_0 is an arbitrary reference temperature chosen here to be 300K, while $h_{s,0}^{ex}$ and $s_{s,0}^{ex}$ are the hydration enthalpy and entropy at T_0 . The combination of terms $h_{s,0}^{ex} - T_0 s_{s,0}^{ex}$ corresponds to the hydration free energy at T_0 . Fitting Eq. 1,9 to the simulation free energies provides an excellent description of alkane hydration over the temperature range simulated, and permits us to obtain the three independent variables $h_{s,0}^{ex}$, $s_{s,0}^{ex}$ and c_s^{ex} that characterize the dissolution thermodynamics.

1.2.5 Partial Molar Volume

In addition to the thermodynamic quantities characterizing the temperature dependence of hydration, we have also evaluated the alkane partial molar volumes at infinite dilution, which describe the pressure response using following equation,

$$v_s = \left. \frac{\partial V}{\partial N_s} \right|_{T,P,N} = \left. \frac{\partial (kT \ln \rho_s(aq) + \mu_s^{ex})}{\partial P} \right|_T \quad (1.10)$$

The partial molar volumes at 300 K and atmospheric pressure were determined as the difference in the average volume between a simulation of 400 water molecules and 1 alkane and a simulation of water molecules alone as following equation shows.

$$v_s = V (N_w = 400, N_s = 1) - V (N_w = 400, N_s = 0) \quad (1.11)$$

The simulations with a single alkane were performed for 50ns while that of pure water was conducted for 100ns.

Experimental hydration free energies for methane, ethane, propane, butane and neopentane over temperature range 280 K -350 K were taken from Wihelm et.al⁴⁰. While these authors report free energies for isobutane, they find a negative heat capacity for this solute, in difference to the observed positive values generally accepted as a signature of hydrophobic hydration. We, therefore, substituted the free energies compiled by Plyasunova et al⁴¹ as our optimization target for isobutane over the range 290 K – 310 K. Partial molar volumes for the alkanes at infinite dilution for comparison with simulation were obtained from the database of Plyasunova et.al⁴¹.

1.3 Simulation Results

Representative alkane hydration free energies for ethane, butane, and neopentane along one atmosphere isobar determined from simulation using the TraPPE-UA model are compared to the experiment in Fig. 1. The simulated hydration free energy curves are

consistently shifted upwards relative to experiment, and appear approximately parallel to the experimental curves. This suggests that while the TraPPE-UA model predicts lower aqueous solubilities than experimentally observed, the simulation do capture the temperature dependence of alkane's solubility (Figure 1.5). The hydration free energy's over-prediction by the TraPPE-UA model extends to all the simulated alkanes. As described above, the alkane site/water oxygen interactions were optimized by adjusting the LJ well depth with the thermal radius at 300 K fixed to minimize the root mean square difference between the simulation and experimental hydration free energies over the reported experimental temperature ranges. As shown in Figure 1, the HH-Alkane model provides a significantly improved quantitative description of alkane hydration free energies as a function of temperature. Through fitting the simulated data with equation 1.9, a predictive curve can be drawn smoothly to describe the developing trend around temperature range.

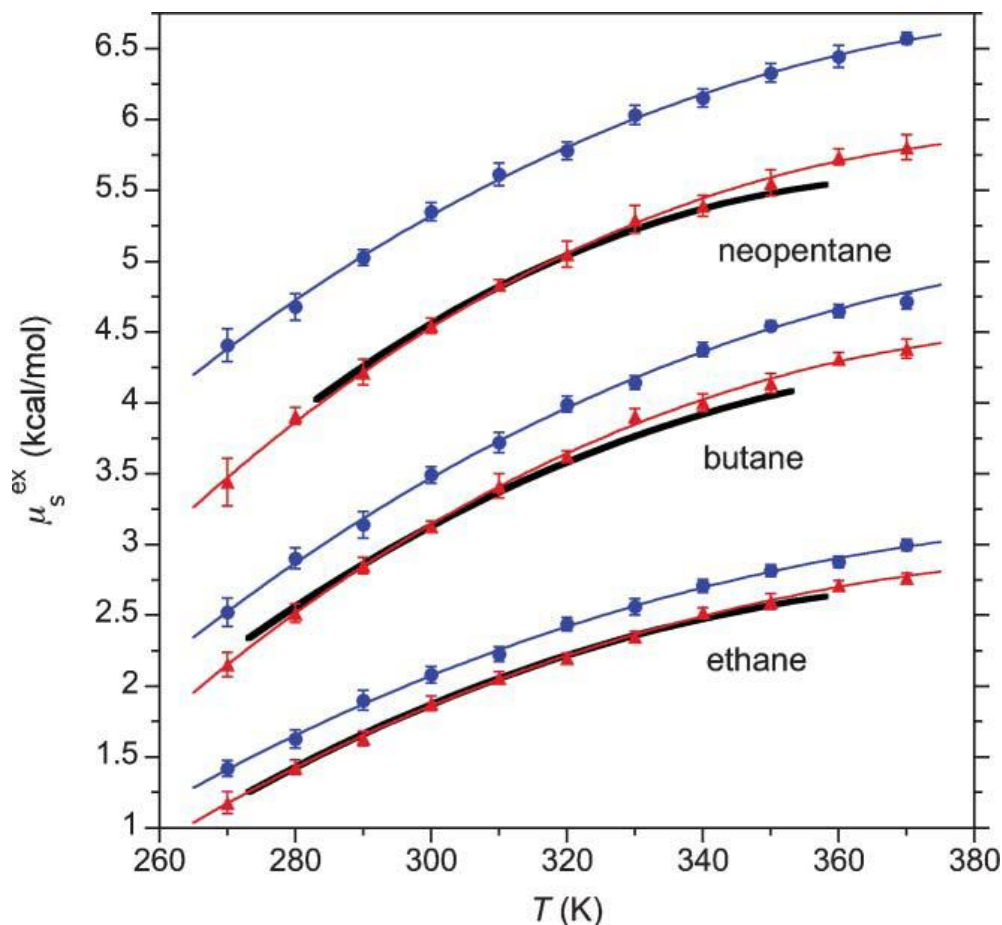


Figure 1.5 Hydration free energies of ethane, butane, and neopentane at atmospheric pressure as function of temperature. For clarity, the hydration free energies of butane and neopentane are shifted up by 1 and 2 kcal/mol, respectively. The blue circles and red triangles correspond to simulation results using the TraPPE-UA and HH-Alkane models, respectively. Error bars indicate one standard deviation. The thin blue and red lines correspond to fits of Eq. 1.9 to the TraPPE-UA and HH-Alkane simulation results, respectively. The thick black line indicates the experimental hydration free energies over the temperature range reported in Ref. 27.

Also the TraPPE and optimized parameter sets between solute and water are reported in the Table 1.1. Respectively ethane was modeled to describe bond parameter and CH3 interacting sites; propane was modeled to describe angle parameter and CH2 interacting

sites; Butane was modeled to supplement verification of dihedral; Neopentane was modeled to contribute C interacting site parameter; As Table 1.1 shows the thermal diameter increased as more hydrogen substituted by pending group . In addition, comparison between HH-Alkane (optimized) and TraPPE-UA specifications, the well-depth parameters perform the major change while the thermal diameters were just tuned slightly. Even though the major change is relative mild, we find the improved agreement of the alkane hydration free energies with experiment was achieved by increasing the cross interaction well depth by $\Delta\epsilon_{iw}/k \approx 3\sim 6$ K. This weak increase in attractive interactions effectively account for the missing polarization interaction between hydrocarbons and water, in agreement with previous simulation studies of noble gas and methane hydration^{19, 22} As indicated by Table 1.1, the constant thermal radius is the basis serving for adjustments of Lenard-Jones parameters.

	$\Sigma_{iw} (\text{\AA})$	$\epsilon_{iw}/R (\text{K})$	$r_{iw}^{\text{therm}} (\text{\AA})$
TraPPE-UA			
CH ₄	3.444	117.4	3.297
CH ₃	3.452	95.57	3.272
CH ₂	3.552	65.48	3.297

CH	3.919	30.53	3.473
C	4.779	6.826	3.824
HH-Alkane			
CH ₄	3.436	123.0	3.297
CH ₃	3.448	98.92	3.272
CH ₂	3.547	67.99	3.297
CH	3.895	33.71	3.473
C	4.614	11.18	3.824

Table 1.1. Cross alkane site/water oxygen Lennard-Jones interaction parameters for the TraPPE-UA and HH-Alkane models. TraPPE-UA/water cross interactions were determined using Lorentz-Berthelot combining rules for the TIP4P/2005 water oxygen. The cross interaction thermal radius at 300 K was determined using Eq. 1.6

As described in methodology part, the HH-Alkane model was optimized to minimize the perturbations of the sizes of the alkane sites. We anticipate that this approach also minimizes perturbations in the pair correlations between water and alkanes. The alkane site/water oxygen radial distribution functions for propane and isobutene at 300 K for the TraPPE-UA and HH-Alkane models are shown in Fig. 1.6. As can be discerned from this figure, the pair correlation perturbations are minimal with the differences between the models comparable to the simulation noise.

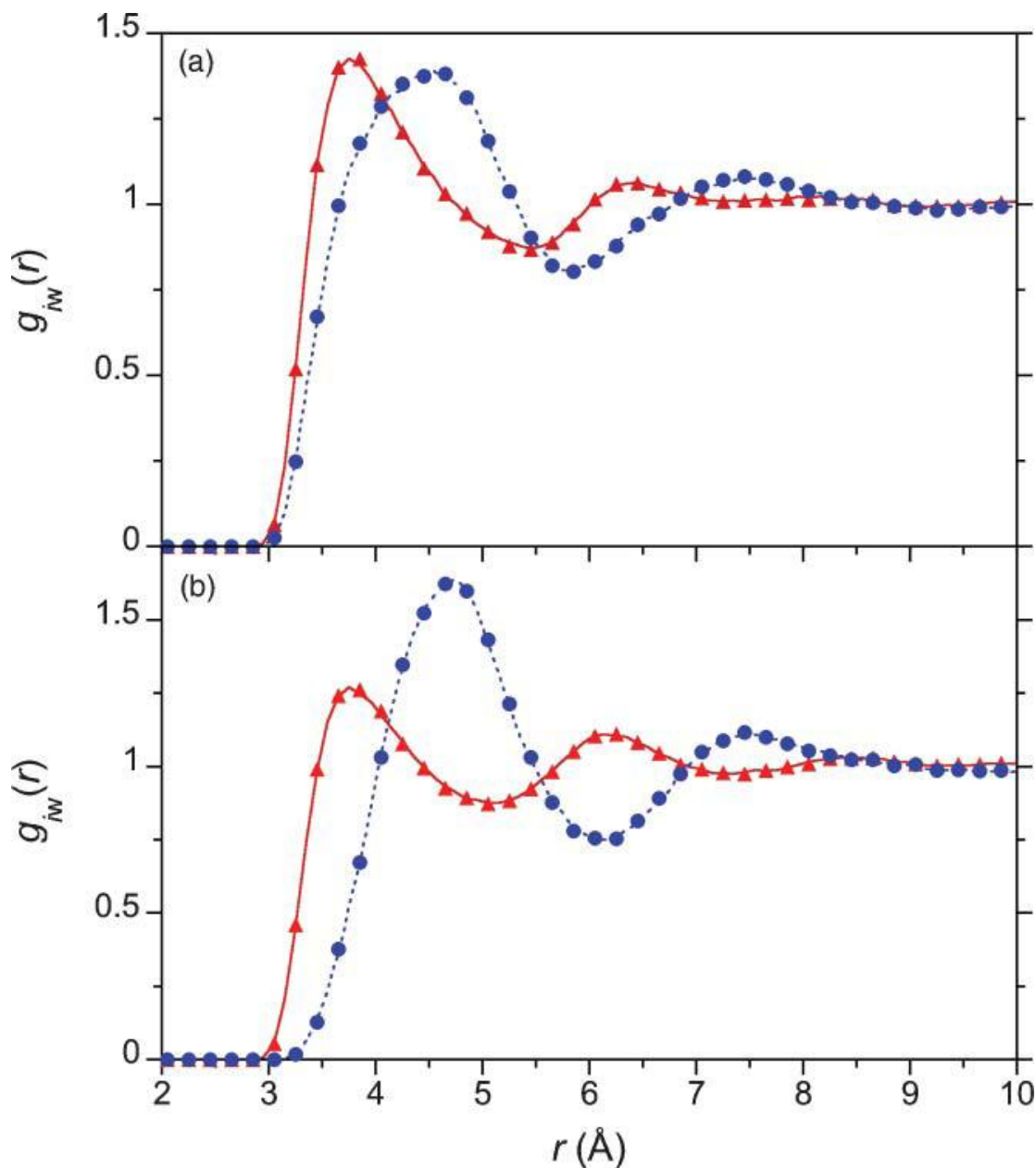


Figure 1.6. Alkane carbon group/water oxygen radial distribution functions for propane and isobutene at 300 K. (a) The distribution functions for propane. The solid red line and red triangles indicate results for the terminal CH_3 units of propane using TraPPE-UA and HH-Alkane models, respectively. The dash blue line and blue circles indicate results for the middle CH_2 unit of propane using the TraPPE-UA and HH-Alkane models, respectively. (b) The distribution functions for isobutane. The solid red line and red triangles indicate results for the pendant CH_3 unit of isobutane using TraPPE-UA and HH-Alkane models, respectively. The dash blue line and blue circles indicate results for

the central CH unit of isobutane using the TraPPE-UA and HH-Alkane models, respectively.

Kirkwood-Buff theory ascribes the partial molar volume of solutes at infinite dilution to an integral over the radial distribution function measure relative to any alkane site⁹¹,

$$v_s = kTk_w + \int_0^\infty [1 - g_{sw}(r)]4\pi r^2 dr \quad (1.12)$$

Where k_w is the isothermal compressibility of water. Given the agreement between the radial distribution functions obtained using the TraPPE-UA and HH-Alkane potentials, the partial molar volumes are expected to agree with one another. In general, the alkane partial molar volumes obtained using the HH-Alkane model are approximately $1 \text{ cm}^3 \text{ mol}^{-1}$ less than those obtained using the TraPPE-UA model (Table 1.2)

	Experiment	TraPPE-UA	HH-Alkane
Solute partial molar volume: v_s (cm^3/mol)			
Methane	37.14 (0.66) [*]	37.4(1.1)	37.1(1.0)
Ethane	52.24(1.11) [*]	51.2(1.0)	50.3(1.4)
Propane	69.31(2.4) [*]	66.4(0.6)	65.9(0.8)
Butane	75.55(8.00) [*]	81.6(0.8)	80.2(0.8)

Isobutane	82.78(2.00) [*]	83.0(1.0)	81.7(1.1)
Neopentane	100.50(3.00) [*]	99.4(1.0)	97.7(0.8)

Table 1.2 Solute partial molar volume of various linear and branched alkanes obtained through experiment, TraPPE-UA and HH-Alkane.

This results from the increased attractions for the HH-Alkane model pulling approximately $1 \text{ cm}^3 \text{ mol}^{-1} / 18 \text{ cm}^3 \text{ mol}^{-1}$ (the ratio of the decrease in the alkane partial molar volume to the partial molar volume of water) ≈ 0.06 water molecules closer into its sphere of influence than the TraPPE-UA model. More importantly, both simulation models provide excellent quantitative descriptions of the experimental volumes, and it is difficult to discriminate between either models' agreement with the experiment based on the reported errors. We note that in a previous simulation study of the partial molar volumes of methane, ethane, propane, and butane in TIP3P water, the simulations systematically overpredict the experimental results by $4 \text{ cm}^3 \text{ mol}^{-1}$ for methane to $22 \text{ cm}^3 \text{ mol}^{-1}$ for butane⁴². Such overprediction was ascribed, in part, to the poor description of water's equation-of-state by the TIP3P model. We believe that the significantly improved description of the partial molar volume found here results from the comparatively superior description of liquid water by the TIP4P/2005 model.

1.4 Concluding Remarks

Beginning with the TraPPE-UA model for linear and branched alkanes as a foundation, we developed the HH-Alkane model by optimizing solute site/water oxygen cross interactions to reproduce the hydration free energies of methane, ethane, propane, butane, and neopentane over a range of temperatures. Optimizing LJ interactions leads a lowering of the LJ well depth by $\Delta\epsilon_{iw}/k \approx 3$ to 6 K. Concurring with previous studies of noble gases and methane in water, we ascribe the increase in the cross interaction well depth to polarization of the alkane by water. This effective polarization is largely absent in the TraPPE-UA model since it was originally developed to reproduce the phase behavior of the non-polar alkanes. We have optimized HH-Alkane interactions for all the CH_n sites ($n = 0$ to 4) permitting extension of the model to any linear or branched alkane in water.

Fixing the alkane site thermal radii during optimization of the HH-Alkane interactions resulted in an overemphasis of the enthalpy and entropy of hydrophobic hydration for propane, butane, and isobutane. This discrepancy could potentially be alleviated by simultaneously optimizing the site radii as well, which can affect the hydration entropy through perturbations in the site-water pair correlations⁴³. In addition to expanding the parameter space over which interactions must be optimized, changing the site radii could prove detrimental to the excellent description of the alkane partial molar volumes

provided by the HH-Alkane model. We thereby assert that the HH-Alkane model provides a balanced description of the aqueous solubility of alkanes in response to perturbations in both the temperature and pressure.

Since the TraPPE-UA model is largely used for modeling alkane phase equilibria, we expect our modifications to this model to be most accurate for modeling alkane partitioning between aqueous and organic phases. Ongoing efforts in our group are extending the present study to validate the ability of the HH-Alkane model to quantitatively predict the thermodynamic signatures of hydrophobic hydration for a broader range of alkanes and hydrocarbons. In the field of protein folding where all-atom force fields are the standard, concurrent efforts in other research groups are aimed at re-parameterizing polypeptide interactions to model helix formation in the highly optimized TIP4P/2005 water model to more closely match the experiment⁴³. We believe the conclusions drawn here regarding the necessity of accounting for polarization interactions between hydrocarbons and water, either through re-parameterization of LJ interaction or potentially an explicit polarizability, are applicable to the development of all-atom protein force fields as well.

Chapter 2

Probe the Thermo-responsive Behavior of Polymer N-isopropylacrylamide (NIPAM)

2.1 Introduction

During the last decades, there have been significant interests of scientists and engineers in investigating the next-generation high performance polymeric materials. The development of smart polymer, or called stimuli responsive polymers had exhibited tremendous promising potential and made soaring progress. Specifically the developmental focus of smart polymers mainly relied on achieving the polymer controllable response to external stimuli such as PH, temperature, irradiation⁴⁴. In addition, the polymeric system can be constructed rationally with a wide range of architectures covering single chain polymer, 2 dimensional films, 3-dimensional particulates and assemblies, etc⁴⁵.

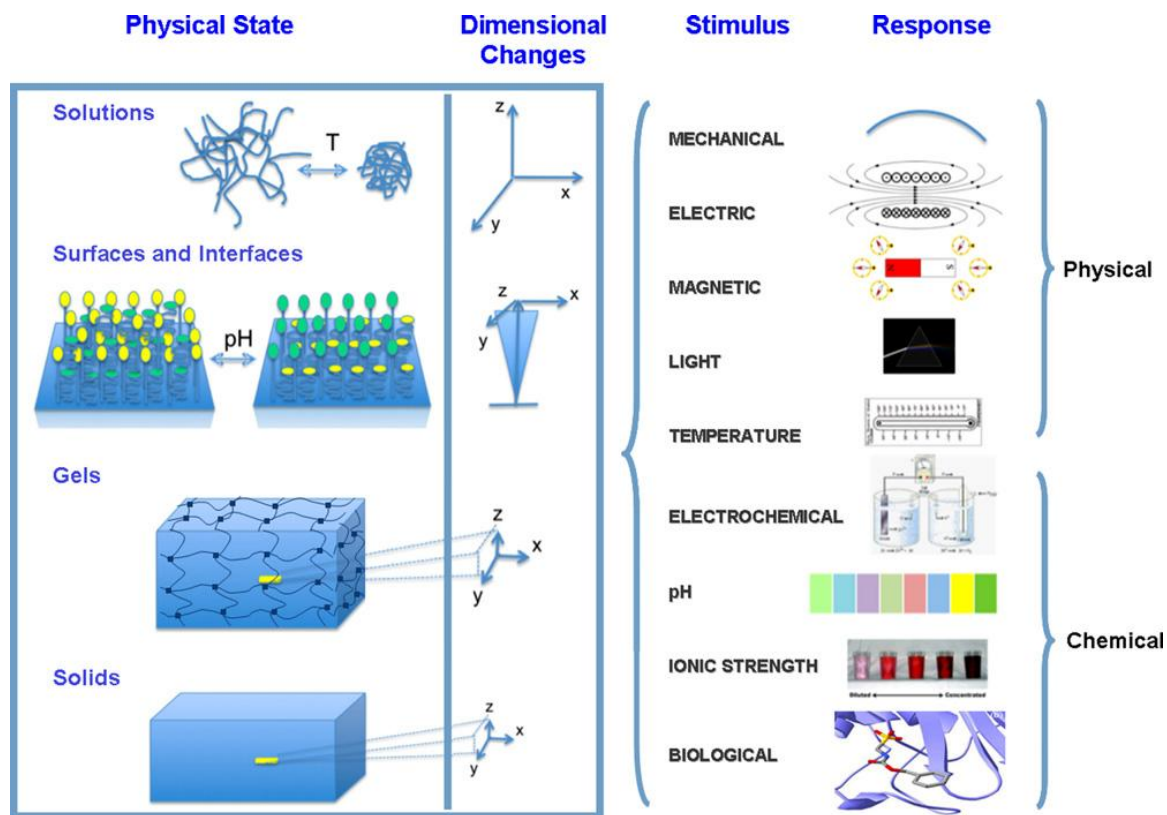


Figure 2.1 Schematic representation of dimensional changes in polymeric solutions at surfaces and interfaces, in polymeric gels and polymer solid resulting from physical or chemical stimuli by Liu et.al⁴⁵

Because of on-going effort in developing specialty materials as well as their pertaining architecture reconstruction, these materials are playing significant parts of wide and diverse application like drug-delivery system⁴⁶, tissue engineering, epicardial restraint therapies and smart biosensor⁴⁷ as well as micro-electromechanical system⁴⁸, coating and textiles⁴⁹.

Lower Critical Solution Temperature (LCST) polymer is typical one of the thermal responsive polymer which achieves functionalities' switch via undergoing structure change controlled by temperature⁵⁰. Polymer phase transition occurs counter-intuitively in LCST system, which as temperature increase above critical temperature turned solution from miscible mixing state into immiscible state⁵¹. The unfavorable entropy of mixing is generally considered as the driving force leading such phase segregation. But the origin of such incompatibility is still under-debated. One physical explanation is due to the stronger polar interactions or increasing hydrogen bonding number which prevents random mixing; Another explanation is due to the solvent's favorable structure being disrupted resulting loss of entropy. For the aqueous solution, prior consideration is usually taken from the first perspective. Specifically speaking, hydrogen bond forming between solute and water lead large negative entropy compensated with relative moderate gain orientational entropy at low temperature. However, as temperature increasing, hydrogen bonds are destabilized due to dramatic gaining of unfavorable entropy during the phase transition. Interestingly, even though the heating of system breaks up hydrogen bonding the only presence of hydrophilic group doesn't lead the occurrences of spinodal LCST phase behavior. Most views attributed the electrolyte or hydrophobic groups to the immiscible mixing within temperature increasing.

Among various polymers exhibiting LCST behavior, N-isopropylacrylamide (NIPAM) is the most extensively studied polymeric materials either in form of homo-polymer, block-copolymer or more complex topologies. In an aqueous environment, NIPAM exists as coil structure at low temperature, but undergoes a discontinuous, dramatic phase transition to a collapsed state above LCST ($\sim 305\text{K}$). LCST close to human body temperature and bio-compatible nature earn high credibility for it to be applied as drug delivery materials. Not only how to design and engineering the phase transition temperature to achieve effective control became the main concern of researchers, but also understanding the chemical nature which is generally considered as determining factor of NIPAM temperature sensitive dramatic change has been raised great attention. Otake et.al performed a thermal analysis of volume phase transition of PNIPAM hydrogel and attributed main effect of high temperature collapse to hydrophobic interaction⁵². Sun et al. Utilized FT-IR spectroscopy to study the intensity of characterizing PNIPAM group's vibration frequency treating with heating and cooling. They concluded that observation of a hysteresis curves represented thermal-shrinking and swelling of hydrogel, which further led the discussion that conversion of hydrogen bond between intra and inter type may determine the linking network formation of PNIPAM⁵³. Wu et.al had successfully observed conformation change of single homopolymer PNIPAM chain from coil to a fully collapsed stable globule state via laser light scattering measurement⁵⁴. Giuseppe

examined PNIPAM's experimental data and took advantage of analogy between coil to globule collapse of PNIPAM and cold renaturation of globular proteins to propose theoretical prediction of free energy change⁵⁵. Thermodynamically speaking, NIPAM's thermal collapse is an entropy-driven endothermic process. Experimental results indicated the relationship between specific state or structure at different temperature and potential theoretical model's prediction. However, observing scope along with uncertainty limited experimental investigation, which inspired various theoretical and modeling works delving into the mechanisms based on detailed molecular features. Okada et.al applied statistical mechanics based approach to derive a phase diagram of NIPAM LCST behavior which is compatible with experimental spinodal diagram. Cooperative hydration parameter determining shape of LCST phase diagram⁵⁶ is extracted out. Such hydration parameter consisted temperature factor and nearest neighbor bound water sites' interacting parameter which are both originated from isopropyl group's steric hindrance. Besides statistical mechanics modeling, the earliest Molecular Dynamics simulation work can be traced to the research conducted by Yoshinori et.al. They investigated water structure around PNIPAM's hydrophilic and hydrophobic parts⁵⁷. Comparing with the counterpart's behavior of UCST polymer PVA, severe polar and water interaction is attributed to be constraints of water stabilization around LCST polymer. Walter et.al performed large-scale MD simulation to study the

conformation change of single chain NIPAM in water⁵⁸. They tested several combinations of force fields and suggested OPLS+SPC/E water model was the optimal choice to reproduce LCST behavior of NIPAM. Tucker conducted molecular simulation to study the length dependence of single chain NIPAM oligomer's LCST⁵⁹. In addition, Deshmukh et al. performed atomistic simulation of PNIPAM, PAA and PEG at low and high temperature respectively and analysis of hydrogen-bond auto-correlation function. Results from their work indicated disruption of water ordering structure around hydrophobic group of LCST polymers determined coil-to-globule transition⁶⁰.

Substantial experimental and theoretical work both manifested a temperature induce the coil-to-globule transition of PNIPAM. The transition is generally considered to be the competitive results of hydrophobic interactions of pendent isopropyl group as well as hydrogen bonding association between amide group and water. Therefore probing into the origin of thermodynamic driving force would shed a light on speeding up further material screening of series of thermal-responsive polymer containing NIPAM monomer. In this work, we performed an atomistic molecular dynamic simulation associated with replica exchange techniques to determine the global polymer conformation and implemented multiple approaches to evaluate hydrophilic/hydrophobic groups' contribution to the overall thermal responsive ability of PNIPAM.

2.2 Simulation Methods

2.2.1 Basic Simulations Technique

A series of replica exchange molecular dynamic simulation of PNIPAM homopolymer were conducted under isothermal-isobaric ensemble using GROMACS 4.0.7⁶¹. Various solutes were solvated in different size water box (table 2.1). SPC/E water model⁶² and OPLS-AA force field⁶³ were adopted to describe solvent and solute respectively. OPLS partial charges were distributed on each atom of NIPAM, Polyacrylamide as well as Propane indicated in table 2.2. Parrinello-Raham barostat³² was used to maintain pressure at 1 bar and Nose-hoover thermostat⁶⁴ was used to maintain temperature for each replicas. A 1fs time step was used to integrate equation of motion and the neighbor list was updated every 5fs. For the intramolecular interactions, Particle Mesh Ewald method³³ was used to calculate long-range electrostatic interactions and L-J interactions were evaluated out of 1.4 nm. LINCS algorithm was used to constrain the geometry of water and fix carbon bond length. Temperatures of 15 replicas were assigned using an exponential distribution over a range from 280K to 357K: 280, 285, 290, 295, 300, 306, 311, 317, 322, 328, 334, 339, 345, 351, 357 to ensure the efficient exchange of each individual replica. The internal time spanning replica exchange attempts were tuned accordingly to ensure average periodic time of one attempt can last about 10ps. Before Replica exchange

simulation, each replica's simulation started with a stretched conformation was performed without exchange until they were equilibrated. An implemented REMD program in GROMACS packages was used to perform 50ns REMD simulation for various systems. Atomic trajectories were stored every 2ps and were obtained for analysis for various structural and dynamical properties of molecules.

Solute	N-isopropylacrylamide	Polyacrylamide	Propane
No. of Water molecules	4123 (80mers) 3001 (40mers)	3113 (80mers) 2528 (40mers)	1000

Table 2.1 Various system's solvent number

Atom number	1	2	3	4	5	6	7	8	9	10
Partial charge	-0.12	-0.06	0.5	-0.5	-0.5	0.3	0.14	-0.18	-0.18	0.06
OPLS-AA No.	136	137	235	236	238	241	229	135	135	140

Table 2.2 OPLS-AA partial charge distribution of monomer atoms

2.2.2 Details of Analysis

Radius of gyration was calculated to characterize the stretching degree of the chain based on the following equation,

$$R_g = \left(\frac{\sum_i \|r_i\|^2 m_i}{\sum_i m_i} \right)^{\frac{1}{2}} \quad (2.1)$$

Where m_i is the mass of atom i and r_i is the distance from atom i to the center of mass of polymer chain. Average R_g was calculated as root mean square value of 50000 conformations. To analyze the interactions between solute and solvents, hydrogen bond number was evaluated by the GROMACS implemented analysis program `g_hbond`. Nitrogen of amide group is defined as donor and oxygen of carbonyl group was defined as acceptors. Geometric criteria for hydrogen bonds were set based on the distance between acceptor and donor (below 0.3 nm) and the angle acceptor-donor-hydrogen (smaller than 30°). Radius distribution functions (RDFs) were also calculated between center carbon atoms of isopropyl groups (C2-C2) via FORTRAN based code.

2.3 Results and Discussion

2.3.1 Radius of Gyration

To intuitively describe the temperature responsive structural change, the average radius of gyrations of 80mers and 40mers homopolymers at various temperatures were extracted

out based on 50ns simulation trajectories, adapting the formula mentioned in the previous chapter. As Figure 2.2 shows, both 80mers and 40mers NIPAM polymers underwent a thermal-collapse within heating up the simulated system associated with water-intermediated interaction. Noticeable cooperative transition of 80mers, which had been affirmed in static light scattering experiment by Wu's group⁵⁴, was displayed in the studied temperature range from 280~360K. Instead of first-order transition frequently observed in NIPAM's Hydrogel/ Co-polymer solution⁶⁵, polymer gradually transformed from stretched coil form to tangled globule form and basically reached a stable state at 320K. Tough 40mers polymer's cooperativity was not as obvious as longer polymer chain, temperature induced collapse was manifested either from the radius of gyration trend or from snap shots observations. The predicted curves were obtained from reverse derivation discussed by following sections, which depicted coil-to-globule transition more clearly and accurately.

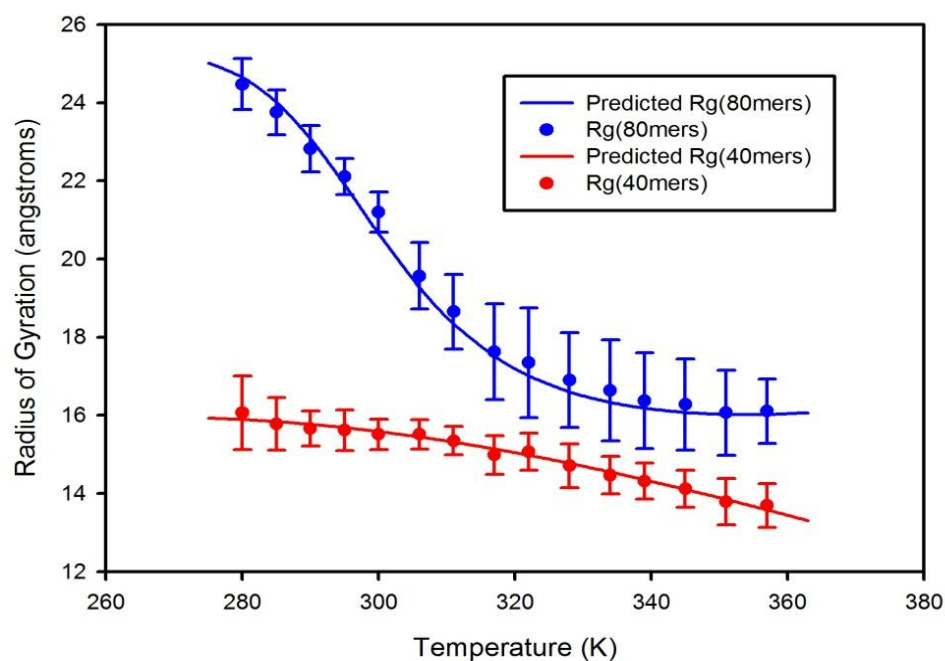


Figure 2.2 Average radius of gyration of NIPAM homopolymer in different length. Blue curve and dots represent 80mers' data; Red curve and dots represents 40mers's data.

Within further analyzing radius of gyration data, both 80mers' and 40mers' probability distribution of Rg can be enlisted in terms of different temperature like Figure 2.3 shows.

In figure A, most 80mers NIPAM's conformation existed in an extended state that Rg was above 20 Å at 280K. At the mid temperature 300K, the distribution was almost balanced between collapsed forms and extended forms dividing by 20 Å plus a vacant distribution area around the dividing point. Continuing with analyzing high temperature sample 357K, the contrary result from 280K was that probability distribution centralized at low radius range about 14 Å and scarcely appeared above 20 angstroms. Three

representative temperatures indicated NIPAM favorably either existed in extended state or collapsed state but were not fond of intermediate state, which was a typical two-state transition behavior.

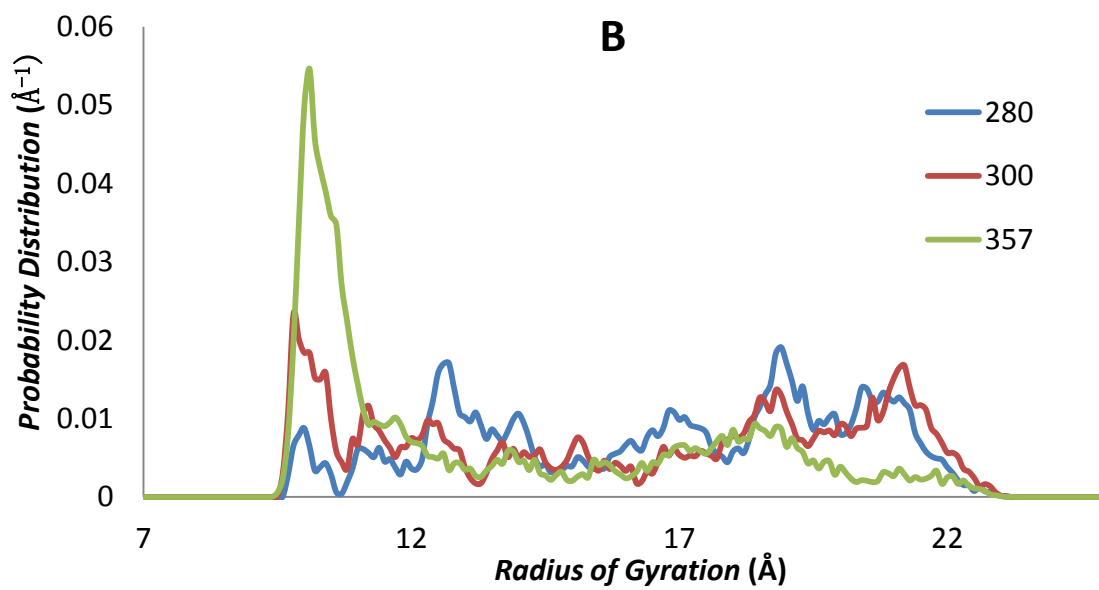
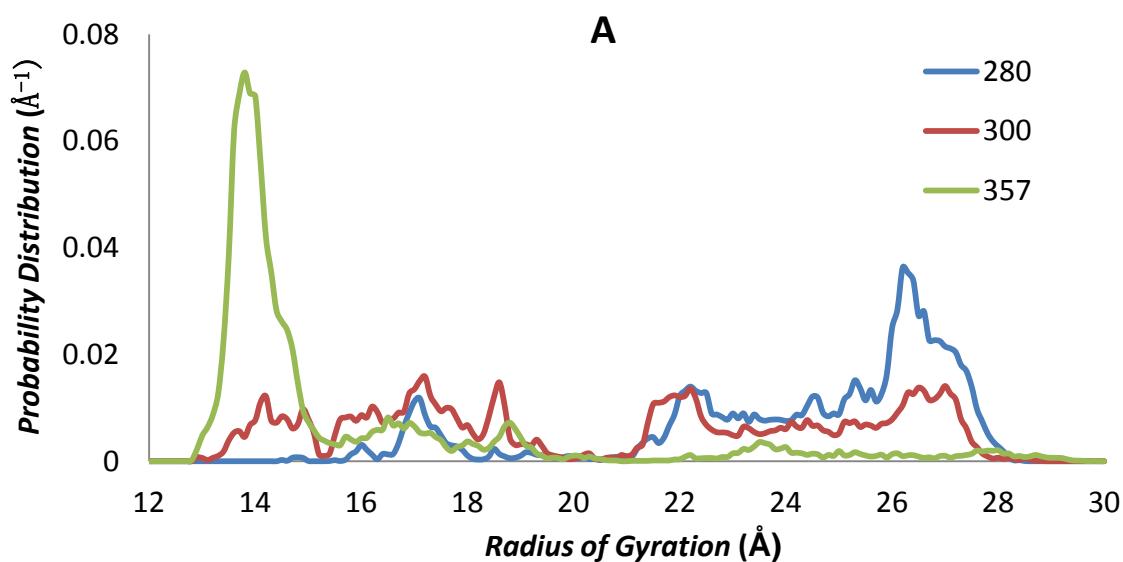


Figure 2.3 Probability distribution of R_g at selected temperature (280K, 300K, 357K) for (A) 80mers and (B) 40mers

As Figure B indicated, a similar scenario of probability distribution as 80mers was observed for 40mers NIPAM. At R_g around 10 Å, a series of gradual increasing peaks represented the globular structures are growing from 280K to 357K. Correspondingly, at R_g around 19 Å, a series of gradual decreasing peaks indicated coil conformations were reduced from 280K to 357K. However, the intermediate distribution was not as vacuumed as 80mers' distribution. In other words, cooperativity of two-state phenomenon for 40mers was not as intensive as 80mers polymers.

2.3.2 Coil-to-Globule Two-State Transition

By nature, protein folding is all-or-none transition process. Heating or cold denaturation of globular protein can be described as two-state equilibrating process, which means proteins either exist in unfolded state or native state⁶⁶. Such underlying folding equilibrium also can be significantly determining free energy change spanning between two states and approved to be an efficient approach to quantitatively characterize the interactions of biomolecules. Based on another perspective, protein can be defined as a heteropolymer consisting both hydrophobic and hydrophilic constitutes. Similarly, NIPAM's thermal responsive behavior is generally considered to be originated from leading role switching between hydrophobic groups and hydrophilic groups as

temperature increases. The analogy between protein folding and polymer thermal's collapse delivered an original pathway to discover what leads the cooperative phase transition of NIPAM. To apply two-state model, we generally divided a probability distribution into two parts at R_g 20.5 Å for 80mers and 15.5 for 40mers. The probability summation above dividing point belonged to the probability of coil (P_C) as well as the one below dividing point belonged to the probability of globule (P_G). Therefore, we are able to summarize the coil and globule distribution probability change as a function of temperature like Figure 2.4 shows. For 80mers, temperature located at the meeting spot, which ratio of P_C and P_G was unity, was approximately Lower critical solution temperature (LCST~305K) observed in experiment. Until 340K, P_G and P_C reached minimized value representing invariance of their ratio's temperature dependence. Some other interesting observation from simulation is LCST of 40mers NIPAM is about 317K, which is higher than 80mers polymer. Molar effect to NIPAM brushes' LCST actually had been validated in previous DSC measurement⁶⁷. In addition, Chapman group also implemented DFT-iSAFT approach to investigate LCST behavior of polymer brushes and concluded that LCST behavior was dependent of molecular weight of polymer and the critical temperature was decreased within prolonging polymer units⁶⁸. Thus that, lower LCST for longer chain polymer can be expected.

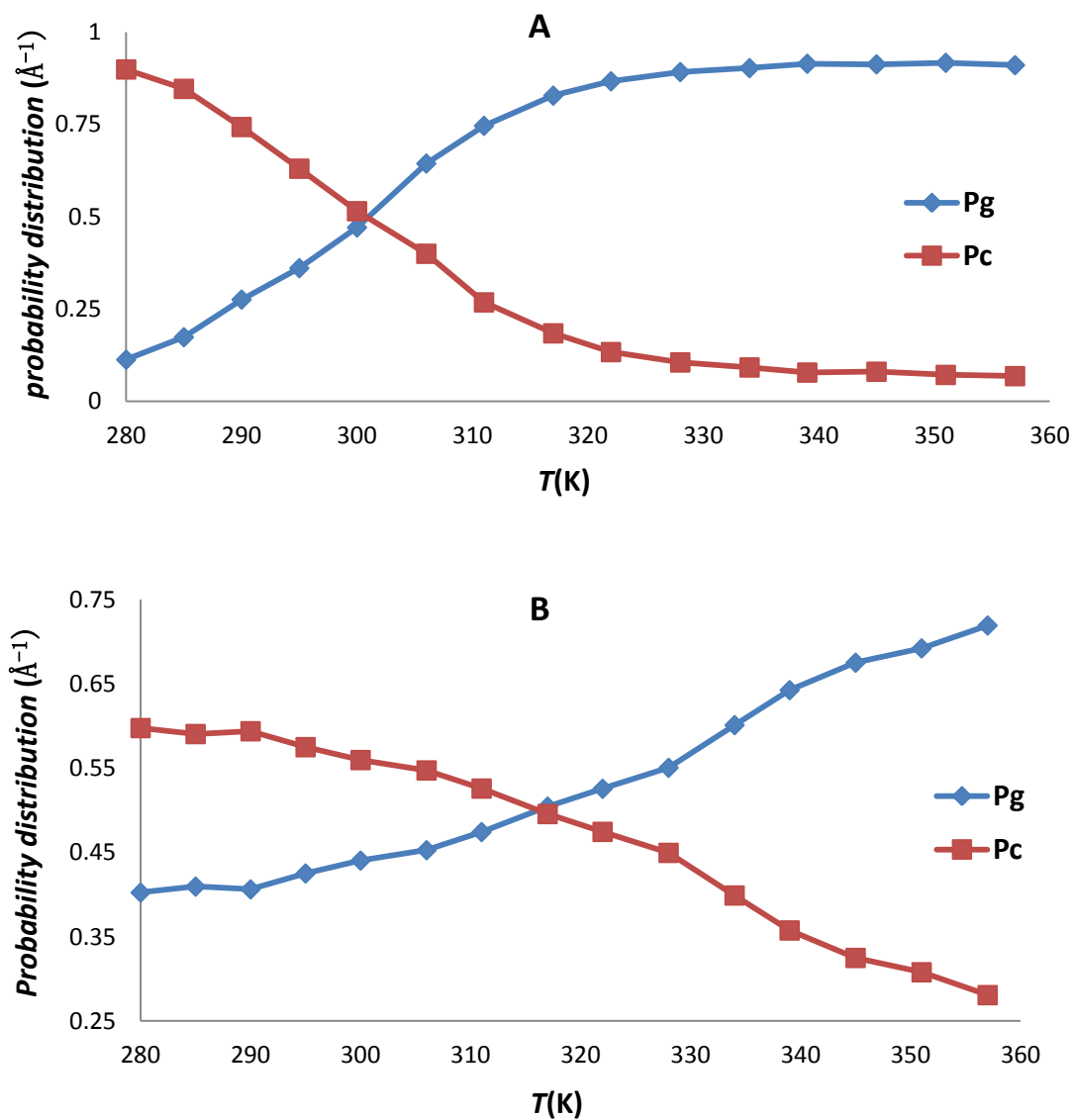


Figure 2.4 Probability distribution of various length NIPAM homopolymers as function of temperature: (A) 80mers, (B) 40mers.

2.3.3 Free energy of Coil-to-Globule Transition

Aiming at quantitatively analyze thermal-responsive behavior, previous two-state model was extended to free energy calculation based on the following equation, in which K_{eq} is defined as the ratio of P_C and P_G .

$$\Delta G = -RT \times \ln K_{eq} \quad (2.2)$$

Like Figure 2.5 showed, Free energy of 80mers parabolically increased from a negative value to a positive value resembling a driving force leading thermal-responsive collapse. To build a relationship between temperature and free energy, we further applied a classical thermodynamic equation describing hydrophobic interaction to fit into simulation results following Eq.2.3:

$$\Delta G^* = A + B(T - T_0) + CT \ln \frac{T}{T_0} \quad (2.3)$$

In the above equation, reference temperature T_0 was 300K. Additionally, fitted curve parameters were summarized in Table 2.3. Fitted value was closely approximated to simulation results and displayed a thermodynamically based exploration. Recalled discussion in the first chapter, thermodynamic signature of hydrophobic hydration rendered almost same trend like NIPAM's free energy temperature dependency. Such observation also inspired us to carefully examine hydrophobic effect's role in resolving the overall structure change.

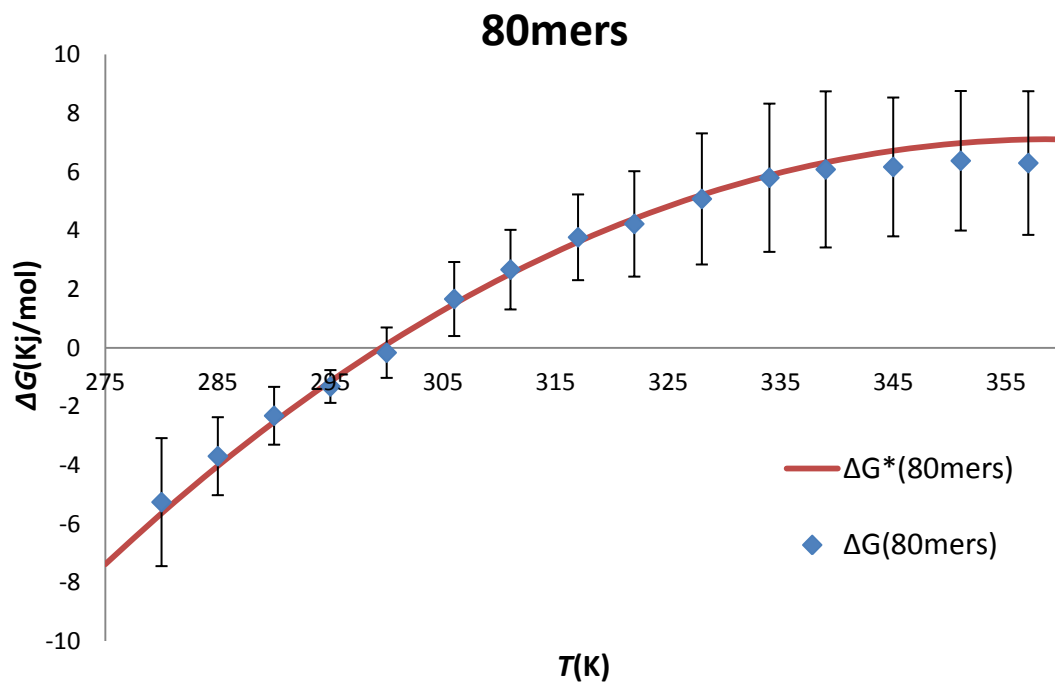


Figure 2.5 Free energy of 80mers NIPAM as function of temperature, the blue diamond represents simulation results. The red line represents predicted value obtained through Eq. 2.2 fitting.

Parameters Length	A	B	C
80mers	0.124	1.584	-1.341
40mers	-0.558	-0.189	0.209

Table 2.3 Least square fitting parameters of equation 2.2 used to describe free energy

Compared with 80mers results, free energy of 40mers was under severe fluctuation according equation 2.1. To some extent, the negative heat capacity extracted based on equation 2.1 was not convincing evidence supporting hydrophobic effect's leading role. However, larger fluctuation should also be taken into account as an important factor leading deviation from an accordable convergence of 80mers NIPAM. Mainly two reasons might be leading effects of such phenomenon. Firstly, shorter chain polymer owned shallow ensemble barrier, which made it easier to exchange information within replicas. Statistical average results were therefore widely perturbed under frequent exchange of information. Secondly, entropic contribution was significant part influencing overall thermal-responses. Less coil conformations of shorter chain polymer diminished the tendency to form a globular structure, which intuitively provided relative less entropy information

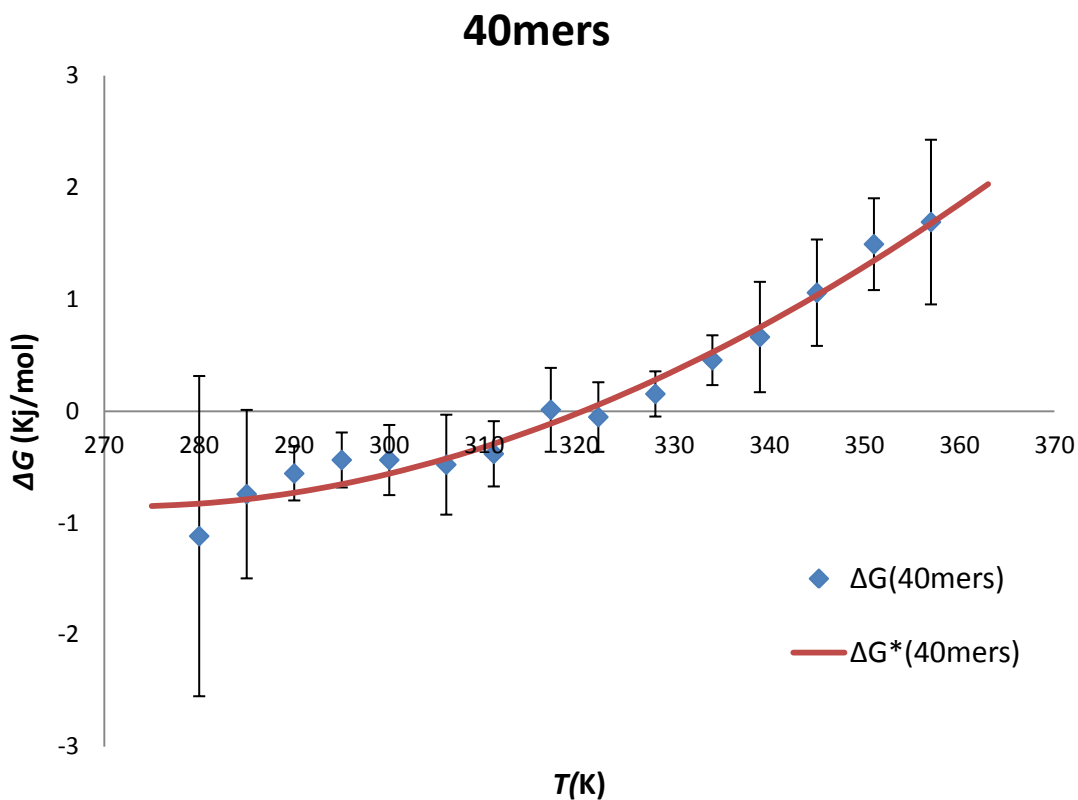


Figure 2.6 Free energies of 40mers NIPAM as function of temperature. The blue diamond represents simulation results. The red line represents predicted value obtained through equation 2.2 fitting.

2.3.4 Predicting Radius of Gyration Using Two-state Model

Another merit of applying two-state model is that we can reversely derive radius of gyration from predicted free energy. Firstly, equilibrium constant K_{eq} can be estimated from Potential of Mean Force according equation 2.4. Secondly, P_C was able to be assessed from K_{eq} according to equation 2.5. Following the relationship that R_g^2 was linearly correlated with P_C , a predicted R_g^{*2} was derived by inputting P_C^* as equation 2.6

indicated. Thus that, a predicted solid line can be extracted out from simulation results using two-state model approach shown in Figure 2.2.

$$K_{eq}^* = e^{-\frac{\Delta G^*}{RT}} \quad (2.4)$$

$$P_C^* = \frac{K_{eq}^*}{1+K_{eq}^*} \quad (2.5)$$

$$R_g^{*2} = aP_C^* + b(1 - P_C^*) \quad (2.6)$$

Parameters a, b of 80mers for above equation 2.6 are 420.20 and 221.52; Parameter a and b of 40mers for above equation 2.5 are 301.99 and 75.03.

2.3.4 Simulation of Polyacrylamide

Previous sections reviewed the thermal responsive collapse behavior of NIPAM based on the molecular analysis of radius of gyration for longer length homopolymer or shorter one in a temperature range from 280K to 357K. Analogous to two-state model, a predicted theoretical transition curve had been drawn out to present NIPAM's counterintuitive thermal responsive character. Due to all the circumstance observed, hydrophobic parts' temperature dependence should be a central value resolving the thermal responsive behavior. Following discussion, focus mainly were laid on two functional groups: amide group and isopropyl group. The previous one was in charge of building the internal and

external hydrogen bond networks of NIPAM, the following one was a sensitive group of hydrophobic hydration.

One approach to evaluate the importance of the isopropyl group in resolving the thermal collapse is to perform analogy REMD simulation of Polyacrylamide (PAM) and compares the effect with NIPAM. Basically, PAM is a similar homopolymer as NIPAM but not consisting of isopropyl groups. As NIPAM's simulation schemes, both 80mers and 40mers polymers were simulated for 50ns among 15 replicas. As Figure 2.7 indicated, radius of gyration derived from our simulated results didn't manifest any thermal responsive structure alternations among replicas either for 80mers or for 40mers PAM. As Figure 2.8 indicated, the probability distribution of R_g didn't render two-state transition trend among selected temperature as NIPAM for PAM. Rather than splitting conformations into two main distributions, the probability distribution of conformations for PAM tended to be expanded around one centralized area. Because the higher temperature ensemble embraced more conformation than lower temperature one, the distribution at lower temperature was enriched to form a peak while the one at the higher temperature was more dispersed to a broader area. Almost all the replicas arrived to a similar minimized energetic state for 80mers ($R_g \sim 18 \text{ \AA}$) and 40mers ($R_g \sim 10 \text{ \AA}$) respectively. In all, the structure of PAM was non-sensitive to thermal arose water intermediated interaction.

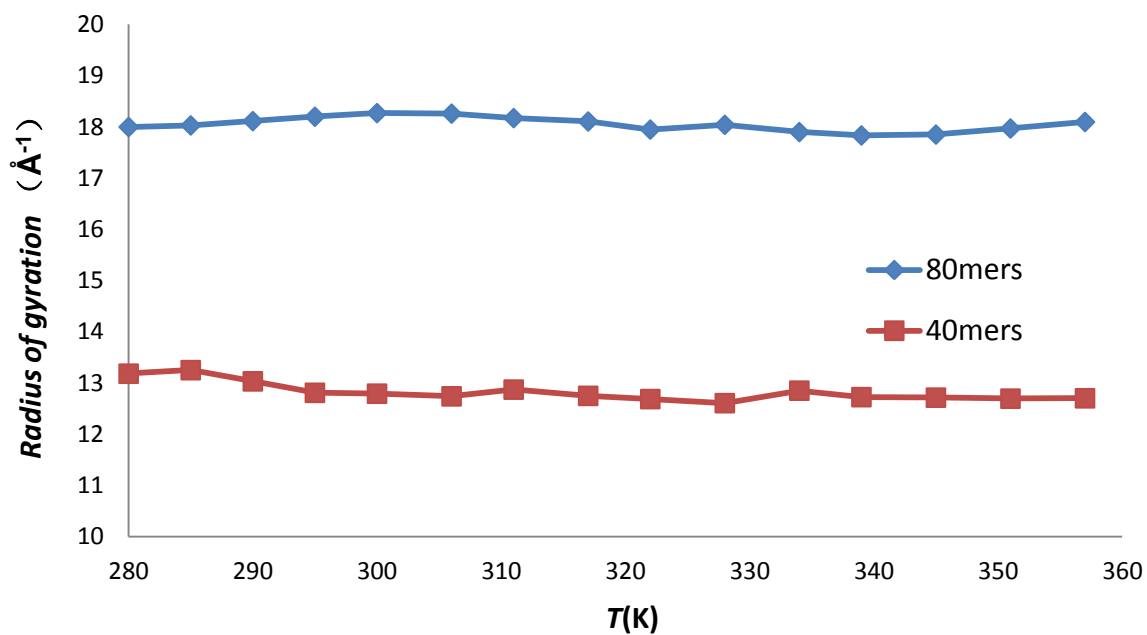
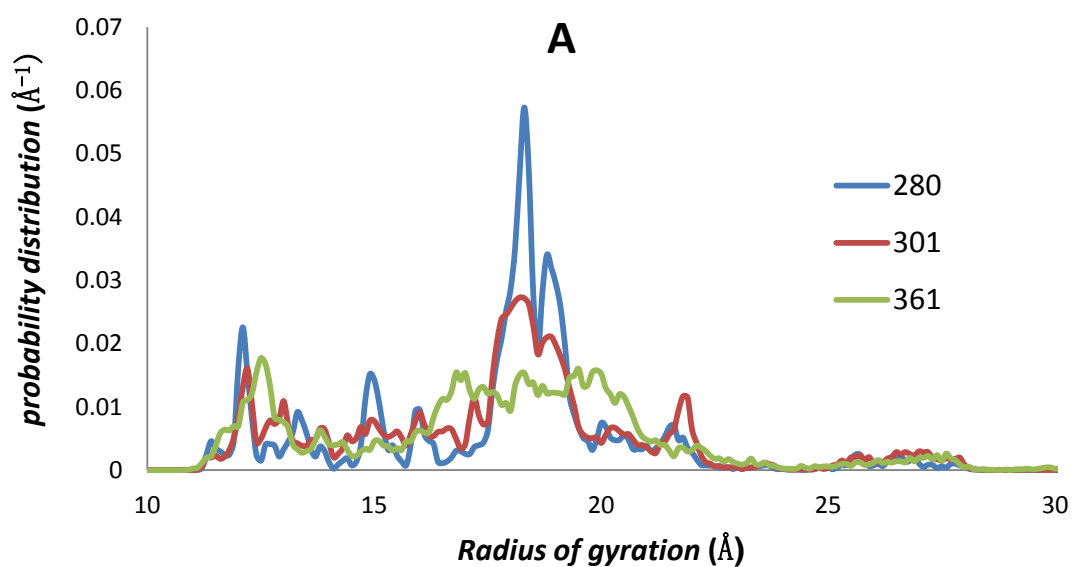


Figure 2.7 Radius of gyration as function of temperature for 80mers PAM and 40mers PAM.



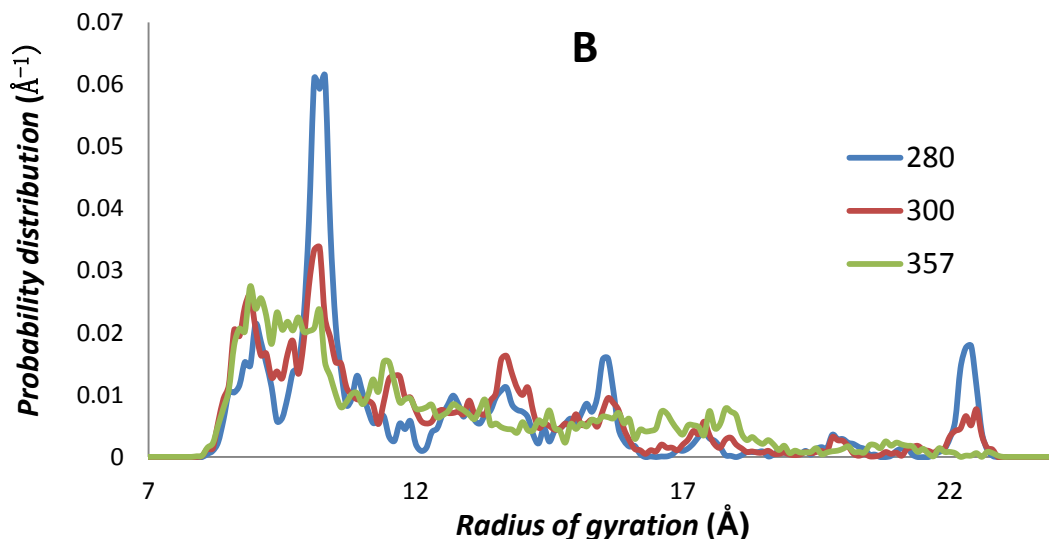


Figure 2.8 Probability distribution of R_g for 80mers PAM (A) and 40mers PAM (B).

2.3.5 Hydrogen Bond Number

Hydrogen bonds' formation and disruption are direct results of LCST phenomenon. A numerous types of hydrogen bonds co-existed in NIPAM-water system. But the main contribution comes from amide's carboxyl and amine groups. Both of these groups can interact with water to form hydrogen bonds. At the same time, they also are able to interact within own self to form an intra-hydrogen bonding networks. Therefore simulation results of PAM and of NIPAM were compared to discern hydrogen bond's temperature dependence in this section. Figure 2.9 reported analysis result of 80mers NIPAM's inter-hydrogen bond number (amide-water) and intra-hydrogen bond number (amide-amide). NIPAM's intra-molecular hydrogen bonds exhibited dramatic increase

above 300K, which was also compatible with well-known LCST of NIPAM. Correspondingly, intermolecular hydrogen bonds were declining as temperature increased. Within the phase transition temperature range (290K~317K), shielding effect of intra-molecular hydrogen bond reduced water-polymer hydrogen formation, leading the hydrogen bond number deviation from linear decreasing trend.

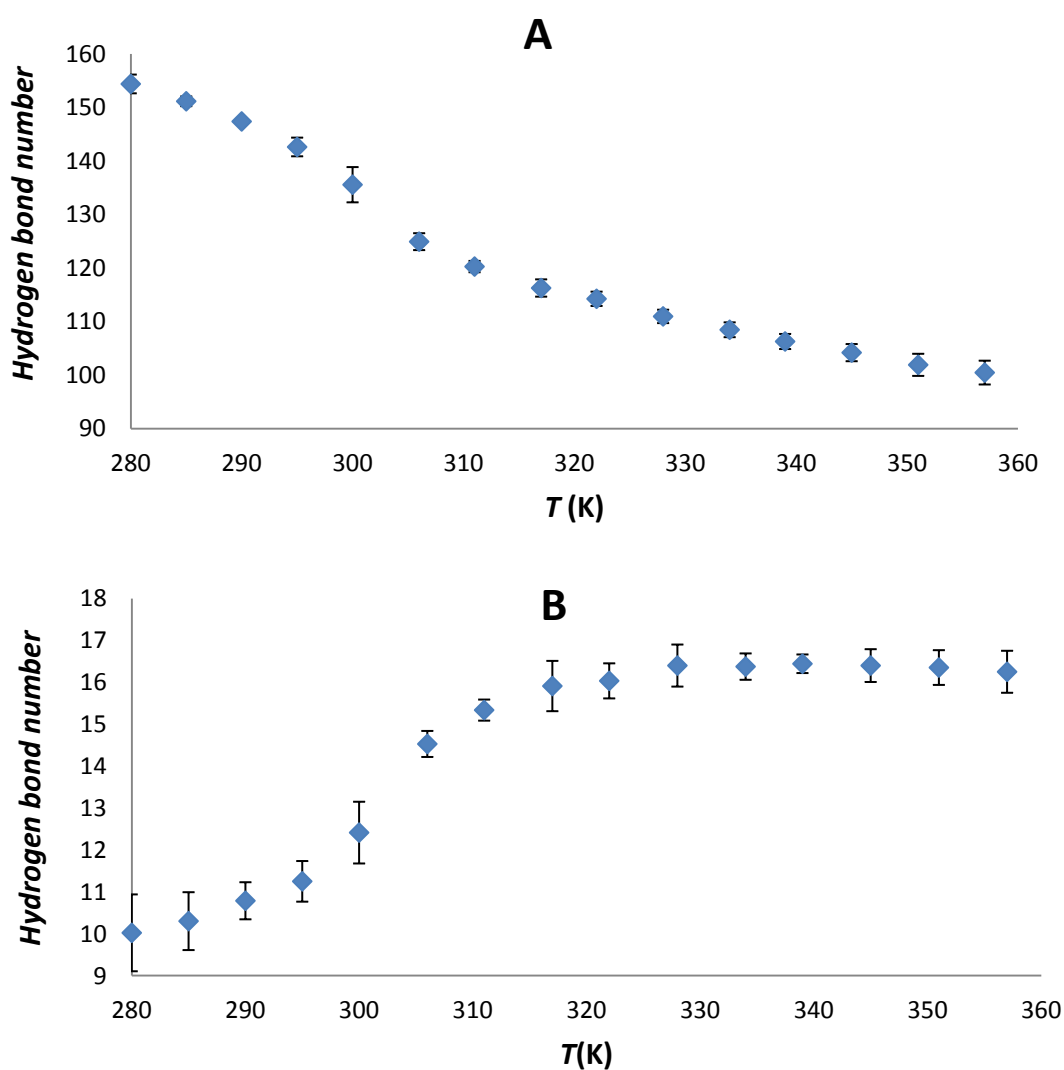
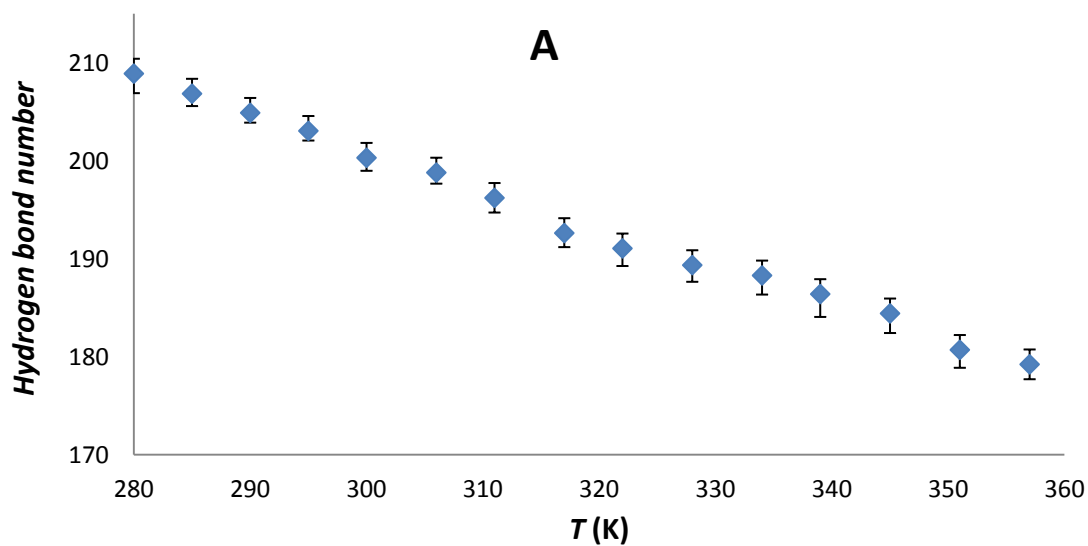


Figure 2.9 Hydrogen bond number of 80mers NIPAM: (A) Inter-molecular hydrogen

bond number; (B) Intra-molecular hydrogen bond

Figure 2.10 manifested PAM's inter and intra-molecular hydrogen bonds' temperature dependencies. Since there were two pending hydrogens at the amines' tail of PAM. The hydrogen bonding number was almost one and half times of NIPAM for Polyacrylamide. Not surprisingly, the intra-molecular hydrogen bond number was independent of temperature and inter-molecular hydrogen bond number linearly declined as temperature increases.



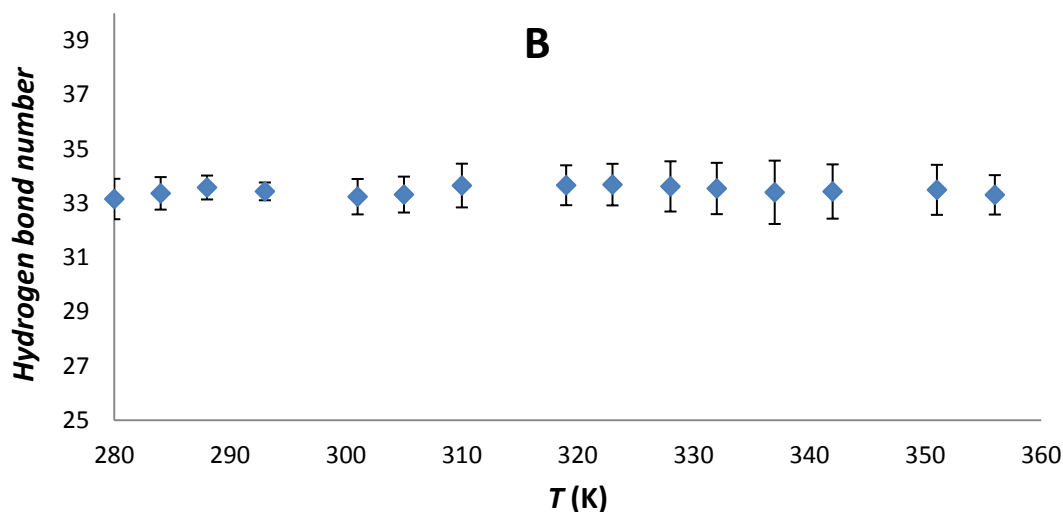


Figure 2.10 hydrogen bond number as a function of temperature for 80mers PAM: (A) inter-molecular hydrogen bonds; (B) intra-molecular hydrogen bonds.

Temperature-arose water-polymer hydrogen bonds disruption can be expected due to the entropy nature of water re-orientation. At high temperature, faster dynamics of water movement rupture stable hydrogen bonding networks. However, intra-molecular hydrogen bonds displayed obvious discrepancies between NIPAM and PAM. NIPAM's intra-hydrogen bonding status was compatible with the LCST phase transition. On the other hand, PAM's intra-hydrogen bonding was non-sensitive to temperature change. Such interesting observation made us wonder whether there were some unique properties of NIPAM apart from PAM resulting discrepancies. Apparently NIPAM's isopropyl group should be taken prior consideration. But in advancing of stepping to investigate isopropyl group, we further analyzed total fraction of hydrogen bonding which is derived

by taking account of ratio of inter and intra-hydrogen bond numbers' sum the total available hydrogen bonding sites. As Figure 2.11 indicates, two parallel linearly decreasing trends were observed, which means hydrogen bonding is consistent naturally between NIPAM and PAM. What led the dramatic difference should be relied on the extra pending isopropyl groups.

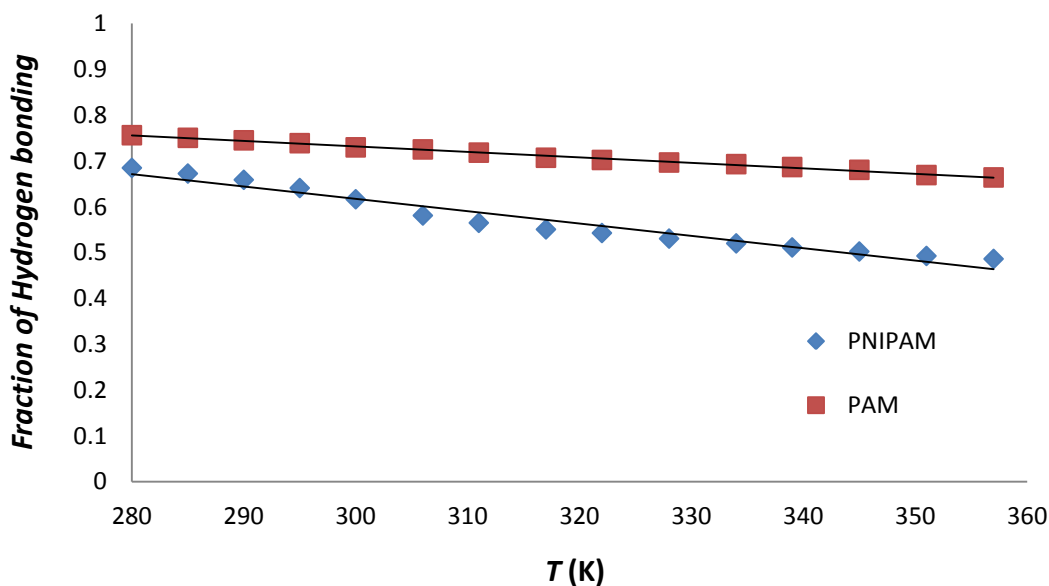


Figure 2.11 Fraction of hydrogen bonding as a function of temperature, blue diamond is data from PNIPAM. Red square is data from PAM.

2.3.6 Isopropyl Group of NIPAM

As mentioned in the previous chapter, the nature of hydrogen bonding reveals no difference in responding to heat treatment between NIPAM and PAM, which led us to switch the highlight to isopropyl groups. Driven by hydrophobic effect, apolar chemicals

in a polar environment tend to aggregate to form an oily droplet spontaneously. To explore the effect of NIPAM isopropyl groups' interaction, the analogous propane solution was simulated to investigate the common interesting features of those structural similar apolar groups. Figure 2.11 listed the results of the radial distribution function analysis of central carbon atoms' for propane as well as for NIPAM's isopropyl groups. Compared with two diagrams, the basic hydrophobic solute's orientations were similar either in terms of the first carbon shell peaking sites ($\sim 0.5\text{NM}$) or the first shell emerging sites ($\sim 0.35\text{nm}$). Though the heights of characteristic peaks were different due to the solute's various chemistries and bonding constraints, the ratios of peaking height between selected temperature (280, 300, 357) were in a consistent value between NIPAM and propane solution, which were about 1:1.2:1.5. For simple hydrocarbon, radial distribution function can be incorporated into equation 2.6 to calculate Potential of Mean Force:

$$W(r) = -RT \ln g(r) + \text{constant} \quad (2.7)$$

The free energy difference between temperature ensembles therefore can be approximately evaluated via the ratio of $g(r)$. Hydrophobic groups' interactions were under similar thermal influence no matter they were isopropyl groups pending on polymer or propane molecules solvating in water. Microscopically speaking, hydrophobic hydration induced either from isopropyl group's interaction or propane molecule likewise

hydrophobic interaction all tended to strengthen the hydrophobic solutes' aggregation as well as water expelment in the vicinity of solutes. Therefore polymer was inclined to rotate its backbone in favor of hydrophobic groups' contacting. Subsequently intra-molecular hydrogen bonding consolidated the globular structure through cross-linking network (N-H-O). Generally speaking, at low temperature amide groups associate extended conformation of polymer into the fully solvated state. Even though unfavorable entropy exists due to the effect of isopropyl groups, their influence is relatively trivial comparing with hydrogen-bonding enthalpic contribution. As temperature increases, unfavorable enthalpic part gradually takes the leading role of free energy. Hydrophobic parts' aggregating along with hydrogen bond disruption assisted polymer's fully thermal collapse. Therefore hydrophobic contribution should be an impetus of such temperature-driven self assembly phenomenon.

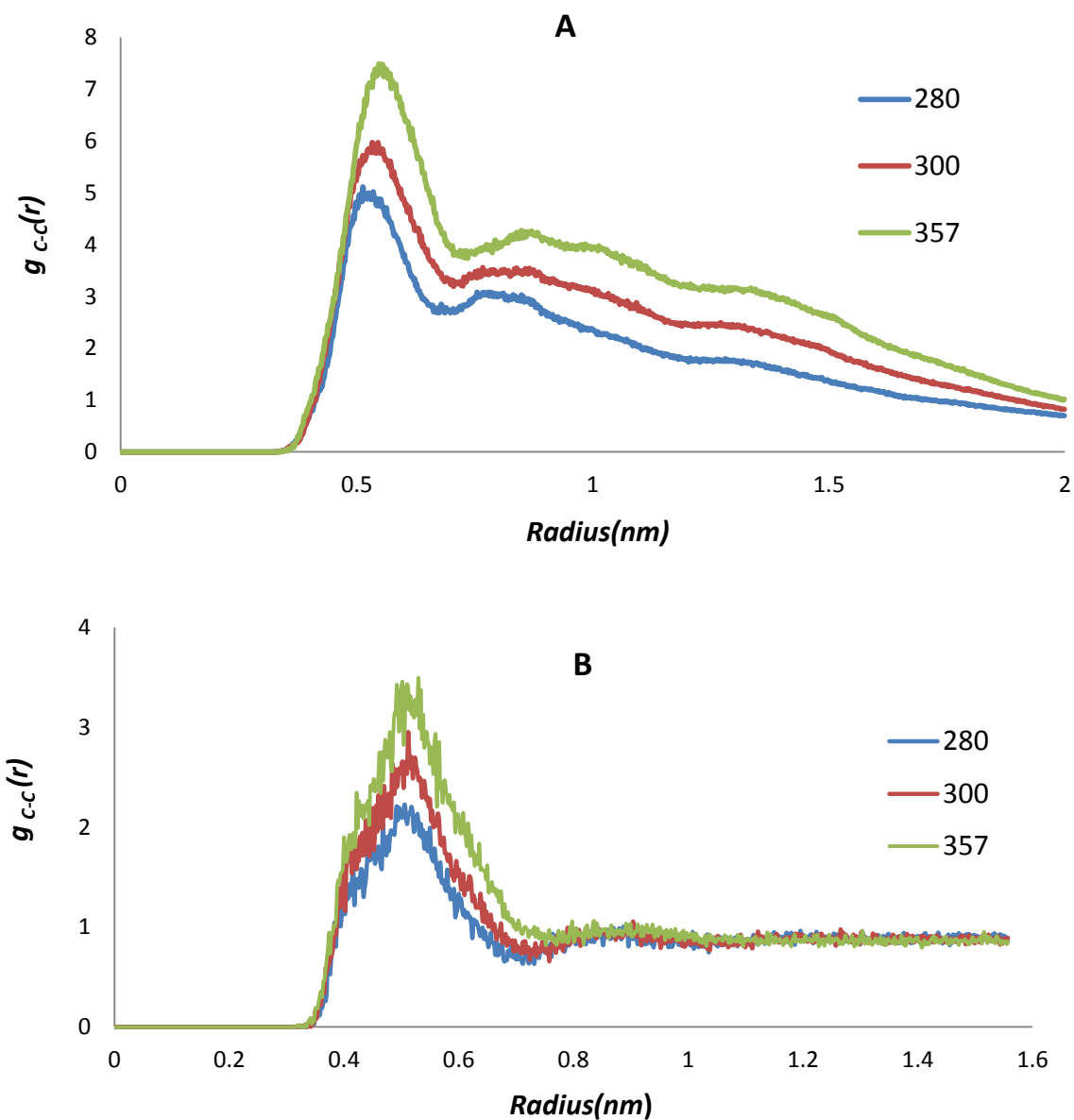


Figure 2.12 Radial distribution function of C2-C2 pair at selected temperature: (A) 80mers PNIPAM; (B) Propane solution

2.4 Conclusion

We studied of LCST behavior polymer NIPAM and discussed our simulation results as

well as theoretical approaches to explain coil-to-globule transition in a thermodynamic perspective. Firstly, radius of gyration based structural transition indicated a two-state conversion between coil and globule state undergoing as temperature increased. Through a classical two-state model fitting approach, free energy was readily extracted from structural information and was shown to be parabolic upward curve as a function of temperature. Since such thermal dependency was alike thermodynamic signatures of hydrophobic hydration, we further discussed the specific hydrophobic group's contribution versus hydrophilic group's contribution. Comparison between PNIPAM and PAM indicated that hydrogen bonding interaction didn't exhibit too much difference in terms of their total hydrogen bonding fraction. Also, both simulation results and experimental studies confirmed that PAM didn't own thermal-responsive character. What drew a dramatic variance of their thermal response should be focused on another functional group the isopropyl group. The thermodynamic signature of the hydrophobic effect for propane was considered as a good reference to determine isopropyl group's function. RDF analysis results asserted our extrapolation that the temperature induced polar solutes' affinity were almost the same degree between isopropyl groups and propane molecules. We believed our studies had achieved a remarkable progress in revealing NIPAM's self-assembly molecular details and understanding its thermodynamics impetus. What's more, the current scheme we adapted also possibly is able to be extended. To put

forth such strategies, firstly we are looking forward to exploring the temperature dependence of N-propylacrylamide, N-ethylacrylamide, and N-methylacrylamide, which will map out hydrophobicities' influence on a series of poly-acrylamide Homologs. Secondly, tune the hydrophilicity/ hydrophobicity is also a promising path to modulate LCST of smart polymer. Our simulation strategy can be taken advantage as an efficient conceptual pre-validation of co-polymer or block-polymer. Thirdly, even though OPLS + SPC/E combination is generally considered as a reliable model to perform simulation, a more accurate force field specialized to describe thermal-responsive polymer was still underdeveloped. Our two-state model fitting process can be used as one to adjust current force fields in correcting thermo-physical properties such as heat capacity or isothermal expansion coefficient. In all, our work broadened a new perspective to understand coil-to-globule transition of NIPAM based on various subjects relating with NIPAM's extraordinary LCST behavior and we believed such work should be able to shed a light on anticipated smart polymeric materials' developments.

Chapter 3

Simulations of Linear and Cyclic Amphiphilic Polymers as Potential Drug Delivery Material

3.1 Introduction

Among broad field of soft matters, Polymer-based micelles have attracted significant interests as potential drug delivery vehicles since their high affinity to various size of host molecules^{69 70}, with their excellent apt ability to assist molecule transporting through different bio-environments as well as their flexibility to tailor the properties such as internal structure and surface activity of amphiphilic polymers. Generally speaking, polymeric micelles are composed of di-block copolymer, or simplified the studied model to substance such as the surfactants. Amphiphilic structures that self-assemble to shield surfactants' hydrophobic tail groups away from water to form an oily interior microenvironment, while keeping the assembly soluble by exposing their hydrophilic group outward toward the bulk water.

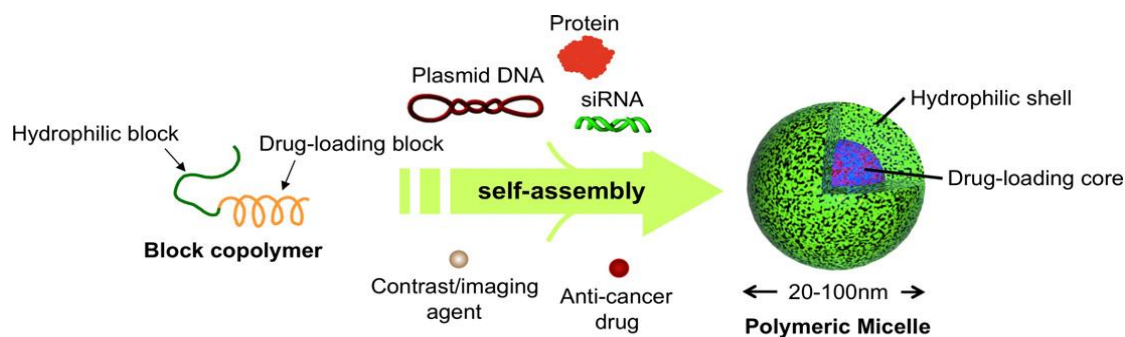


Figure 3.1 Mechanisms of polymeric micelles encapsulating drug transporting⁷¹

However, the process that individual surfactant forming microenvironment micelles is highly dependent of critical micelle concentration. At low concentration surfactants exist as monomers as a result of translational entropy of individual surfactants. Above their critical micelle concentration (CMC), however, surfactants assemble into micelles due to the hydrophobic driving force overwhelming the translational entropy.

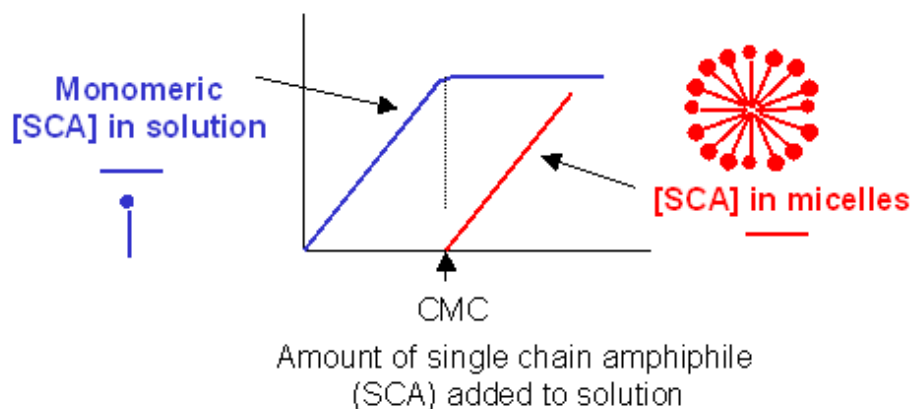


Figure 3.2 Demonstration of Critical Micelle Concentration (CMC) dependence of surfactant

Hence that instability of micellular structure indeed existed at low concentration surfactants. To overcome such unstable factor, amphiphilic dendrimer is one of the promising candidates. Dendrimer emanated from central core with exterior branching structure and terminated with periphery groups. The tree alike polymeric materials are able to be used both as drug-delivery carrier and intrinsic drug subtracts⁷². Advantage of using dendrimer is that they exhibit high competencies to deliver nano-scale bio-active molecules or nucleotides meanwhile they are built with a covalent bonding structure. However synthesis of dendrimer confronted challenges that moving from laboratory to the clinic applications. Multistep syntheses and associated higher costs of dendrimer preparation are also main obstacles blocking their commercial application⁷².

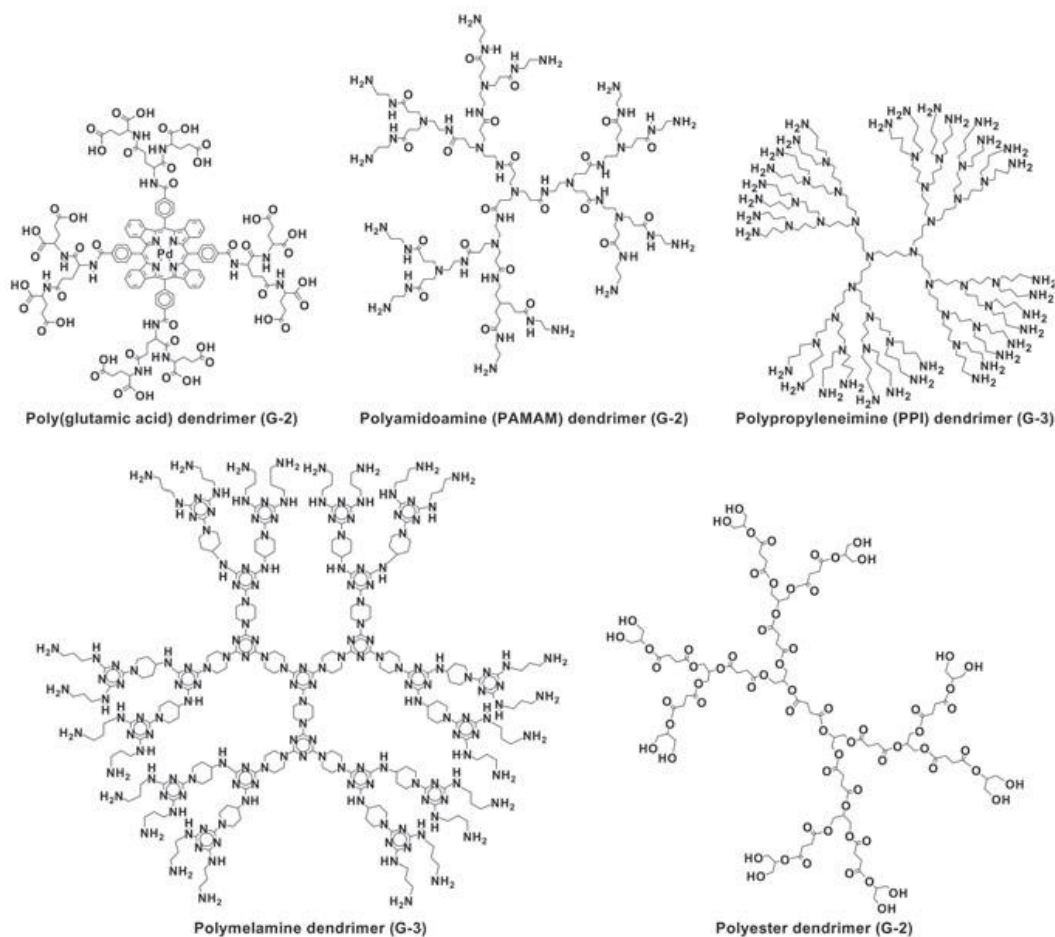


Figure 3.3 The variety of dendrimer used in biology. A few examples of the types of dendrimer chemistries used in biological applications. (a) G-2 poly (glutamic acid) dendrimer. (b) G-2 polyamidoamine (PAMAM) dendrimer (c) G-3 polypropyleneimine (PPI) dendrimer. (d) G-3 polymelamine dendrimer. (e) G-2 polyester dendrimer⁷².

Therefore to find out readily synthesis polymeric micelles is essential for developing next-stage drug delivery materials. Polymeric micelles can exhibit vastly reduced CMCs, and in the case of some branched structures, even overcome this concentration dependent assembly behavior. They can make unimolecular micelles as a result of the significant

local concentration of hydrophobic and hydrophilic groups to yield a micellar structure without aggregating with any other polymer molecules. Except drug delivery vehicles, robust nature of polymer micelles makes them attractive for a range of application as oil dispersants to nano-reactors and emulsifiers.

Laurent and Grayson recently reported synthesis of novel amphiphilic homopolymer architectures that form dynamic micelle structures that owned the capability for selective encapsulation and responsive release of guest molecules depending on the solvent polarity⁷³. These amphiphilic homopolymers were synthesized with either a linear or cyclic topology by attaching a bifurcated amphiphilic unit, consisting of a dodecyl hydrophobic side chain and a tetra (ethylene glycol) hydrophilic side chain onto performed linear and cyclic backbones using copper-catalyzed azide-alkyne cycloaddition chemistry (Figure 3.4). These polymers were shown to readily dissolve water-soluble dyes in toluene, demonstrating their potential for the encapsulation and subsequent release of water-soluble drugs when transported across non-polar barriers such as skins. Although ¹H NMR, SEC, and MALDI-TOF mass spectroscopy measurements confirm the chemical architecture of these polymers⁷³, questions remain concerning the molecular-level conformation and structure of these polymers in various solvents and their inversion upon transfer from a polar solvent to a non-polar solvent, and vice versa.

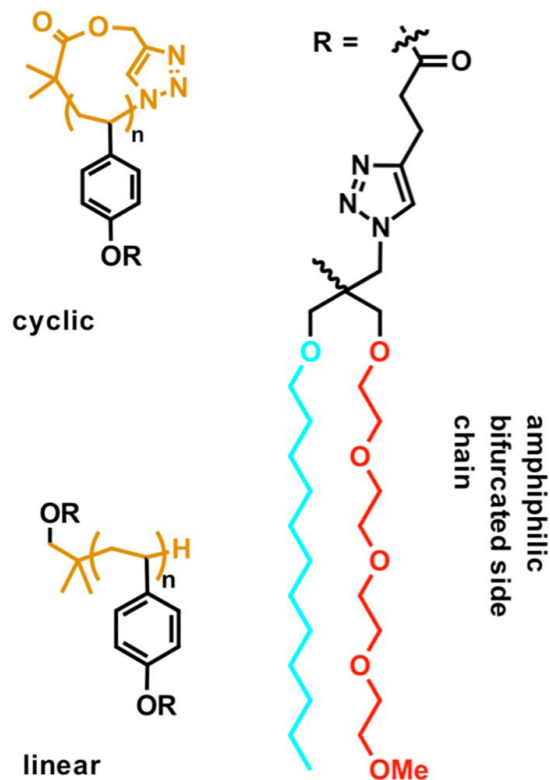


Figure 3.4 Chemical structures of the linear and cyclic homopolymer amphiphilic monomers

The vast majority of nonlinear amphiphilic polymers are structurally based toward the formation of either micelles or uni-molecular micelles. For example, amphiphilic star block copolymers are covalently attached in such a way that the core is attached to either the hydrophilic half or the hydrophobic half of the block copolymer arms⁷⁴. The micro-structural amphiphilic homopolymers first time reported recently are of particular interest because they are assembled in such a way that both the polar and non-polar side chains exhibit equal proximity to the core and to the periphery. As such, they are expected to reversibly form both micellar and reverse micellar configurations, depending

upon external stimuli. The extent to which one conformation is favored over the other is independent of the architecture, but rather dependent upon the nature of the side chains that of the external environment. For the cyclic polymers, Laurent and Grayson hypothesized that in non-polar solvents the hydrophilic ethylene glycol chains would orient themselves inward to minimize solvent interactions while the hydrophobic alkyl arms would orient outward into solvent, forming a "reverse micelle-like" configuration as depicted in Figure 3.5. Otherwise in polar solvents, the expectation of orientation is that the hydrophilic and hydrophobic arms would invert themselves and provide a "normal micelle-like" configuration (Figure 3.5). The inversion from micellar to reverse micellar configurations has been reported for linear amphiphilic homopolymers^{75, 76}. This polarity driven conformation change can potentially be exploited for selective encapsulation and stimulus-responsive release of guest molecules.

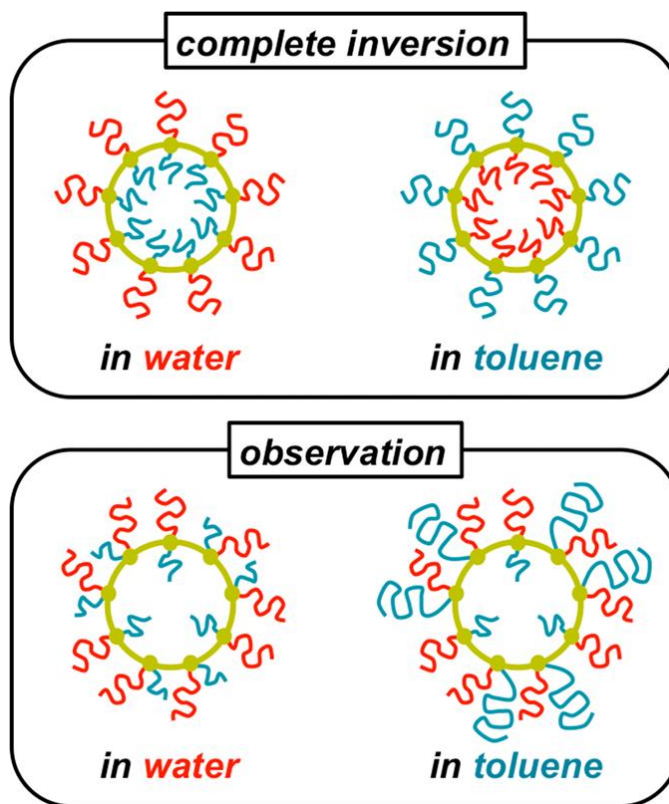


Figure 3.5 Schematic illustration of the side chain distribution about the cyclic amphiphilic polymer in water and toluene. The top figure shows the complete inversion model in which the position of the polar (red) and nonpolar (cyan) side chains completely switch their orientations relative the polymer backbone (yellow) in different solvents. The bottom figure shows the observed conformations in which the polar chains are relatively swollen in both water and toluene, while the non-polar chains retreat in water and swell in toluene. In both solvents the central ring of the cyclic polymer is observed to be filled with a pool of alkyl chains.

Herein, we seek to understand the exact placement of polar and non-polar side chains during this reversible behavior. In the simplest model for the reversibility of cyclic amphiphilic homopolymers, one could imagine the non-polar side chains being extended

outward in non-polar solutions with the polar side chains buried near the core and the polymer backbone located at the interface. In polar solvents, because of the architectural symmetry between polar and non-polar side chains, one might expect a complete inversion of the conformation, with non-polar side chains at the core, and polar ones at the periphery. Whereas the size of pool inside the cyclic backbone hasn't been confirmed using microscopy, one still may ask a question that is the central pool spacious enough or not? In Laurent's work, they already found out polymer in water is not complete soluble⁷³. How does alkyl chain affect the solubility if they bury themselves inside the core of polymer? To answer all these questions, we use all atom molecular dynamic computer simulations to study the stable conformations of Laurent and Grayson's cyclic amphiphilic homopolymers in polar and non-polar environments and use linear homopolymer analogs to help clarify the effect of the cyclic architecture on solvent-dependent conformations. Water and toluene are used as the high and low polarity solvents. This particular study focus on the conformational analysis of a singular polymer chain, and therefore it most accurately correlates with a model of amphiphilic polymers as uni-molecular micelles. Conformational changes can be challenging for simulations to explore due to the large free energy barriers between conformations, so we use replica exchange with driven scaling (REDS2)⁷⁷ method to enhance sampling of dense polymer conformations of these dense structured polymers. From knowledge of the

solvent dependence of the polymer configurations we investigate if the solvent induced conformational changes support the encapsulations and release of guest molecules⁷⁸.

3.2 Replica Exchange Simulation with Dynamical Scaling

Following with previous mentioned strategy, replica exchange simulation was implemented to explore the ultimate or at least approximate ultimate equilibrated state. However system size is always a troublesome issue impeding replica exchange simulation's application⁷⁹ with mainly two-folded technical limitations. Firstly, as Figure 3.6 indicated the thermal distributions within neighbor ensemble are scaled up with the system size number N . However the thermal fluctuations within ensembles are scaled up with the square root of N . Therefore, if system size increases four times, the overlapping energetic state actually demonstrated very scarce distribution within neighbor replicas, which hardly achieve attempts of exchanging. Secondly, the goal of replica exchange simulation is achieving swaps between lowest temperature and highest temperature. The system size dependence made it more severe by the requirement that all replicas cycle through all the temperature. More frequent swaps are in need to realize exchange within the low temperature ensemble and the high temperature ensemble. Though it is possible to achieve the widely separating replicas' swapping at the end of the day, the conformation information overflow during the communicating process. Conventional

parallel tempering turns out to be not a practical method in dealing with vast system size simulations.

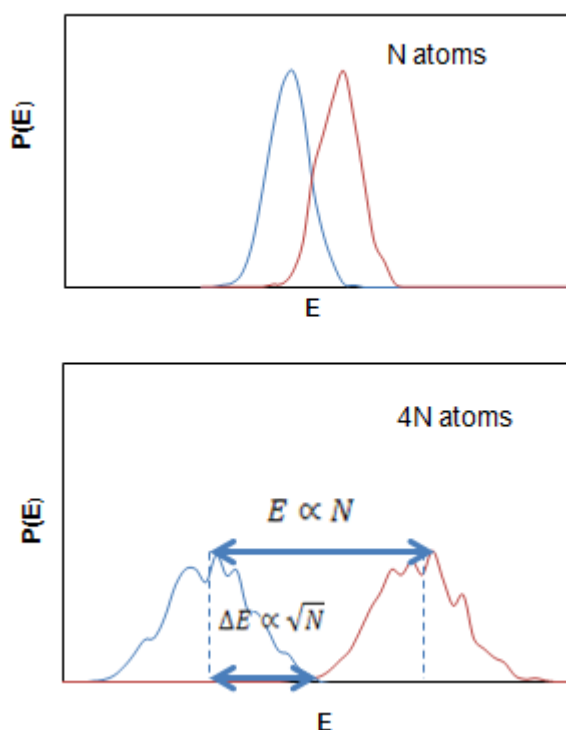


Figure 3.6 the demonstrating system size dependence of probability distribution of potential energy within neighbor thermal ensembles. The overlapping area between neighbor replicas is significantly reduced as system size increase four times.

Molecular dynamic simulation of soft matter solution system confronted such system size challenge mainly because most time a large number of solvents are required to sustain pressure balance of orthogonal box and avoid periodical overlapping of atoms especially when the solute is a macromolecule such as biopolymers, proteins and DNA. Specifically our simulated systems consist of 36713 atoms for linear amphiphilic polymers and of

35701 atoms for cyclic amphiphilic polymers. The system size is quite computationally challengeable. As Figure 3.7 shows, six replicas are far from enough due to their non-overlapping probability for water solvated cyclic polymer system.

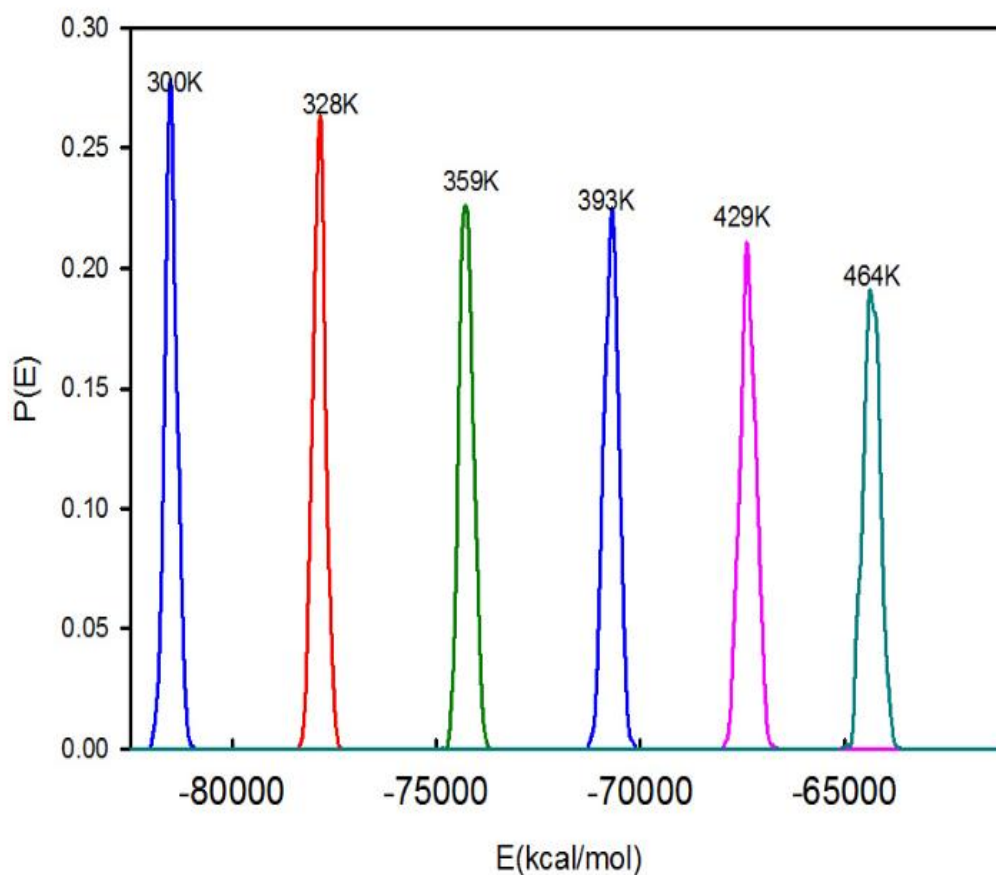


Figure 3.7 Probability distribution of potential energy for six separating replicas.

To realize feasible exchange within neighbor replicas, probably seven replicas are demanded to cover up one gap of those six potential energy barriers. Therefore, approximately 44 to 45 replicas would be utilized followed conventional replica

exchange methods. The heavy computational burden would be enforced to implement such simulations. The replica exchange with driven scaling (REDS2) method implemented within AMBER 11 was used for all simulation in tackling such technical problem. In REDS2 method⁷⁷, the potential energies of selected replicas are modified, according to following equation 3.1

$$E_{\lambda}(r) = \left[\frac{T_M}{T_A} \lambda + \frac{T_M}{T_B} (1 - \lambda) \right] E(r) \quad (3.1)$$

Where T_M is the temperature of the scaled replica, T_A and T_B are the temperatures of the neighboring un-scaled replicas, and $E(r)$ is the standard potential energy of the system. The scaling parameter λ varies from 0 to 1, allowing for high probabilities of accepted exchanges with the replica at temperature T_A when λ is near 1 and the replica at T_B when λ is near 0. Such scaling replica allows for a single replica to span a wide range of energies and to replace a number of conventional replicas. λ is treated as dynamically variable just as λ -dynamic application in the extended Lagrangian methods such as Car-Parinello⁸⁰, fluctuating charge⁸¹ and Nose-Hoover simulations⁸². λ is made to vary from 0 to 1 over a time scale τ as $\lambda(t) = \sin^2(\pi t/\tau)$. Over the range of replica temperatures, scaling replicas replaced of conventional replicas. Applying such strategy, the separating replicas between 300K and 328K can be correlated with swaps much more easily comparing with conventional method as Figure 3.8 indicating.

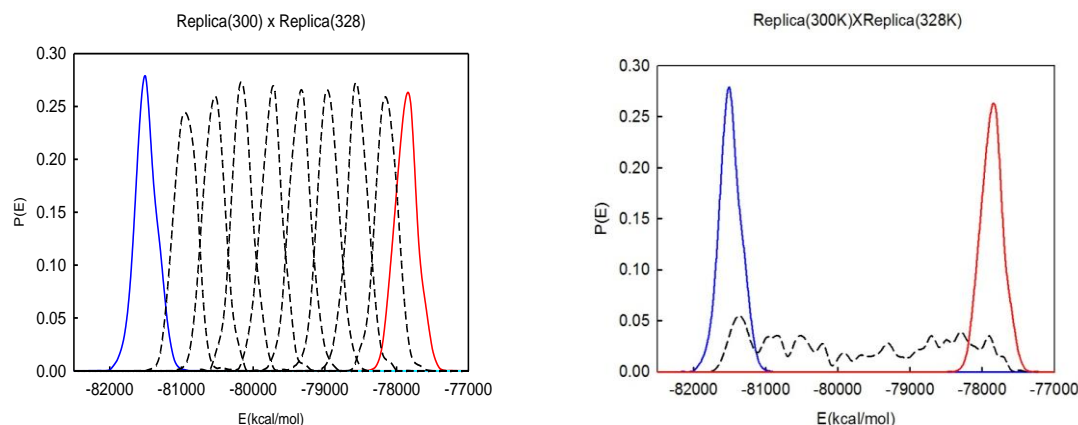


Figure 3.8 Left Figure shows seven replicas are required to fill in the potential energy barrier, right figure demonstrated a wide distributed scaling replica large enough to fill in the gap.

Figure 3.9 demonstrated the probability distribution at various replicas after performing REDS2 simulation in 2ns. It can be manifested that the REDS2 distribution migrated among different ensembles. With sufficient time of simulation, the swap between highest temperature and lowest temperature will be achieved eventually. As Figure 3.10 indicated, the structural information (radius of gyration of alkyl arms) obtained from REDS2 simulation is superior comparing with Classical Molecular Dynamics Simulation (MD) in two aspects. Firstly, higher fluctuation would surely enhance sampling efficiency. Secondly, REDS2 assists simulation reaching equilibrium in less computational time. Therefore adapting REDS2 methods to simulate macromolecule system is an efficient method not only in reducing computation time but also in providing concise molecular information.

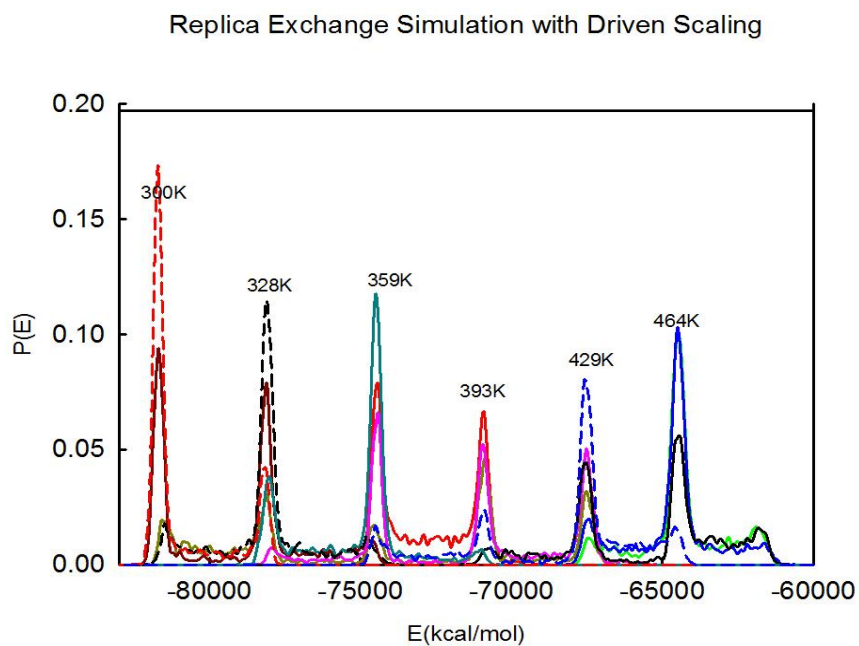


Figure 3.9 Replicas Exchange Simulation with Driven Scaling (REDS2) ensures six replicas exchange their information sufficiently.

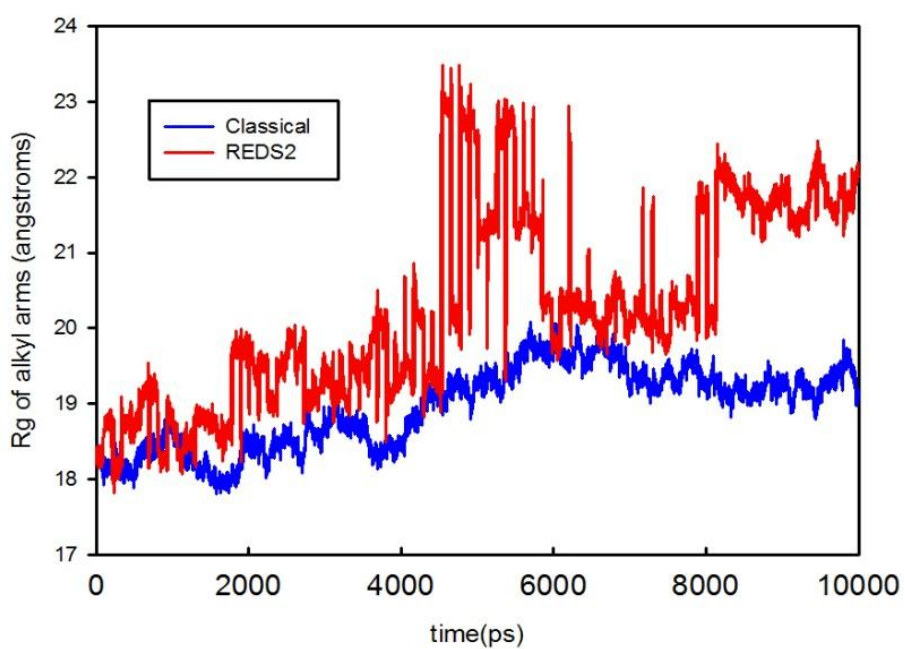


Figure 3.10 Radius of gyration of alkyl arms as a function of time: blue line represents the data obtained from classical simulation. The red line represents the data obtained from REDS2 simulation.

3.3 Materials and Simulation Methods

The linear and cyclic amphiphilic homopolymers were prepared using LEaP module in AMBER 12⁷⁸. The amphiphilic unit of the linear and cyclic polymer includes a dodecane chain and a tetra (ethylene glycol) chain attached to a tris-alcohol core. There are 115 atoms in the monomeric units and the linear polymer model consists of 40 monomeric units whereas the cyclic polymer consists of 32 monomeric units. Quantum mechanical calculations were conducted to obtain the charges for the polymer system using GAUSSIAN 09 packages⁴² at the MP2 level with a cc-pvtz basis set⁴³. The atomic partial charges for the molecules were obtained through electrostatic potential fitting methods. All other parameters for the polymers were taken from the general AMBER force field (GAFF)⁸³. The GAFF force field was used because it has been demonstrated to be accurate in simulation of organic liquids^{84, 85}, membranes⁸⁶, and polymers⁸⁷. Simulations were performed for water and toluene. Explicit water molecular dynamics simulations were performed with TIP4P/2005²⁴ water model. The toluene parameters were taken from GAFF also. Both the linear and the cyclic polymers were solvated using 8000 water

molecules. In the case of toluene 1500 toluene molecules were used to solvate the polymer systems. All the simulation system size are summarized in⁸⁶ table 3.1

Solvent Polymer	Toluene	Water
Linear Polymer	27213	36713
Cyclic Polymer	26201	35701

Table 3.1 Various simulated polymer system size.

Molecular dynamics simulations were performed in the canonical ensemble. Before initiating replica exchange moves, each replica was pre-equilibrated for 1 ns. The production simulations were run for 20 ns. Twelve replicas were used in our simulations spanning from 300 to 500 K, with temperatures equal to 300, 314, 328, 344, 359, 376, 393, 411, 429, 447, 464 and 482 K. Of these 12 replicas, we used six un-scaled replicas ($T = 300, 328, 359, 393, 429$, and 464 K) and six scaled replicas ($T = 314, 344, 376, 411, 447$ and 482 K). The Hamilton scaling time τ was set to 120 ps, which ensures the scaled replica remains in equilibrium⁸⁸.

3.4 Results and Discussion

3.4.1 Structure of Linear and Cyclic Polymers in Solvents of Varying Polarity

Representative simulation snapshots after 20ns of the linear and cyclic polymers in water and toluene at 300K are provided in Figure 3.11. The linear polymer adopts a relatively extended conformation in both solvents, whereas the cyclic polymer is more compact as a result of its internal topological constraints. The peripheries of both polymers in water appear to be more compact than in toluene. Specifically, the oligomeric PEO side chains appear to lie on top of an alkyl arm core in water for both the linear and cyclic polymers (Figure 3.11), while the polymer backbone is buried beneath the alkyl layer. Rather than switching positions, in toluene both the PEO and alkyl side chains appear to swell, giving the polymers a "hairier" appearance. This observation suggests the PEO arms are more soluble in toluene than the alkyl side chains are in water. Indeed, PEO sits on the edge of solubility in water, exhibiting surface activity⁴⁹ and a lower critical solution temperature, above which the polymer phase separates from aqueous solution⁵⁰.

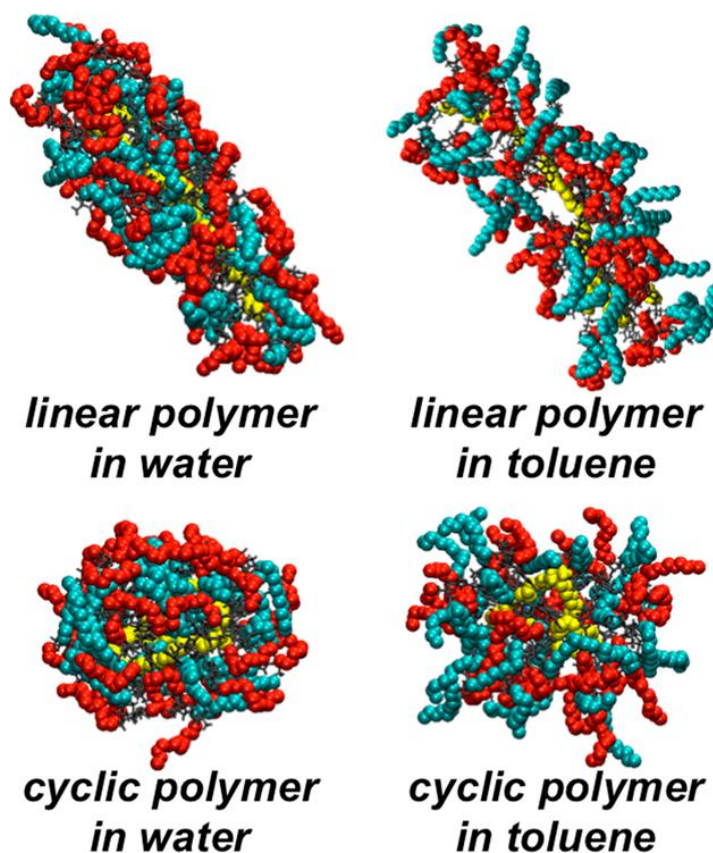


Figure 3.11 Representative simulation snapshots of the linear and cyclic amphiphilic polymers in water and toluene at 300 K after 20ns. The polymer backbone, alkyl side chains and oligomeric PEO side chains are illustrated as yellow, cyan, and red van der Waals surfaces. Connecting units attaching the side chains to the backbone are illustrated as dark sticks

3.4.2 Radii of Gyration

The relative polymer sizes and positioning of their constituent units can be characterized by their radii-of-gyration (Table 3.2) and radii-of-gyration probability distributions (Figure 3.12 and Figure 3.13). The instantaneous radius-of-gyration (R_g) of a polymer,

or subset of constituent polymer atoms, is determined by the expression like following equation,

$$R_g = \left(\frac{\sum_i \|r_i - r_{com}\|^2 m_i}{\sum_i m_i} \right)^{\frac{1}{2}} \quad (3.2)$$

Where the sum extends over the N atoms of polymer, or subset of atoms, where r_{com} is the center-of-mass position. In both water and toluene, the cyclic polymer has a smaller radius than its linear counterpart, resulting from the internal constraints imposed to create a macro-cycle (Table 3.2)

	polymer	backbone	alkyl arms	PEO arms
	(Å)	(Å)	(Å)	(Å)
<hr/>				
linear in water	21.6	18.0	21.1	23.1
linear in toluene	25.7	22.0	27.8	25.8
cyclic in water	16.5	9.1	16.4	19.2
cyclic in toluene	18.9	9.2	23.8	19.4

Table 3.2 Average Radii of Gyration of the Linear and Cyclic Amphiphilic Polymers, Their Backbones, the Hydrophobic Alkyl Arms, and the Hydrophilic PEO Arms in Water and Toluene at 300 K

Indeed, although the backbone R_g distribution for the linear polymers shifts to greater radii upon transfer from water to toluene (Figure 3.12), reflecting the fact that toluene is better solvent for the backbone than water, the backbone distribution of the cyclic polymer barely changes (Figure 3.13). Nevertheless, the overall dimensions of both polymers swell in toluene compared to water, (Table 3.2), suggesting that on average toluene is a better solvent than water for these polymers and their constituent units.

In water the R_g distribution of the PEO arms of the linear and cyclic polymers are greater than those of the alkyl arms (Figure 4 and Figure 5). As expected, the relative positioning of PEO and alkyl arms switch in toluene, with the radii of the alkyl arms being greater than PEO. In addition, the radii of the side chains are greater than that of the backbone, indicating the backbone is enshrouded beneath the side chains. Upon transfer from water to toluene, the PEO arm R_g for the linear polymer slightly swells whereas it barely moves for the cyclic polymer (Table 1). The swelling of the PEO chains for the linear backbone in toluene existed, which is absent in the case of the cyclic polymer. The main reason leading such results comes from the lighter constraints enforcing on the macro-cycle structure comparing with linear structure. Indeed, the PEO R_g distributions for the cyclic polymer in water and toluene are nearly super-imposable on one another (Figure 3.13). The largest dimensional change upon transfer is observed for the alkyl side chains, which significantly extend into toluene.

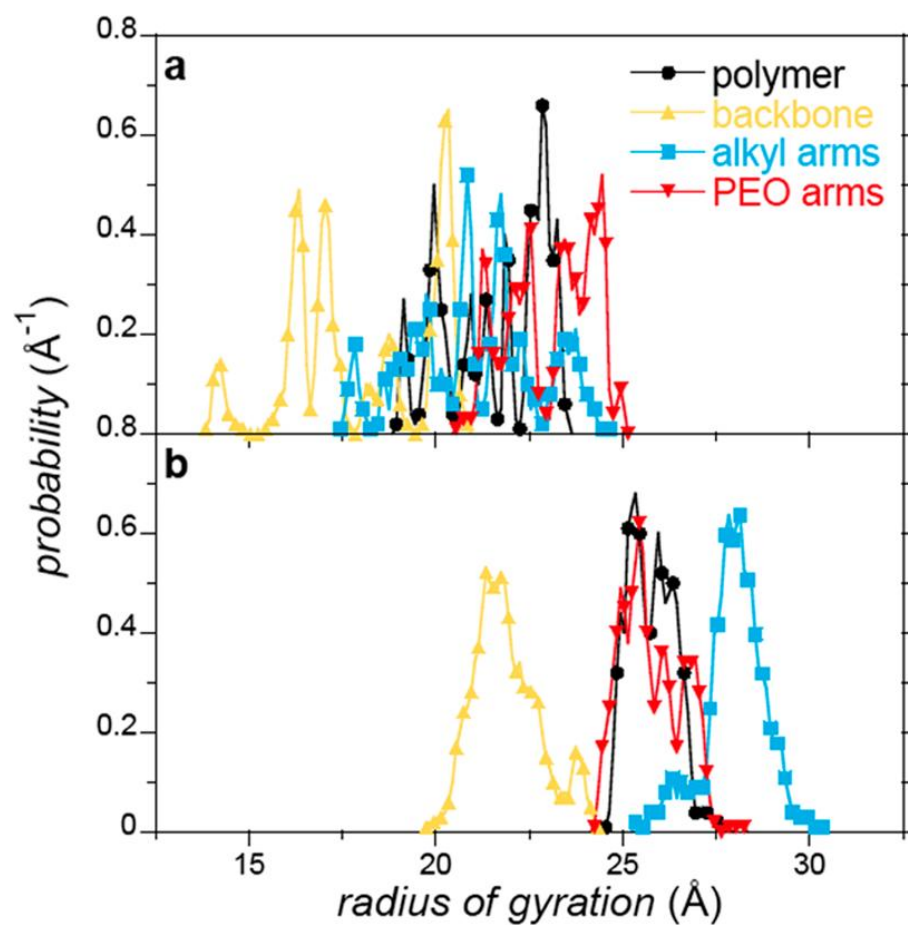


Figure 3.12 Radius-of-gyration probability distributions for the linear polymer and its constituent groups in water (a) and toluene (b) at 300 K. The figure symbols are defined in the legend provided in (a) The probability distributions are normalized as $\int \rho(R_g) dR_g = 1$.

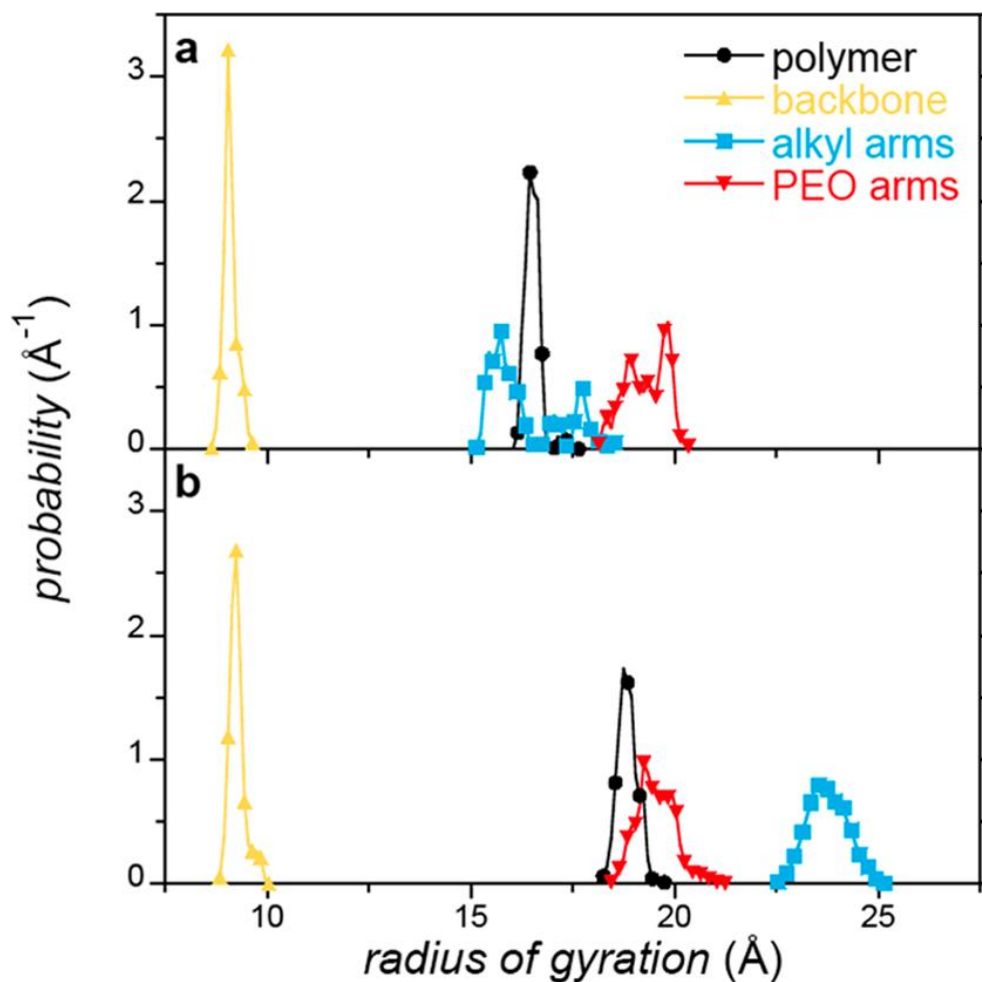


Figure 3.12 Radius-of-gyration probability distributions for the cyclic polymer and its constituent groups in water (a) and toluene (b) at 300 K. The figure symbols are defined in the legend provided in (a). The probability distributions are normalized as $\int \rho(R_g) dR_g = 1$.

3.4.3 Density distribution function

The solvent and polymer unit density distributions about the center-of-mass of the cyclic polymer in water and toluene are plotted in Figure 3.13. We only plot density distributions for the cyclic polymer because it has a more compact, spherical structure

than the linear polymer as snap shots indicating, which exhibits smeared density over a wider range of separations. In water, the PEO arm carbon and oxygen atoms predominantly reside on the surface of the assembly (Figure 3.13a); with a single peak in the neighborhood of the PEO arm R_g (Table 3.2). The alkyl arms, on the other hand, exhibit two peaks, an outer peak at a separation comparable to the alkyl arm R_g and a more prominent inner peak near the COM. This inner alkyl peak lies inside the backbone density distribution, suggesting that some of the alkyl chains do fill the core, though the majorities are outside the average radius of the backbone. This makes the center of the polymer a significantly non-polar environment. Water is repelled by the polymer core and its density falls to essentially zero below the layer of PEO side chains. The PEO arm density distribution is only weakly perturbed upon transfer to toluene. There is a slight presence of PEO chains inside the average backbone radius, however, only to a limited extent when compared to the alkyl rich core when observed in water. The outer alkyl arm density peak swells to a separation outside the PEO distribution when in toluene (Figure 3.13b). This observation is consistent with the changes in the R_g of the constituent polymer units within transferring from water to toluene reported above. The swelling of the outer alkyl peak is supplied in part by the pool of alkyl units at the polymer center, resulting in a slight depression of the inner peak density. In difference to water, toluene is

able to penetrate the core of the cyclic polymer, suggesting a polymer owning higher solubility for non-polar solvent than polar solvent.

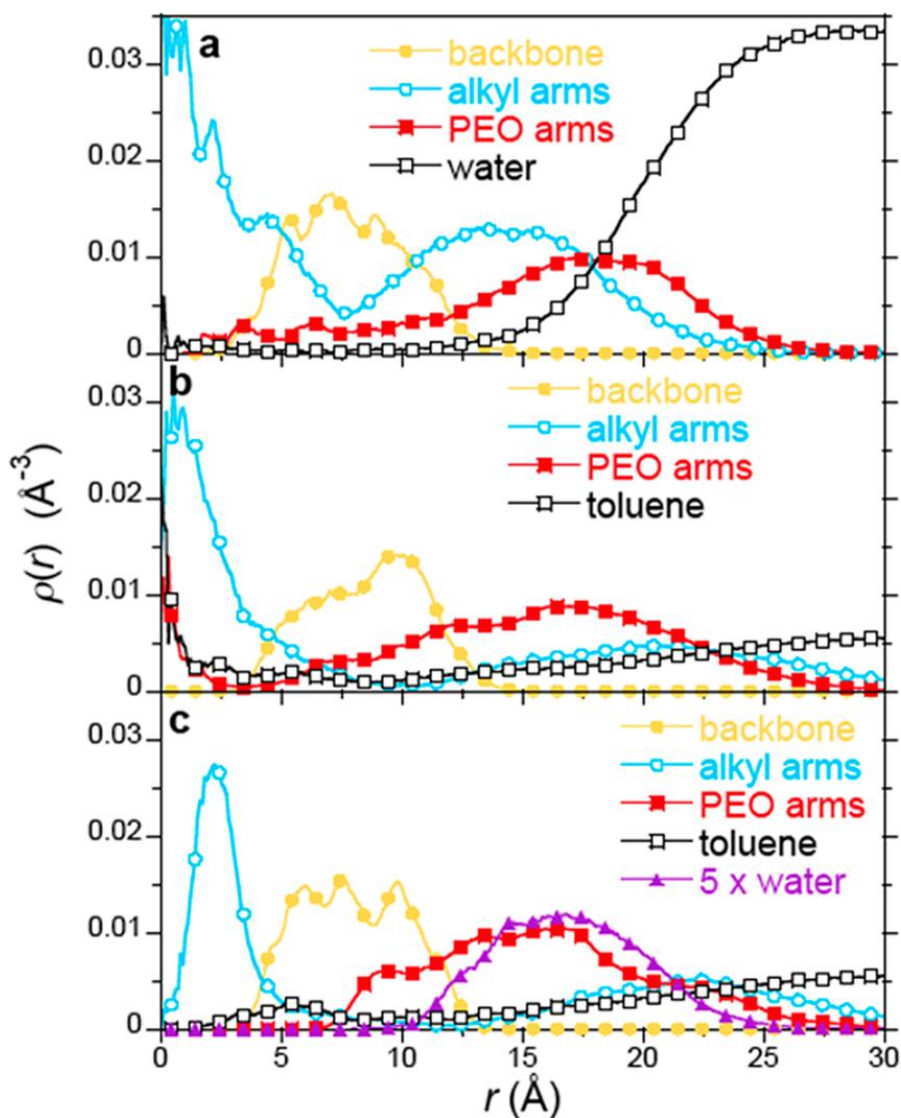


Figure 3.13 Heavy atom density (not include hydrogen) as function of distance from the cyclic polymer center-of-mass for the polymer backbone, alkyl arm, PEO arm units in water (a), toluene (b), and water/toluene mixed (c) solvents at 300 K. Figure symbols are defined in the inset legends.

3.4.4 Instantaneous Liquid Surface.

Density distribution function is a classical method to characterize molecular structure taking an inside-out center-of-mass based perspective on polymer structure. It has already rendered a directed recognition to us about what's the basic polymeric material orientation. However, the radiating area is increasing as a function of squared radius. Therefore the observed scale of the periphery area of the system is limited considering the volume factors. An alternate outside-in-perspectives can be achieved by determining an instantaneous surface encapsulating the polymer at each moment during the simulation and evaluating the alkyl and PEO arm distributions relative to that interface, which is determined here using the definition of Willard and Chandler⁸⁹. Details of analysis are implemented in following procedure with a demonstration in Figure 3.14.

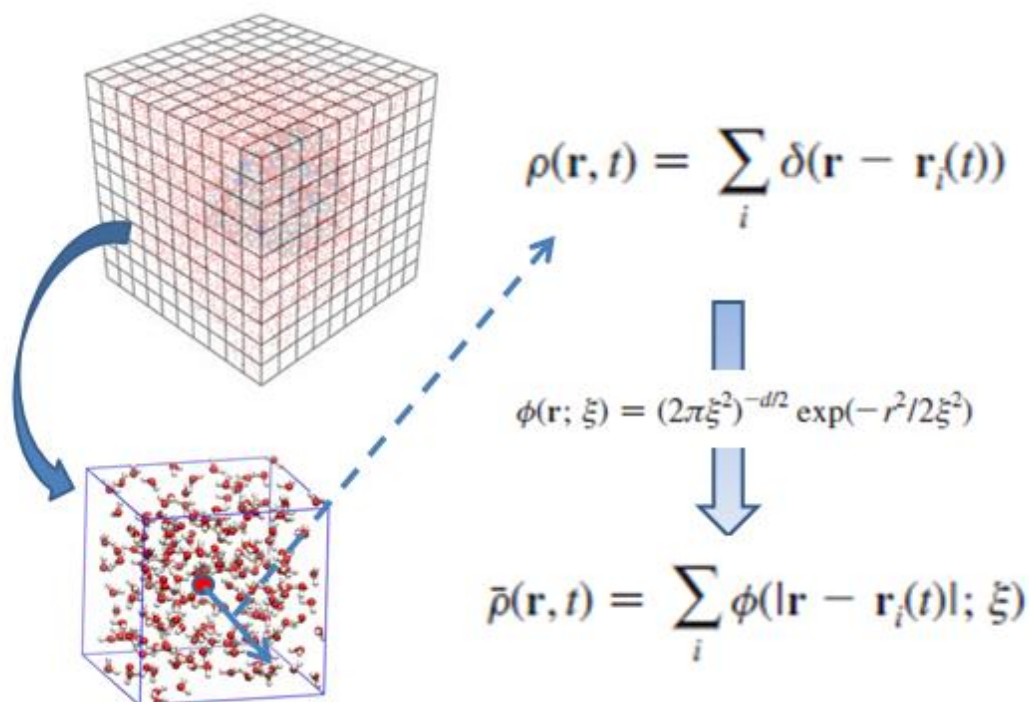


Figure 3.14 A simple demonstration of instantaneous liquid surface construction. Simulated system was coarse-grained into small cells. Retrieving one of the small cells, a calculation of distance relating center position to surrounding can be integrated into a delta function. Within Gaussian approximation of the delta function, an average density function can be subsequently derived.

The simulated system is coarse-grained into $70 \times 70 \times 70$ cells to ensure the cell size is one \AA^3 . The normalized Gaussian function is used to feasibly describe the instantaneous delta function, where λ is the smearing length, at each heavy atom site of the solvent and determining the surface at which the smeared density is equal to half of the bulk solvent density. This approach has been previously applied to determine the dynamic interfacial properties of protein assemblies in water. Here we assign a value of $\lambda = 2.4 \text{ \AA}$ to the

smearing length, which is comparable to the correlation length for water. As Figure 3.15 shows, we can actually mapped out the water density distribution surrounding the polymer using this method and visualize the instantaneous shape of polymer dynamics.

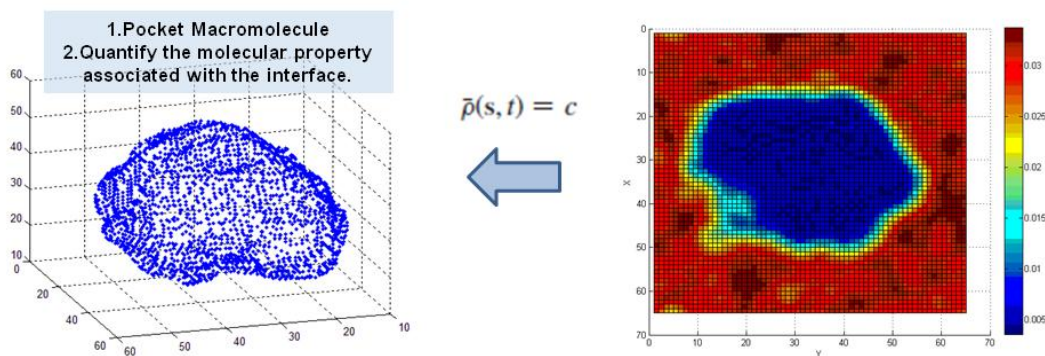


Figure 3.15 Demonstration of mapping density function surrounding cyclic polymers system (right) through projection at the center of system. Through defining a constant density (half of the bulk density), a 3-dimension pocketed macromolecule can be displayed.

One of interesting features by employing such interfacial analysis techniques is to quantify the molecular properties associated with the interface. Our approach is through identifying the most approximate distance between scattering interfacial mesh point and interested heavy atoms. In that we basically depicted a normal distance between liquid interface and heavy atom sites. As Figure 3.16 shows, the atoms closer to COM located at the longer distance position (green line), the atoms further from COM located at the shorter distance position in the distribution figure.

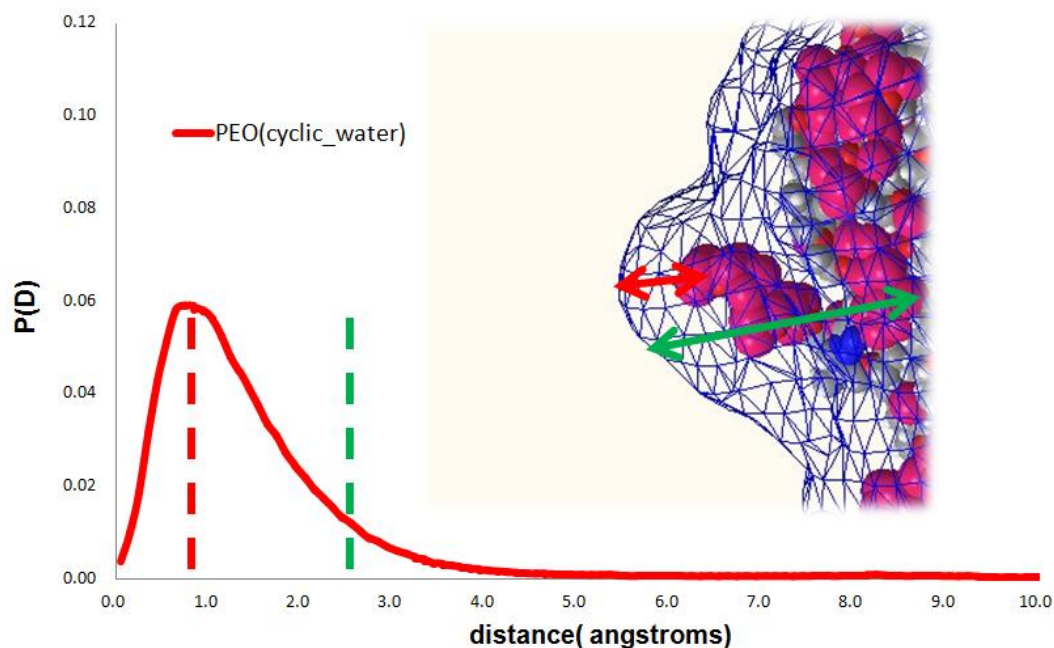


Figure 3.16 Demonstration of distribution of PEO arms' atom for cyclic polymer in water system as function of instantaneous liquid surface distance.

The instantaneous interface-side chain heavy atom distance distribution function for the alkyl and PEO arm side chains of the linear and cyclic polymers in water and toluene are reported in Figure 3.17. We noted that short distances in these distributions correspond to the heavy atoms being closest to the solvent interface and further away from the polymer center. In water the PEO arms sit closet to the interface, as indicated by the prominent peak at ~ 1 Å, while the alkyl side arm atoms are spread out further from the interface. In toluene, both the alkyl and PEO heavy atoms reside approximately 0.5 Å from the interface; however, the alkyl atoms display a larger, more prominent peak than the PEO atoms. Most interestingly, the distributions of the alkyl and PEO arms for the linear and

cyclic polymers in both water and toluene are practically identical, barring minor differences. So although distinct differences in the structures of the linear and cyclic amphiphilic polymers based on a center of mass analysis are observed, from the outside-in the polymers are nearly identical. We conclude then that the major structural differences observed during the center-of-mass based analysis results from polymer backbone topology effects, and that the impact of the solvent on the ordering of the alkyl and PEO arms is largely independent of that topology.

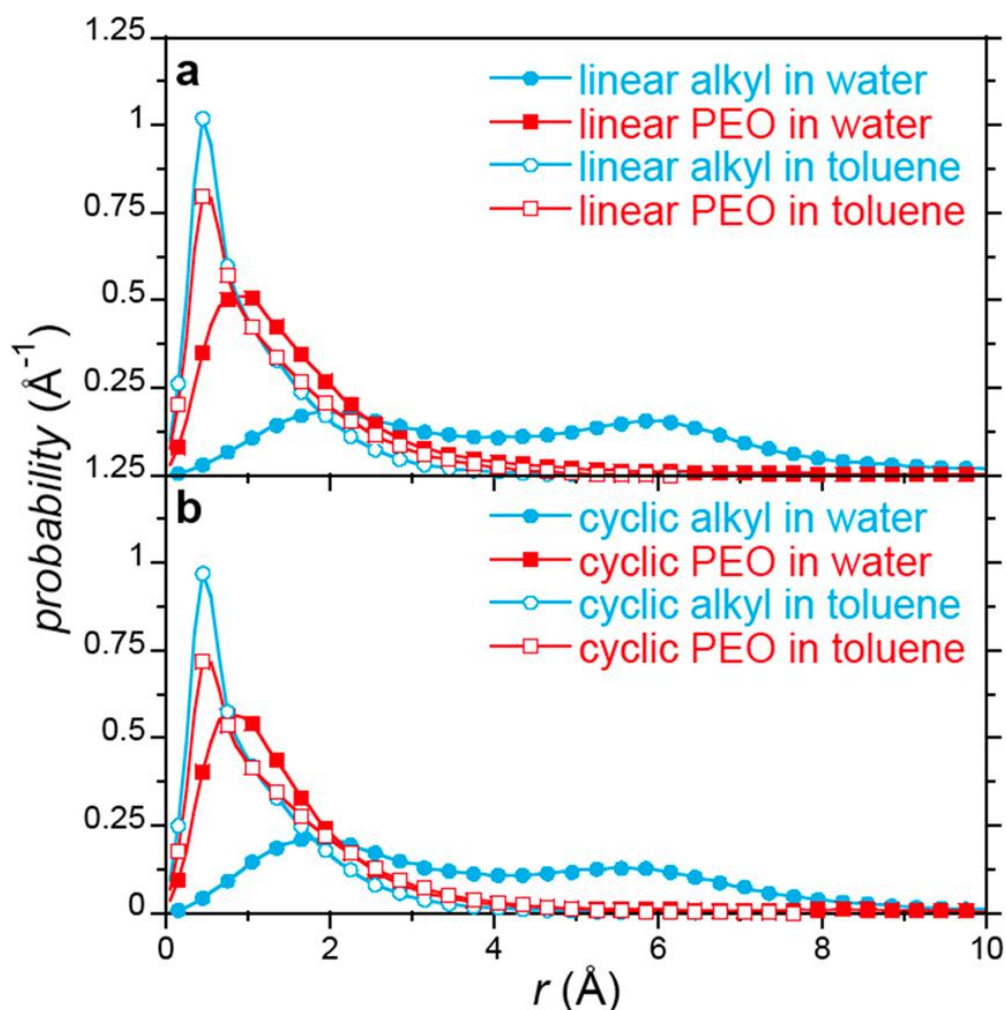


Figure 3.17 Instantaneous solvent interface-side chain heavy atom distance distribution functions for the PEO and alkyl heavy arms for the linear (a) and cyclic (b) polymers in water and toluene at 300 K. Figure symbols are defined in the inset legends. The probability distributions are normalized as $\int \rho(R_g) dR_g = 1$.

3.4.5 Capacity to Deliver Hydrophobic and Hydrophilic Moieties.

The structural analysis indicates that primary response to the difference solvent environments involves movement of the alkyl arms. The asymmetric redistribution of the alkyl and PEO side chains in water and toluene begs the question, are the observed conformational changes significant enough to impact the capture and release of hydrophobic/hydrophilic guests in differing solvent environment? To answer such curiosity and to assess the capacity of these polymers to deliver hydrophobic guests from an aqueous to an organic environment, we have evaluated the potential-of-mean force (PMF) between argon and these polymers in water and toluene. PMFs were evaluated by determining the excess chemical potential of argon as function of distance from the polymer center of mass out into the bulk solvent using the test particle insertion method. The distance dependent excess chemical potential, $\mu_{Ar}^{ex}(r)$, is evaluated as

$$\mu_{Ar}^{ex}(r) = -kT \ln \langle \exp[-\frac{\varphi_{solvent-Ar}(r)}{kT}] \rangle_0 \quad (3.3)$$

Where kT is the product of Boltzmann's constant and the temperature, $\varphi_{solvent-Ar}(r)$ is the total solvent-argon interaction energy r away from the polymer center of mass, and the

brackets $\langle \dots \rangle_0$ indicate a canonical ensemble average over configurations obtained in the absence of a guest. In these calculations argon was modeled as a Lennard- Jones particle $\sigma_{\text{ArAr}} = 3.415 \text{ \AA}$ and $\epsilon_{\text{ArAr}} = 1.0393 \text{ kJ/mol}$.

Widom insertion method belongs to one of the perturbation theory methods which requires relative large amount of trials to ensure accurate statistical average. For large systems, adequate insertion trials as long as computational time are in need. Therefore, we have to improve Widom insertion methods through updating calculating algorithms. In MD simulation mostly two kind algorithms are adapted: neighbor-list and linked-list. Basic ideas of these two algorithms are same: It is sorting out atom numbers sequentially in decreasing searching scale of long-ranged interactions since most time long-ranged interactions contribute trivial influence to the results. Neighbor list method achieved so by adding an extending shell of cut-off distance and updating atom numbers within exterior shell. On the other hand, linked-list method is dividing the simulation box into small cells of equal size and sequentially marking atom No. in each cell. After sorting, a classical sequential counting is transformed into a two-dimensional array of re-constructing data. For Widom insertion coding technique, a subroutine of the linked - list algorithm was embedded in the analysis code. The data struts were updated for every configuration. As shown in Figure 3.19, while implementing one insertion, the inserting atom is located at central cell. Meanwhile it begins to search neighbor cells' head atom

and subsequently collect atom positions' information of each cell. The range of neighbor cells was extended to surrounding 74 cells, which almost counter fluctuation in a certain range. Within applying the linked - list algorithm, we found the computation speed was enhanced three times. Based on our studies, such approach should be an essential technique incorporated in large-scale simulation system.

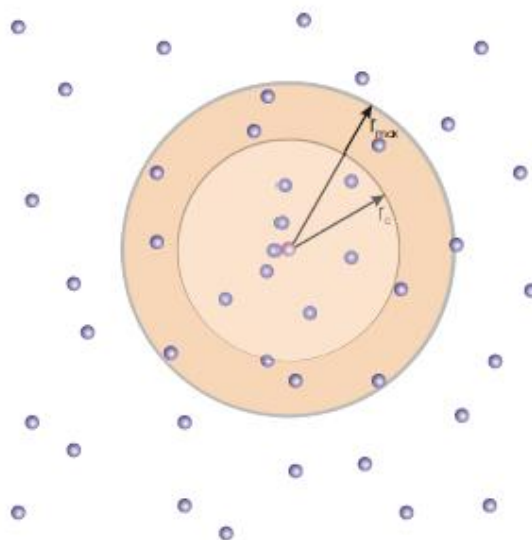


Figure 3.18 Schematic demonstration of neighbor list methods. Every molecule stores its neighbor atoms for a distance $r_{\max} > r_c$ in a formatted list and such list is updated every n_{upd} time steps.

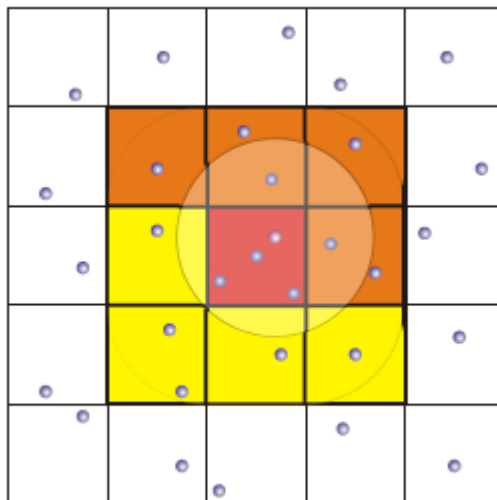


Figure 3.19 Schematic demonstration of linked-list algorithms. Molecules were arranged in a lattice of cubic cells of side-length r_c . The red cells represent the inserting central position's cell. The yellow cells represent the cells consisting of short-range interacting neighbor atoms. (In practical operation there are more cells in three dimensions)

The PMF between argon and cyclic polymer in water (Figure 3.20) shows a distinct preference for the polymer interior. Specifically, the excess chemical potential of argon drops from a very unfavorable 8.6 kJ/mol in bulk water to a more favorable plateau of ~ 4 kJ/mol in the polymer between separations of 5 - 15 Å in the periphery of the assembly structure where the water density has dropped to nearly zero. Between 0 to 5 Å the PMF exhibits an even higher affinity well in the vicinity of the alkyl arm enriched center of the polymer. Also shown in Figure 3.21, the PMF between argon and the linear polymer in water is essentially the same as that for the cyclic polymer except it does not exhibit deeper inner minimum because the center-of-mass for the linear polymer is occluded by

the polymer backbone. In toluene, the PMF displays a broad plateau of ~ 4 kJ/mol inside the cyclic polymer assembly that drops to 2.5 kJ/mol in the bulk solvent. On the basis of these PMFs, then we expect model hydrophobic species, like argon, to partition into the amphiphilic polymer's hydrophobic interior in water and into the bulk solvent in toluene.

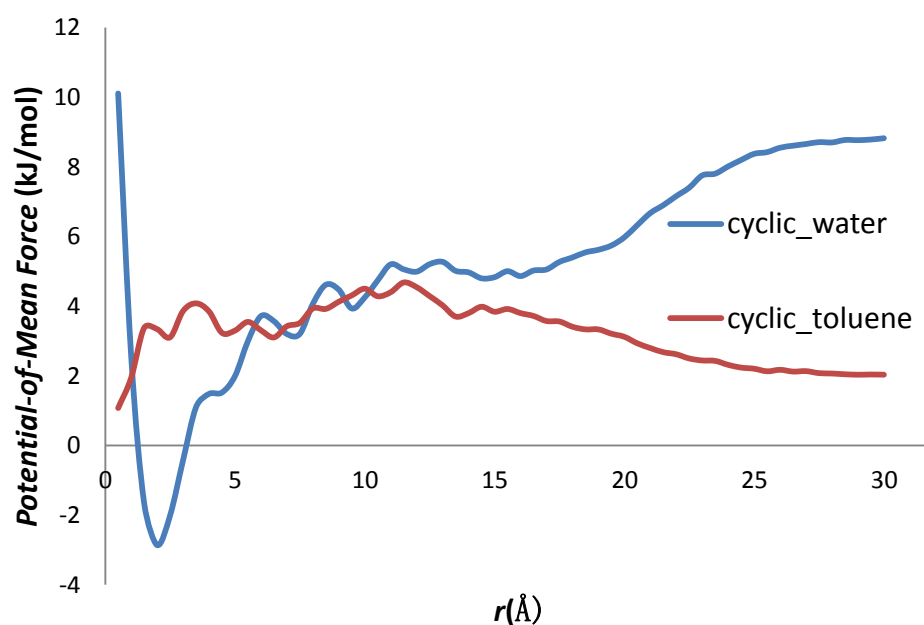


Figure 3.20 Argon excess chemical potential as a function of distance from the cyclic polymer center-of-mass in water and toluene at 300K. Figure symbols are defined in the inset legend.

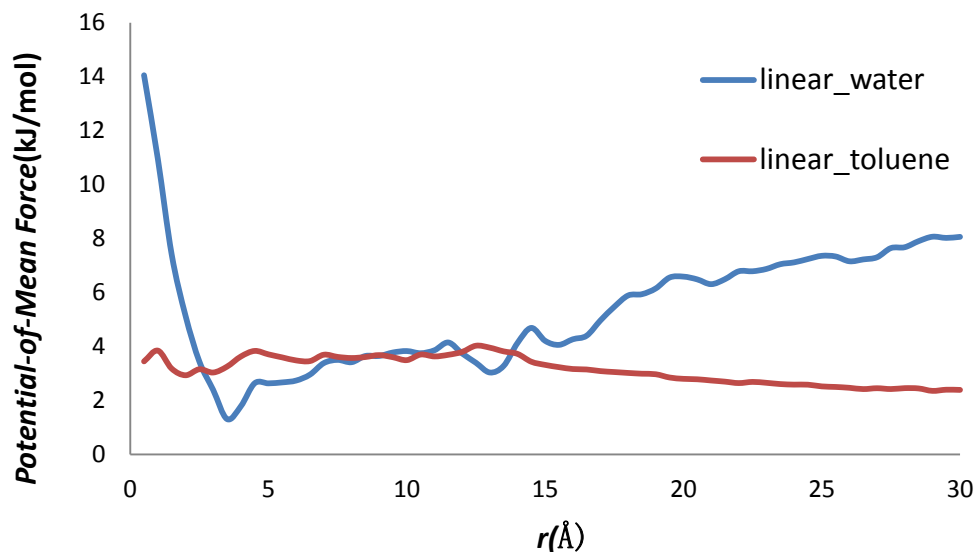


Figure 3.21 Argon excess chemical potential as function of distance from the linear polymer center-of-mass in water and toluene at 300K. Figure symbols are defined in the inset legend.

Since most hydrophilic species are electro-statically active also they own high orient degrees-of-freedom which will reduce the probability of successful insertions. It's difficult to implement a hydrophilic test vice versa. Arjun implemented another approach by adding 75 water molecules to cyclic polymer in toluene system and examined the affinity of water as a model polar guest for the cyclic polymer interior in an organic environment. The local density of water as function of distance from the center of mass for the cyclic polymer in water is shown in Figure 3.13c after 20ns of simulation. The water density shows a prominent peak that coincides with the PEO arm density between backbone and alkyl arm peaks, corresponding to the highest polarity portion of the

polymer in toluene. This is distinct to simpler ideas that envision hydrophilic guests settled into the hydrophilic center. Integrating the polymer density from the center-of-mass out to the periphery at 25 Å, about 72 of the 75 added water molecules are soaked up by the polymer, indicating both a strong preference of the model hydrophilic guest for the polymer in toluene and a significant carrying capacity. We also have performed a counterpart simulation dissolving 40 toluene molecules in 8000 water and polymer system. A similar phenomenon was found that about 80% toluene molecules were absorbed into the polymers. Consolidating all the observed results including polymer's preferential uptake of argon in water followed by release in toluene, the uptake of water in toluene as well as the uptake of toluene in aqueous solution, all the evidences supported the capacity for these amphiphilic polymers to act as delivery vehicles triggered by changes in solvent polarity. More importantly, the ability of our simulations to capture this experimentally documented capability lends evidence that the REDS2 enhanced sampling technique is capturing relevant conformational change essential to model delivery from a molecular perspective.

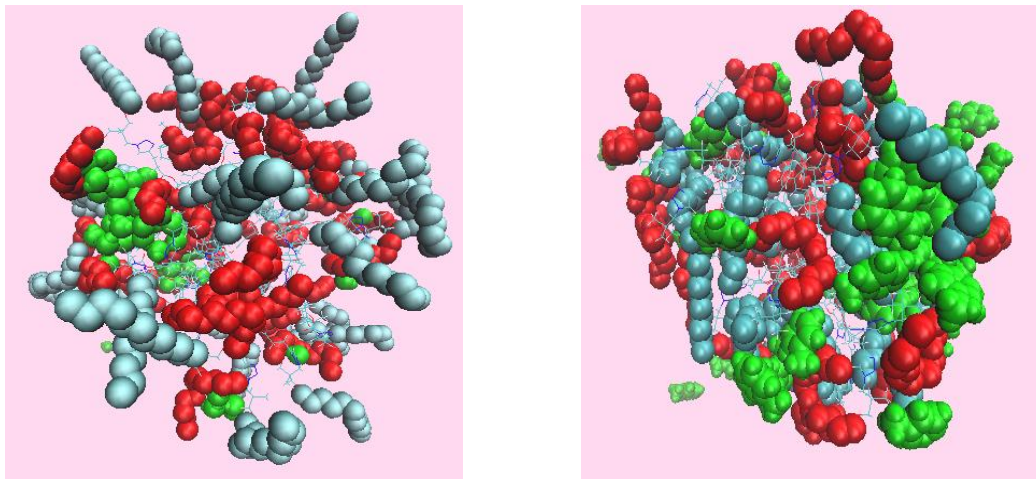


Figure 3.22 Uptake mixing immiscible solvents by polymer: cyan balls represent heavy atoms of alkyl arms, red balls represent heavy atoms of PEO arms. Green represents incompatible solvents which are water molecules (left) and toluene molecules (right) respectively.

3.5 Conclusion

Above structural analysis indicates that the most basic model that the cyclic chain inverts when transferred between a polar and non-polar solvent is too simple. The structural analysis was based on the radius-of-gyration of the characteristic parts of the polymer, the density distribution relative to the polymer center of mass, and the distribution of atomic distances from the instantaneous surface. Rather than a large structural inversion, the PEO chains appear to be equally solvated in both solvents and that the predominant changes in the polymer structure can be traced to changes in the alkyl arm distributions. In water the alkyl arms retreat beneath the PEO chain interfacial layer, on the contrary in toluene the alkyl arms swell beyond the PEO layer. For the cyclic polymer, a small pool

of alkyl arms resides in the assembly core near the similarly hydrophobic polymer backbone no matter the solvent polarity. The structural results of this study may provide guidance for the design of other amphiphilic polymers. The design strategy will be discussed in the next chapter.

Our results indicate the ability of the polymers to bind either hydrophobic or hydrophilic guests. Argon, a model hydrophobic guest, can bind to a variety of positions inside the polymer resolving in water or toluene resulting free energy gain to bind relative to solvent. Water molecules, as prototypes for hydrophilic guests, bind to positions close the PEO arms while in toluene solvent and not in the center. Near the center is the polymer backbone, which is hydrophobic. A more hydrophilic backbone might bring polar guests into the center. The conclusion that proposed drug delivery polymers may in fact bind drug molecules away from the center of the polymer was also reached in a simulation study by Swope et al⁹⁰. For star polymers with diblock arms, consisting of hydrophobic and hydrophilic segments. These results also suggest design strategies, as the side chains not only help to determine the polymer structure but also bind guests.

Chapter 4

Design of Tailored Polymer via Molecular Simulation

4.1 Introduction

Contents of previous chapters unfolded our molecular modeling strategies and simulation techniques to investigate polymer systems not only in understanding their interesting molecular features but also in probing molecular interaction's mechanisms. The next question is will the molecular simulation be used to propose a rational design scheme accordingly? In Pharmaceutical industries, Molecular Dynamics simulations integrated with quantum mechanics techniques have been adopted as an efficient approach to implement Computed-Aided Drug Design (CADD). Molecular Dynamics Simulations were employed to study structural dynamics or binding affinities between drug moieties and targeted protein/enzyme through statistical thermodynamics approach⁹¹. Accompanying that there have been quite number of successful stories either about developing novel fast screening algorithms⁹² or searching interacted binding site⁹³⁻⁹⁵. Besides major successes in biology sector, MD simulations also extended their

applications in assisting design in engineering fields. Yang and Pratt employed first simulation of electric double-layer capacitors based on nano-tube forests modeled fully at a molecular level⁹⁶. Based on accurate prediction of experimental results, simulations were performed to assist designating various physical chemical factors including pore geometry, various filling of pores that contribute to enhance performance of electric storage materials⁹⁶. Wanjari and Ashbaugh studied the conformational change of alkane chains in a confinement of nano-tubes and observed an interesting phenomenon that narrower confinement actually force stronger entropic barrier while alkane chains "struggled" harder to escape from CNT. This simulation extended possibility of molecular modeling in understanding unrevealed details of existing NMR spectra measurement⁹⁷. Fiore and Garde cooperated experimental and simulation studies to take a insights of molecular orientation of Trimethylamine N-Oxide (TMAO) and tert-Butyl Alcohol (TBA) at hydrophobic interfaces which provided a molecular template on designing interfacial active small molecule applied in bio-absorbing or detaching surface⁹⁸. Karatasos studied the association effect of the Anti-Cancer Drug Doxorubicin with PEGylated hydrobranched polyesters in an aqueous solution. The dynamics motions of drug cluster indicated longer PEG arms enhanced nano-carrier's robustness in delivering moieties. They also proposed the hydrophilic arms' length as key parameter to be manipulated for drug delivery⁹⁹.

Within constitutively efforts from computational chemistry and physical chemistry chemists, polymersome materials have been extensively studied either in their fundamental nature or potential applications. The experimental researchers and theoretical researchers collaborated closely to examine polymer's chemo-physical properties and anticipated in reaching consistent views in terms of molecular design. Ballauff and Likos reviewed dendrimer studies based on theoretical modeling and simulation perspectives. They pointed out combination of simulation and analytical theories with experimental techniques such as small angle neutron scattering data should be a powerful tool to understand the complicated structural features of super-macromolecules such as dendrimer. Also they proposed future focus should be laid on the strategies of appropriately modifying the size, the end groups, charge during the preparation of dendrimer. Therefore from simulation aspect, a more realistic modeling potential such as force field and more incorporated parameters should be provided.¹⁰⁰. Hussain et.al also outlined a current simulation and modeling technique beneficial to polymer-matrix nanocomposites and pointed out that current simulation research had established trustable models and researchers should focus on applying such model/simulation in improving mechanical or transport properties of high-performance materials⁹⁵. Discher et.al reviewed drug delivery polymersome materials' emerging applications from computational molecular dynamics (MD) schemes to experimental

results¹⁰¹. Vesicles' formation and fissions' dynamics to mimic the micellar structure kinetics in real solution environment were the main challenging tasks and simulation groups have strived to understand such problems either using coarse-grained potential to overcome computational burden of large system¹⁰² or dissipative particle dynamics (DPD) method to overcome the limitation of time step-size¹⁰³.

Despite formidable challenges implementing atomistic level simulation for macromolecular systems, developing a consistent force fields modeling various types of polymer structure and substance have to be started from all-atom descriptions. The diversities of polymer geometry and composition actually increased the simulation's complexities more. Therefore the bridge between molecular level mechanisms and experimental observation is gradually built as scaling up of simulation but the scaling up of simulated system also brought uncertainty of simulated results and incapability enabling simulation. Because the ultimate goal of simulation is developing computational modeling as an effective tool to perform rational design of interested materials, therefore to tackle the existing scaling problem is essential not only for Molecular Dynamics simulation research groups but also to satisfy the quest from polymer science and engineering community. Continuous development of GROMACS³⁰, AMBER⁷⁸, CHARMM¹⁰⁴ established efficient platforms for large-scale MD simulation and a

open-source environment provided us basis to develop novel algorithms using existed modules.

Since we already mapped out an effective strategy that using the REDS2 technique to exploit a polymer's ability of carrying moieties, rational design of polymer can be employed by alternating existing molecules' functional groups accordingly. Several schemes are listed in Figure 4.2. One of the main issues about the PHS-yns macrocyclic polymer was the amphiphilic arms didn't undergo complete inversion. If taking a microscopic view from snapshots (Figure 3.11), the arms were fond of tangling with each other due to the natural affinity of non-polar parts existing in both hydrophilic and hydrophobic arms. What leading such consequence can be explained according to the unified weak or strong segregation block co-polymer theories developed by Matsen and Bates¹⁰⁵. Potentially immiscible Diblock copolymer would like to undergo phase transition and induced self-assembly of polymeric solvents to form various ordered morphologies. Chemical incompatibility of diblock monomer produced such phase separation originating from unfavorable entropic gaining while mixing. As equation 4.1 indicating, the interacting parameter χ_{AB} should be one of the parameters characterizing block copolymer's molecular structure.

$$\chi_{AB} = \left(\frac{Z}{k_B T} \right) \left\{ \epsilon_{AB} - \left(\frac{1}{2} \right) (\epsilon_{AA} + \epsilon_{BB}) \right\} \quad (\text{eq. 4.1})$$

Another factor characterizing molecular structure according to unified theory is the composition $f_A = N_A/N$

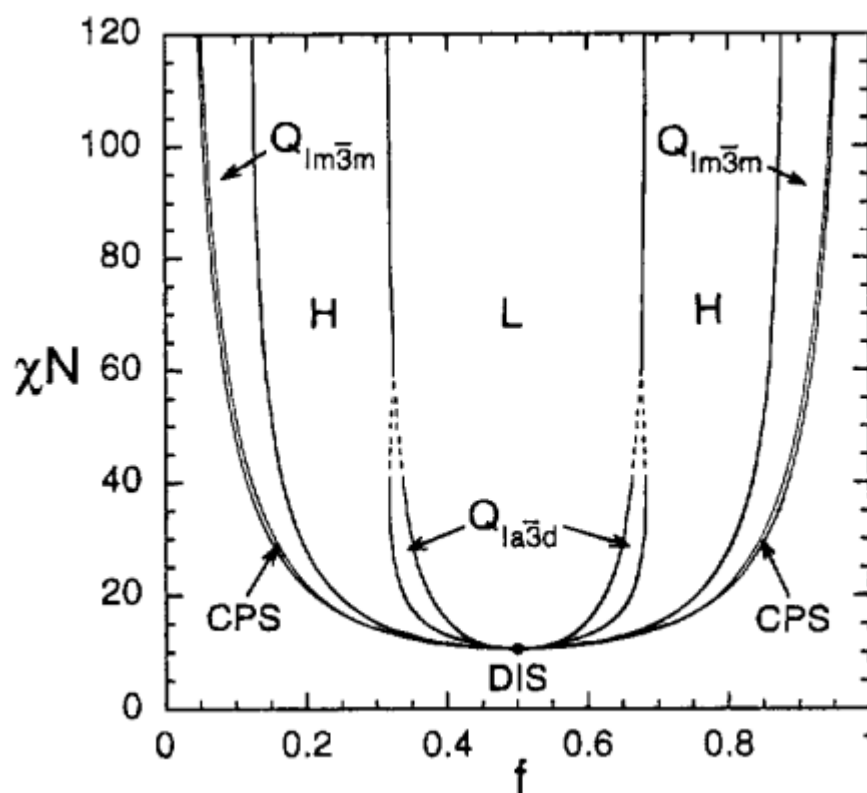


Figure 4.1 Mean-field phase diagram for conformationally symmetric diblock melts. Phase are labeled L (lamellae), H (hexagonal cylinders), Q_{Ia3d} (bicontinuous Ia3d cubic), Q_{Im3m} (bcc spheres), CPS (close-packed spheres), and DIS (disordered) obtained from Matsen and Bates's Unified Weak and Strong Segregation Theory. Dashed lines denote extrapolated phase boundary and the dot denotes the mean-field critical points¹⁰⁵.

Inspired by above diagram, Diblock co-oligomer of PEO and dodecane may co-existed at disordered phase or approached to the separation boundary since the oligomer length is quite short (6 units).

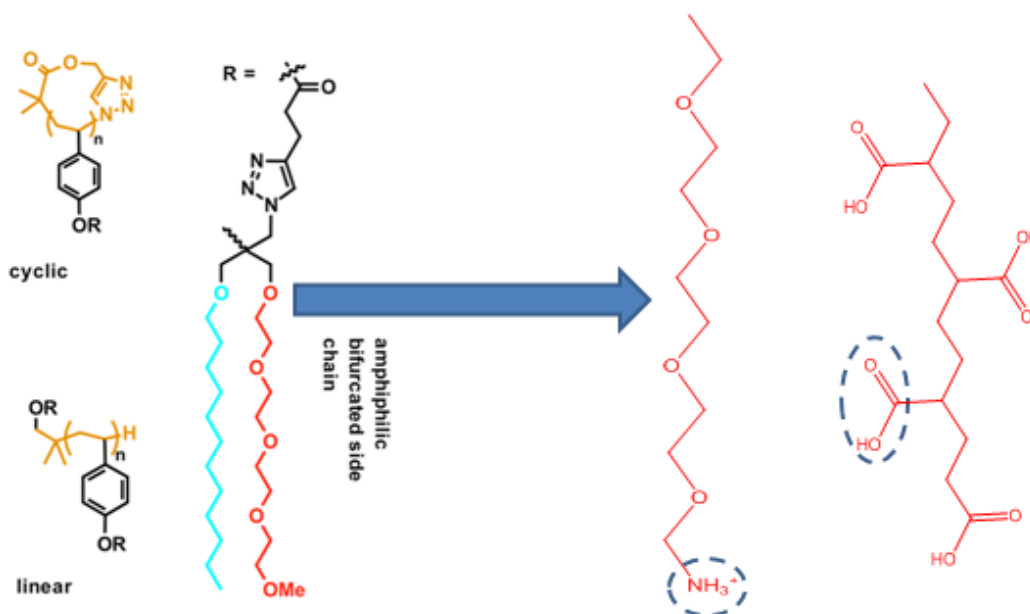


Figure 4.2 Two strategies potentially to designate polymer in strengthening arms' self-assembly structure: 1. terminated the PEO oligomer with a charged group. 2. Increase the hydrophilicity by alternating PEO based hydrophilic polymer to Polyacrylic units' base.

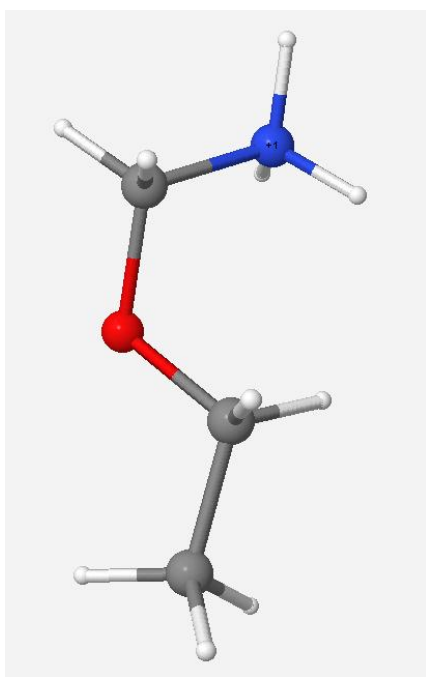
Indicated as Figure 4.2, two schemes were planned to be implemented. Firstly, according to the polarity being capable to tune the Flory-Huggins interacting parameter, we plan to introduce a bio-compatible charged amine group to terminate the hydrophilic arms. Second, more hydrophilic arms can be attached to the amphiphilic units by replacing PEO of Poly (acrylics) (PAA) oligomer. In addition, another possibility is alternating the alkyl polymer backbone into a more hydrophilic one. Collaborated with Dr. Rick's group, simulations were initiated to test above three strategies. For the current phase, I am

working on studying the effect of alternating terminating group from methyl group to NH_3^+ group.

4.2 Application and Validation of Proposed Design

4.2.1 Methods and Materials

Followed up with techniques' statements of previous chapter, we built up an initial configuration using LEaP module in AMBER 12³⁷. Since cyclic polymer exhibited more consistent results for analyzing, this time the only architecture we focused on is macro-cycle. The amphiphilic units still constituted a hydrophobic dodecane chain and polystyrene based backbone. Whereas a tetra (ethylene glycol) chain attached to



tris-alcohol core was terminated with a NH_3^+ charged group. Correspondingly, 32 chloride ions were solvated into our system to keep electrostatic balance and the force field of Cl^- was updated according Molinero's work using frcmod format file. QM calculations were also performed to obtain RESP charges of the modified group ($\text{NH}_3^+\text{CH}_2\text{OCH}_2\text{CH}_3$) using GAUSSIAN 09 packages⁴² at the MP2 level with cc-pvtz basis sets⁴³ as the left figure showed. Calculation of whole modified

arms was still undergoing conducted by Dr. Paramaswaran to tackle several emerging difficulties including charge distribution and adjustment of the multiplicities. The specific charge distributions for modified part are summarized in Table 4.1.

Atom	Modified Charges
N1	-0.38587157
C1	0.07378143
O1	-0.37430557
C2	0.16553943
C3	-0.97185657
H1	0.32455943
H2	0.32455943
H3	0
H4	0.15333543
H5	0.15333543
H6	0.20090743

H7	0.20090743
H8	0.43679443
H9	0.43679443
H10	0.43679443

Table 4.1 Modified RESP charges of terminated part of PEO arms

We still used GAFF to describe organic groups and solvent as well as TIP4P2005 to describe water model. 8000 water and 1500 toluene were solvated into the system.

4.2.2 Structural Results: Radius of Gyration

Treatment of adding charged NH_3^+ groups is just a minor alteration in terms of structure, but major alternation regarding with chemical functionalities. As table 4.2 indicating, overall cyclic polymer sizes were increasing after alternating ending group. As well backbones' R_g were increased too, but the observation of snapshots (Figure 4.3) indicated the backbone was stretched into an elliptical shape. The actual area of central space probably was smaller compared with original polymer. Alkyl arms in toluene solution didn't display difference between modified and original polymers with only 0.1 variance. Those arms in aqueous solution manifested expansion about 2.4 Å which is not surprising due to overall structure inflation. On the other hand, PEO arms' R_g of modified polymer

in both toluene and water solution were about 21 Å. Compared with the original polymer's results, the radii-of-gyration stretches about 2 Å. However, the structural change trend regarding varying polarity actually didn't exhibit any difference within modified and original polymer. Demonstrated by Table 4.2, what drew a difference was the extents of arms' retreating and advancing.

	polymer	backbone	alkyl arms	PEO arms
	(Å)	(Å)	(Å)	(Å)
cyclic in water (mod.)	18.4	10.3	18.8	21.9
cyclic in toluene (mod.)	19.7	10.2	23.7	21.3
cyclic in water	16.5	9.1	16.4	19.2
cyclic in toluene	18.9	9.2	23.8	19.4

Table 4.2 Average Radii of Gyration of the Modified and Original Cyclic Amphiphilic Polymers, Their Backbones, the Hydrophobic Alkyl Arms, and the Hydrophilic PEO Arms in water and Toluene at 300 K

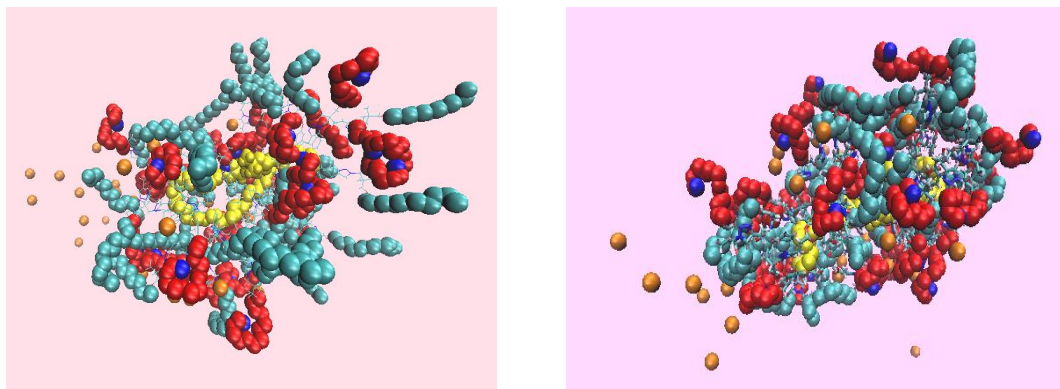


Figure 4.3 Demonstrating snapshots of modified cyclic polymer in toluene (left) and in water (right). The polymer backbone, alkyl side chains, and oligomeric PEO side chains are illustrated as the yellow, cyan, and red van der Waals surface. The modified heavy atom of NH_3^+ is illustrated with blue surface.

R_g distributions of the PEO, Alkyl, polymer and backbone in different polarity solvents were also summarized in Figure 4.4. Compared with original polymers' results in Figure 3.12, impressive variance was the overall distribution moved forward to the exterior area. The hydrocarbon backbone was buried beneath the side chain with slight advancing. Alkyl arms moved back and forth sensitive to the solvent's polarity. PEO arms' R_g on the other hand wasn't varying too much regarding polarity change. The charge group basically turned the neutral polymer to a polyelectrolyte. The overall inflation of polymer might be resulted from larger excluded volume of chains induced by the stronger polar segregation effect.

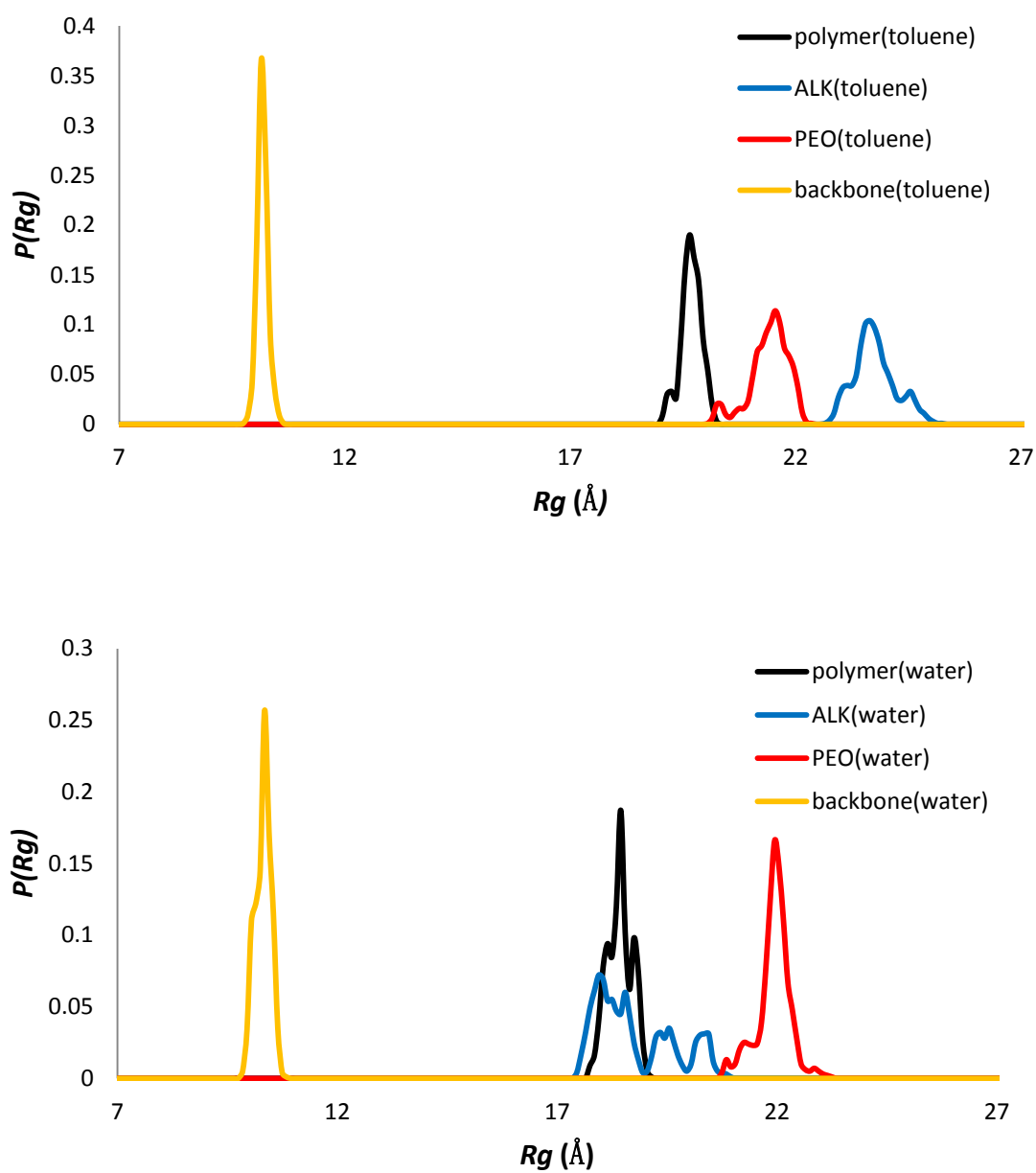


Figure 4.4 The radius-of-gyration distribution of modified cyclic polymer in toluene (above) and water (below)

4.2.3 Structural Results: Hydrogen Bonding Effect

One of the interesting observation from snapshots for this new modified polymer was ending group NH_3^+ bending over to form a "hook" structure. Therefore, we performed an analysis toward to the vector between last 3 heavy atoms (11~13 atoms of PEO arm) and last 4~6 heavy atoms (8~10 atoms of PEO arm). For the original tetra PEG oligomers, the average rotating angle is 89.83° in toluene and 66.03° respectively. For the modified oligomers by counting NH_3^+ as the last atom, the average rotating angle is 139.94° and 135.31° respectively. NH_3^+ group and closest ester group are bonded via hydrogen bonding. Such bending structures are not only found common in toluene, but also in water solution. Hypothetically, all the charged group of hydrophilic arms should be used to expel hydrophobic arms. However, the inclination to interact with the oxygen of ester group shielded some hydrophilic arms' expellment to some extent. Therefore, even though the uncompatibilities of amphiphilic arms was strengthened due to the stronger self - association of PEO arms, the dynamics of amphiphilic arms were also decreased due to the constraint of hydrogen bonding.

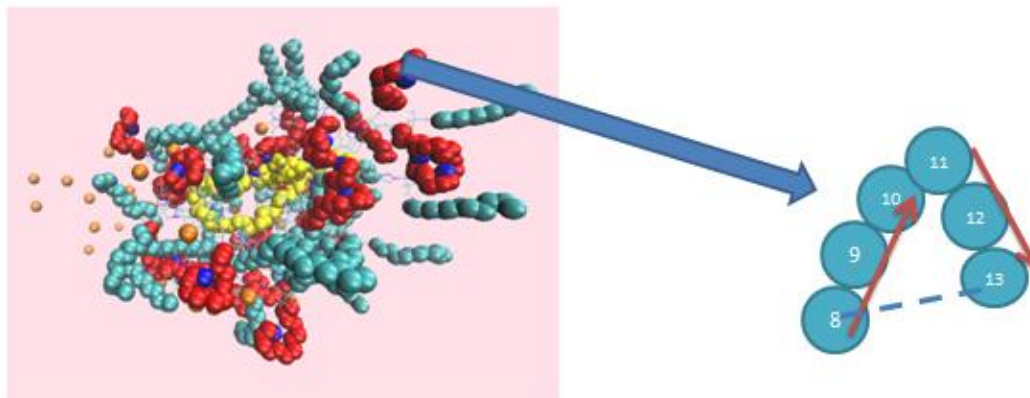
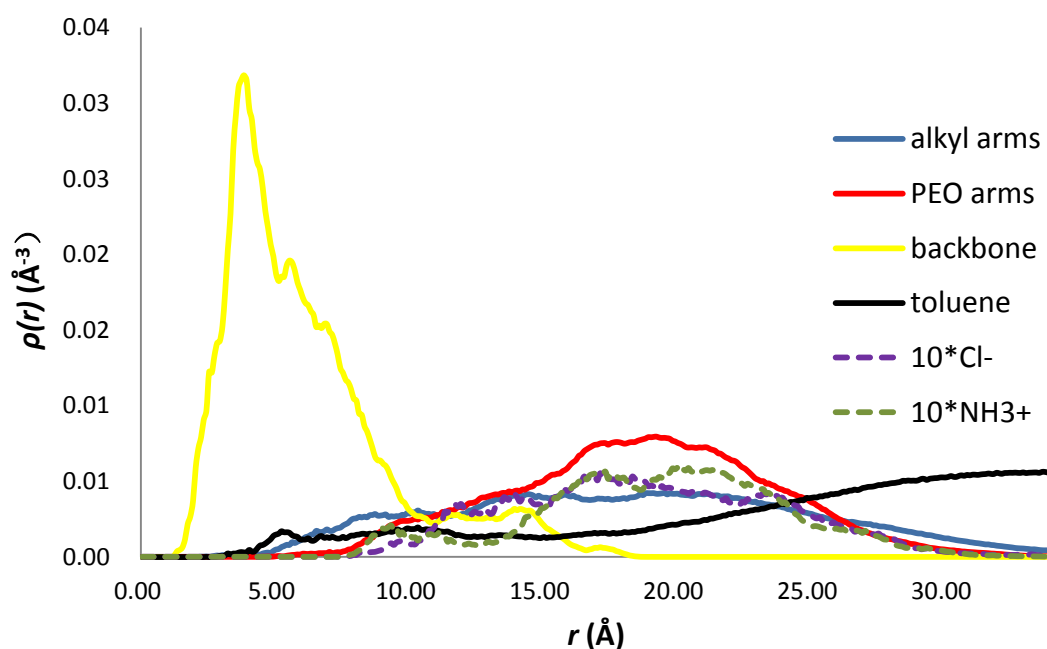


Figure 4.5 Rotating angles of two vectors were analyzed between the last 4 to 6 atoms and last 3 atoms. The blue dashed line manifested hydrogen bonding atoms

4.2.4 Structural Results: Density Distribution Function

Above results all suggested polymer's size inflation occurred as we modified the ending group of PEO oligomer to NH_3^+ . To discern interior molecular structure details clearly, density distribution function was further implemented to study interested components of polymers. Compared with 3.13, there were several obvious structural changes: Firstly, backbone's distribution was narrowed to sharper distribution toward inner place, suggesting backbone loop actually became smaller comparing with original distribution. Secondly, there was no distribution of alkyl arms and PEO arms nearby the center of polymer. The original prominent peaks of alkyl arms disappeared, replaced by a relative flat distribution both for polymer in water and toluene. PEO arms' distributions in water and toluene identically exhibited a shallow peak around 19 Å. However, PEO arms'

exterior distribution was prolonged to 28~30 Å after modification with the original PEO arms' distribution only reaching at about 25 ~28 Å. Both polar and non-polar olvents penetrated deeper. Especially the water penetration could reach to 5 Å which is quite departing from original phenomenon that cyclic polymer blocked the water penetrating at about 15 Å. Basically chloride ions' distribution superimposed with PEO arms' and most of ions were absorbed onto the polymer side. Under NH_3^+ strong attraction to chloride, Chlorides' distribution was influenced by NH_3^+ 's dynamics majorly but it was still perturbed under other atoms' influence such as oxygen of water, oxygen of tris-alcohol groups or nitrogen atoms in triazio groups.



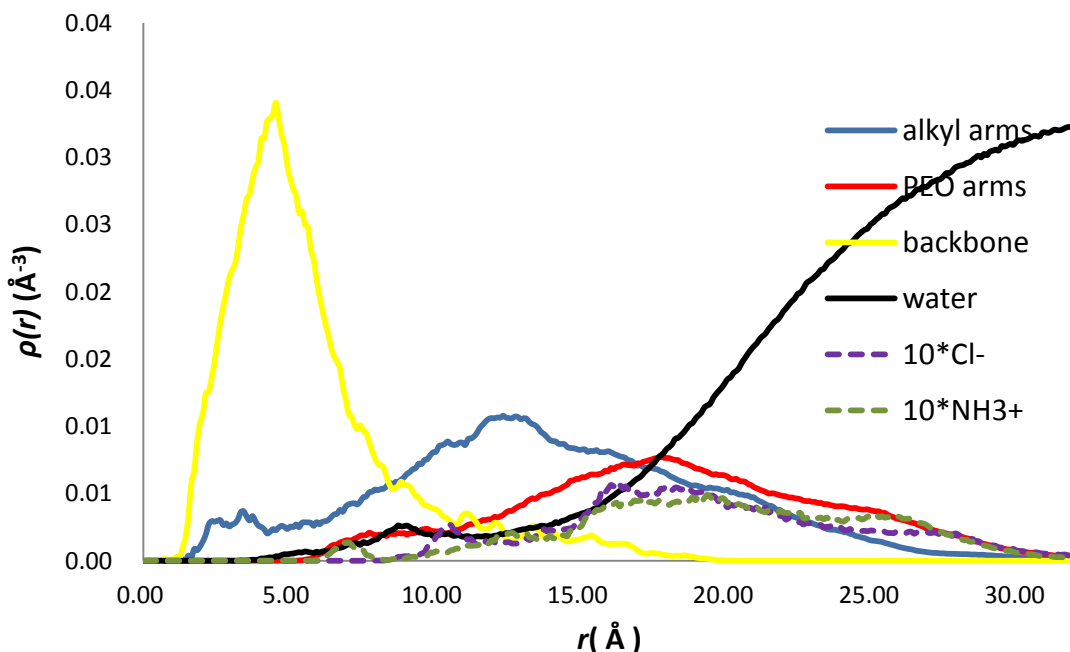


Figure 4.6 Heavy atom densities as function of distance from the cyclic polymer center-of-mass for the polymer backbone, alkyl arms, PEO arm unit, Chloride, NH_3^+ in toluene (top), in water (bottom). Figure symbols are defined in legends.

4.2.5 Structural Results: Instantaneous Liquid Surface

As demonstrated by Figure 4.6, further comparative analysis between the instantaneous liquid surface of modified cyclic polymer and the original cyclic polymer were implemented. Similarly, a smearing length λ 2.4 Å was assigned and cells at half of the solvent bulk density were considered as blocks of reference instantaneous density surface. PEO arms and Alkyl arms of new modified polymer uniformly extended to the longer distance distributions in either water (top Figure 4.6) or toluene (bottom Figure 4.6). As also indicated in Figure 3.17, minor difference was resulted from the distinction of linear

and cyclic topologies. Therefore, it's not surprising that the distributions of modified polymer were just slightly affected by the prolonged eclipsed topology.

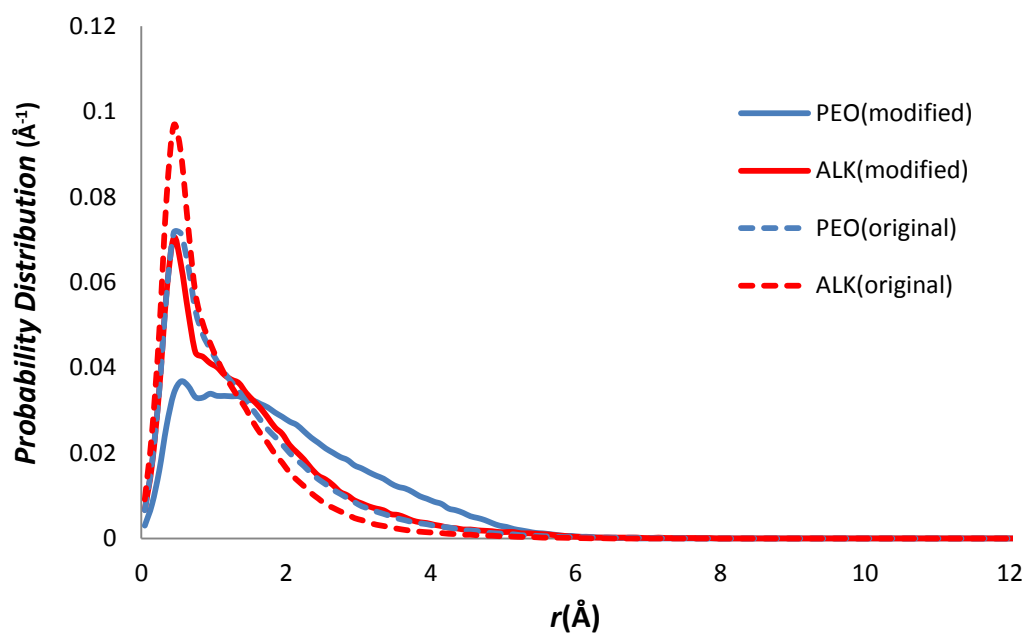
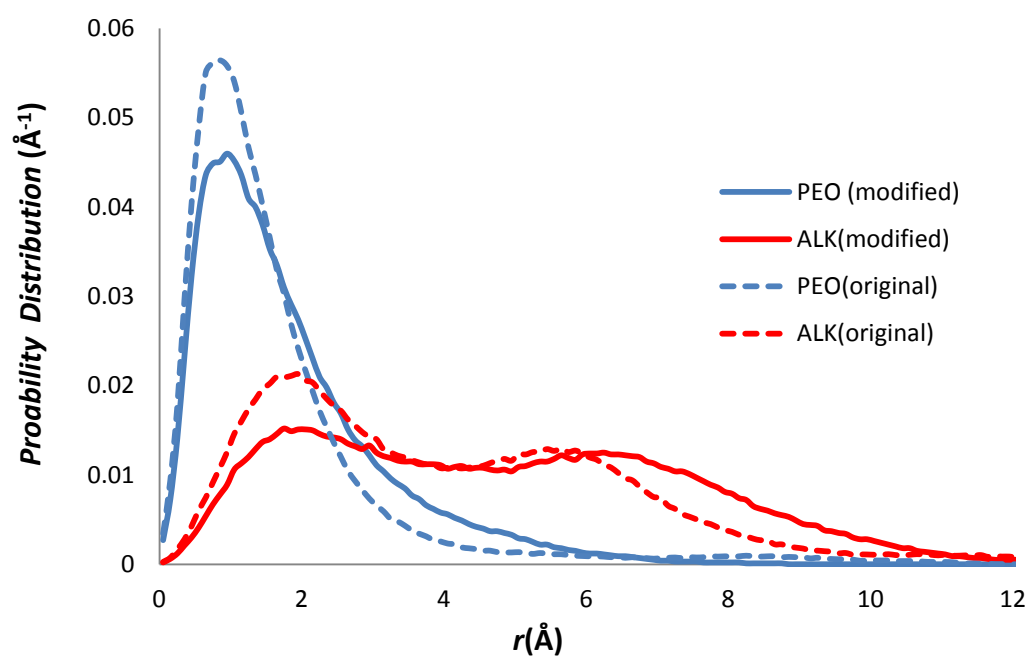


Figure 4.7 Probability distribution of distance for PEO (blue) and ALK (red): Top results are from cyclic polymer in water solution, bottom results are from cyclic polymer in a toluene solution.

Specifically speaking, the structural character of modified cyclic polymer in water manifested consistent features between modified and original one, with a twin peaking distribution of alkyl arms and sharp distribution of PEO arms nearby liquid interface. In water, the alkyl arms retreated more compared with the original alkyl distribution while the PEO arms' main distribution wasn't perturbed too much upon modifications. On the other hand, distribution of polymer in toluene exhibited more obvious distinction than original polymers. The original distribution rendered significant overlapping between PEO and alkyl arms. However, such overlapping distributions were took place by the separated ones for the modified polymers' alkyl arms and PEO arms. Especially the PEO arms were faded further from the liquid surface through the alkyl arms still occluded the position nearby the liquid interface. It's a remarking validation of our initial design idea that charged groups pended on the hydrophilic arms will lead stronger segregation of amphiphilic chains and affect the chemistry utterly with minor change of structure.

4.3 Conclusion

In this chapter, we generally reported an ongoing work that uses molecular simulation to test and validate a conceptual design of tailored polymer. The previous work of Chapter 3

provided a feasible strategy in tackling large macromolecules' sampling and exploring interested features. Hereby we performed simulations with adding terminated charged group NH_3^+ onto the hydrophilic arms of cyclic polymer as well as chloride ions into the existed system. We adopted same analysis methods to compare results from 20ns simulation of modified polymer with counter-parts of original PHS-yen polymer. Indicated by radius-of-gyration analysis, overall size of polymer as well as amphiphilic arms were all increased, but the modified polymers' preferences to various polarities beared no differneces. Density distribution function revealed several molecular details distinct from original template: 1. there were no amphiphilic arms reverting beneath backbone which was probably limited by the permittivity of the narrower backbone loop. 2. more solvents penetrated much deeper, suggesting that structure became relatively loose after introducing new charged group. 3. chloride ions' distribution closely coincided with the NH_3^+ heavy atoms' distribution, especially in the periphery area of polymers either in toluene or water. Instantaneous liquid surface analysis also revealed that minor difference of backbone didn't affect the basic orientation preference of amphiphilic arms. Ditributions of instantaneous liquid surface distance were faded to flatter distribution upon modifying the polymer. Especially PEO arms' distribution shrouded more under the instantaneous toluene surface, indicating occurrence of stronger segregation. According to our expectation, stronger segregation should result a more thorough inversion, however,

our observations were diverted from initial guess. One of the current problems is still the backbone's spatial allowance is limited due to the geometry constraints. High stiffness of hydrocarbon backbone as well as shorter chain length may lead such consequence. Hopefully convoluting of all the other schemes' results, a complete design scheme for improving the performance of interested polymeric micelles is able to be delivered.

Chapter 5

Conclusion and Future Work

As previous mentioned, the aim of our work is developing simulation as a powerful tool to recapture the thermal or pressure-responsive transition, to recognize mechanisms governing the material's hierarchical structure transition, to deliver sufficient molecular-level information for statistical mechanics theories' validation, to extend theoretical prediction for next-stage material improvement. In terms of single molecule perspective, we have basically built several technical schemes either through incorporating REDs technique or through force field's optimization. However, in terms of description of a real solution system consisting multiple macromolecules, atomistic simulations right now still confront enormous challenge. Multi-scale modeling is considered as an effective strategy to build a bridge spanning either between time scopes or length scopes as shown in Figure 5.1. In terms of our specific studied case, an atomistic level structural transition of unimolecular amphiphilic homopolymer regarding solvent polarity change has been able to be rendered through MD simulations. However,

if we anticipate to further probe self-assembly phenomenon of "real" polymer solution, keeping using atomistic

model to simulate multi-fold scaled-up system is not a practical solution. Applying martini model, which is a Coarse-Grained (CG) force field for biomolecular simulation, has been found to be a effective approach to overcome such system size barrier as well as reproduce attractive chemical specificities¹⁰⁶. Since growing number of MARTINI parameters of basic polymer systems such as polyethylene glycol (PEG)¹⁰⁷, polystyrene^{107, 108}, etc, have been derived, building a MARTINI model and performing CG simulation of our interested polymeric micelles' solution are able to be realized. Hopefully, applying martini model to simulate true polymer solution can resolve inter-molecular interaction within micelles intermediated with solvents. Moreover, such study is expected to produce more intuitively comparable results with experimental findings.

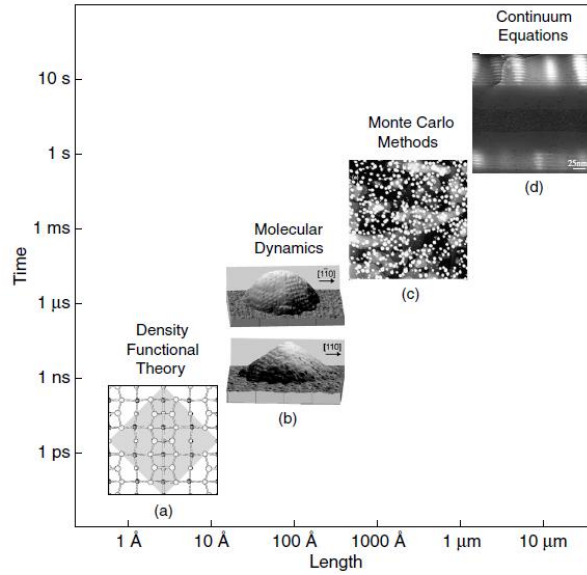


Figure 5.1 The hierarchy of modeling methods plot for the range of length and time scales illustrated with the multiscale phenomenology of quantum dots obtained from the heteroepitaxial growth of InAs on GaAs(001).

We also developed our own MD Simulation program LUDDITE which potentially is able to simulate amphiphilic polymeric system. It has been integrated with Berdensen barostat, Berdensen thermostat, neighbor-list algorithms, and harmonic bonding potential so far. One of the work done by LUDDITE was simulating a single chain polymer's self-assemble globular structure. Instead of 6-12 LJ potential, a m-n non-bonded potential was used to allow much more flexible parametrs' tuning as equation 5.1 indiated,

$$E_{pot} = -\frac{a}{r_s^m} + \frac{b}{r_s^n} \quad (5.1)$$

$$a_{ij} = \left(\frac{n}{m-n}\right) \left[\left(\frac{m}{n}\right)^{\frac{m}{m-n}}\right] \varepsilon \sigma^m \quad (5.2)$$

$$b_{ij} = \left(\frac{n}{m-n}\right) \left[\left(\frac{m}{n}\right)^{\frac{m}{m-n}}\right] \varepsilon \sigma^n \quad (5.3)$$

We can also split the potential into two part: attractive part and repulsive part.

$$\text{if } r < r_{mn}, \quad E_1 = E_{pot} + \varepsilon ; E_2 = -\varepsilon + esh \quad (\text{repulsive})$$

$$\text{if } r > r_{mn}, \quad E_1 = 0 ; E_2 = E_{pot} + esh \quad (\text{attractive})$$

$$\text{in which , } r_{mn} = r_0 + \left[\left(\frac{m}{n}\right)^{\frac{1}{m-n}}\right] \sigma , \quad esh = -\frac{a}{r_{cut}^m} + \frac{b}{r_{cut}^n}$$

Then we introduce a lamada parameter to adjust the potential from Lenard-Jones Potntail to WCA potential according to equation $E_{ij} = E_1 + \lambda E_2$. When $\lambda = 0$, equation 5.1 is governed by L-J potential; When $\lambda = 1$, that is governed by Week-Chadler Anderson potential. As Figure 5.2 shows, two type intermolecular interactions were assigned to construct a "symbolized" amphiphilic unit, with the red beads symbolizing atoms under L-J potential and the blue beads representing the atoms under WCA potential. Driven by the interaction of L-J potential, chain molecule tended to self-reorganize to form global inwardly. WCA potential on the other hand just sustained other atoms non-superimposed. We have tested the elasticity of harmonic bonding's influence (K_{harmonic}) to the overall conformation of single chain like Figure 5.2 showed. Results indicated stronger elasticity was enable to stretch the polymer chain until conformation reached a equilibrated state.

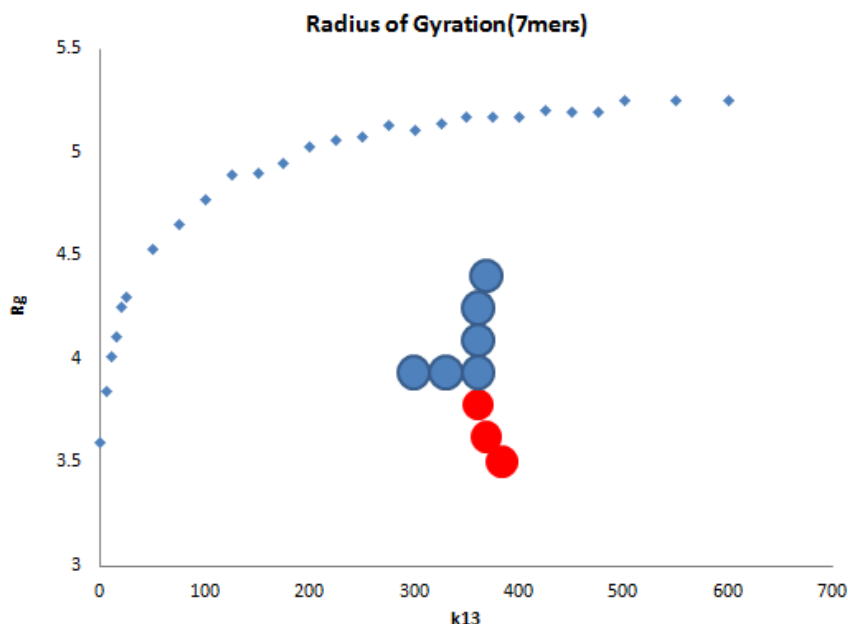


Figure 5.2 The Radius of Gyration as a function of harmonic potential strength for single chain 7mers polymer. The central picture demonstrated the structure of amphiphilic polymer, with red balls representing atoms governed by full interacting L-J potential and blue ones representing atoms governed by WCA potential.

In the next-stage research, we plan to develop LUDDITE to simulate more complex system such as diblock or tri-block polymer fluid consisting 400-500 chains, in which we can tune the potential and observed the micellar structure and dynamics using such Coarsed-Grained MD Algorithms. Water are going to be incorporated with LUDDITE as well as Ewald Algorithms including long-range electrostatic interaction. Hopefully, LUDDITE can be developed to serve a wider range of thermodynamics studies by adding more features and functions.

List of References

1. Bishop, K. J. M.; Wilmer, C. E.; Soh, S.; Grzybowski, B. A., *Small* **2009**, 5 (14), 1600-1630.
2. Vvedensky, D. D., *Journal of Physics-Condensed Matter* **2004**, 16 (50), R1537-R1576.
3. Zhang, S. G., *Biotechnology Advances* **2002**, 20 (5-6), 321-339.
4. Palma, C. A.; Cecchini, M.; Samori, P., *Chemical Society Reviews* **2012**, 41 (10), 3713-3730.
5. Nahmad-Molinari, Y.; Ruiz-Suarez, J. C., *Physical Review Letters* **2002**, 89 (26).
6. Olson, A. J.; Hu, Y. H. E.; Keinan, E., *Proceedings of the National Academy of Sciences of the United States of America* **2007**, 104 (52), 20731-20736.
7. Bucknall, D. G.; Anderson, H. L., *Science* **2003**, 302 (5652), 1904-1905.
8. Taylor, R. D.; Jewsbury, P. J.; Essex, J. W., *Journal of Computer-Aided Molecular Design* **2002**, 16 (3), 151-166.
9. Bertsimas, D.; Tsitsiklis, J., *Statistical Science* **1993**, 8 (1), 10-15.
10. Rossky, P. J., *Theoretical Chemistry Accounts* **2000**, 103 (3-4), 263-264.
11. Dickman, R.; Hall, C. K., *Journal of Chemical Physics* **1986**, 85 (7), 4108-4115.
12. Ghonasgi, D.; Chapman, W. G., *Molecular Physics* **1994**, 83 (1), 145-158.
13. Ashbaugh, H. S.; Paulaitis, M. E., *Industrial & Engineering Chemistry Research* **2006**, 45 (16), 5531-5537.
14. Nagarajan, R.; Ruckenstein, E., *Langmuir* **1991**, 7 (12), 2934-2969.
15. Hummer, G.; Garde, S.; Garcia, A. E.; Paulaitis, M. E.; Pratt, L. R., *Journal of Physical Chemistry B* **1998**, 102 (51), 10469-10482.
16. Hummer, G.; Garde, S.; Garcia,

A. E.; Pohorille, A.; Pratt, L. R., *Proceedings of the National Academy of Sciences of the United States of America* **1996**, 93 (17), 8951-8955.

17. Hummer, G.; Garde, S.; Garcia, A. E.; Pratt, L. R., *Chemical Physics* **2000**, 258 (2-3), 349-370.

18. Ashbaugh, H. S.; Garde, S.; Hummer, G.; Kaler, E. W.; Paulaitis, M. E., *Biophysical Journal* **1999**, 77 (2), 645-654.

19. Paschek, D., *Journal of Chemical Physics* **2004**, 120 (14), 6674-6690.

20. Krouskop, P. E.; Madura, J. D.; Paschek, D.; Krukau, A., *Journal of Chemical Physics* **2006**, 124 (1).

21. Garde, S.; Ashbaugh, H. S., *Journal of Chemical Physics* **2001**, 115 (2), 977-982.

22. Paschek, D., *Zeitschrift Fur Physikalische Chemie-International Journal of Research in Physical Chemistry & Chemical Physics* **2009**, 223 (9), 1091-1104.

23. Dyer, P. J.; Docherty, H.; Cummings, P. T., *Journal of Chemical Physics* **2008**, 129 (2).

24. Abascal, J. L. F.; Vega, C., *Journal of Chemical Physics* **2005**, 123 (23).

25. Ashbaugh, H. S.; Collett, N. J.; Hatch, H. W.; Staton, J. A., *Journal of Chemical Physics* **2010**, 132 (12).

26. Horn, H. W.; Swope, W. C.; Pitera, J. W.; Madura, J. D.; Dick, T. J.; Hura, G. L.; Head-Gordon, T., *Journal of Chemical Physics* **2004**, 120 (20), 9665-9678.

27. Docherty, H.; Galindo, A.; Vega, C.; Sanz, E., *Journal of Chemical Physics* **2006**, 125 (7).

28. Chapman, W. G.; Gubbins, K. E.; Jackson, G.; Radosz, M., *Fluid Phase Equilibria* **1989**, 52, 31-38.

29. Martin, M. G.; Siepmann, J. I., *Journal of Physical Chemistry B* **1998**, 102 (14), 2569-2577.

30. Hess, B.; Kutzner, C.; van der Spoel, D.; Lindahl, E., *Journal of Chemical Theory and Computation* **2008**, 4 (3), 435-447.
31. Nose, S., *Molecular Physics* **1984**, 52 (2), 255-268.
32. Parrinello, M.; Rahman, A., *Journal of Applied Physics* **1981**, 52 (12), 7182-7190.
33. Darden, T.; York, D.; Pedersen, L., *Journal of Chemical Physics* **1993**, 98 (12), 10089-10092.
34. Martin, M. G.; Siepmann, J. I., *Journal of Physical Chemistry B* **1999**, 103 (21), 4508-4517.
35. Essmann, U.; Perera, L.; Berkowitz, M. L.; Darden, T.; Lee, H.; Pedersen, L. G., *Journal of Chemical Physics* **1995**, 103 (19), 8577-8593.
36. Beutler, T. C.; Mark, A. E.; Vanschaik, R. C.; Gerber, P. R.; Vangunsteren, W. F., *Chemical Physics Letters* **1994**, 222 (6), 529-539.
37. Konrad, O.; Lankau, T., *Journal of Physical Chemistry B* **2005**, 109 (49), 23596-23604.
38. Chandler, D.; Weeks, J. D.; Andersen, H. C., *Science* **1983**, 220 (4599), 787-94.
39. Ben-Amotz, D.; Stell, G., *Journal of Physical Chemistry B* **2004**, 108 (21), 6877-6882.
40. Wilhelm, E.; Battino, R.; Wilcock, R. J., *Chemical Reviews* **1977**, 77 (2), 219-262.
41. Plyasunova, N. V.; Plyasunov, A. V.; Shock, E. L., *International Journal of Thermophysics* **2004**, 25 (2), 351-360.
42. Sangwai, A. V.; Ashbaugh, H. S., *Industrial & Engineering Chemistry Research* **2008**, 47 (15), 5169-5174.
43. Lazaridis, T.; Paulaitis, M. E., *Journal of Physical Chemistry* **1994**, 98 (2), 635-642.
44. Stuart, M. A. C.; Huck, W. T. S.; Genzer, J.; Muller, M.; Ober, C.; Stamm, M.; Sukhorukov, G. B.; Szleifer, I.; Tsukruk, V. V.; Urban, M.; Winnik, F.; Zauscher, S.; Luzinov, I.; Minko, S., *Nature Materials* **2010**, 9 (2), 101-113.
45. Liu, F.; Urban, M. W., *Progress in Polymer Science* **2010**, 35 (1-2), 3-23.

46. Park, T. G.; Jeong, J. H.; Kim, S. W., *Advanced Drug Delivery Reviews* **2006**, 58 (4), 467-486.
47. Chaterji, S.; Kwon, I. K.; Park, K., *Progress in Polymer Science* **2007**, 32 (8-9), 1083-1122.
48. Hao, T., *Advanced Materials* **2001**, 13 (24), 1847-+.
49. Mather, P. T.; Luo, X. F.; Rousseau, I. A., *Annual Review of Materials Research* **2009**, 39, 445-471.
50. Liu, R. X.; Fraylich, M.; Saunders, B. R., *Colloid and Polymer Science* **2009**, 287 (6), 627-643.
51. Qian, C. B.; Mumby, S. J.; Eichinger, B. E., *Macromolecules* **1991**, 24 (7), 1655-1661.
52. Otake, K.; Inomata, H.; Konno, M.; Saito, S., *Macromolecules* **1990**, 23 (1), 283-289.
53. Sun, S. T.; Hu, J.; Tang, H.; Wu, P. Y., *Journal of Physical Chemistry B* **2010**, 114 (30), 9761-9770.
54. Wu, C.; Wang, X. H., *Physical Review Letters* **1998**, 80 (18), 4092-4094.
55. Graziano, G., *International Journal of Biological Macromolecules* **2000**, 27 (1), 89-97.
56. Okada, Y.; Tanaka, F., *Macromolecules* **2005**, 38 (10), 4465-4471.
57. Tamai, Y.; Tanaka, H.; Nakanishi, K., *Macromolecules* **1996**, 29 (21), 6761-6769.
58. Walter, J.; Sehart, J.; Vrabec, J.; Hasse, H., *Journal of Physical Chemistry B* **2012**, 116 (17), 5251-5259.
59. Tucker, A. K.; Stevens, M. J., *Macromolecules* **2012**, 45 (16), 6697-6703.
60. Deshmukh, S. A.; Sankaranarayanan, S. K. R. S.; Suthar, K.; Mancini, D. C., *Journal of Physical Chemistry B* **2012**, 116 (9), 2651-2663.
61. Hess, B., *Abstracts of Papers of the American Chemical Society* **2009**, 237.

62. Berendsen, H. J. C.; Grigera, J. R.; Straatsma, T. P., *Journal of Physical Chemistry* **1987**, *91* (24), 6269-6271.
63. Jorgensen, W. L.; Tiradorives, J., *Journal of the American Chemical Society* **1988**, *110* (6), 1657-1666.
64. Nose, S., *Journal of Chemical Physics* **1984**, *81* (1), 511-519.
65. Kuckling, D.; Adler, H. J. P.; Arndt, K. F.; Ling, L.; Habicher, W. D., *Macromolecular Chemistry and Physics* **2000**, *201* (2), 273-280.
66. Munoz, V.; Eaton, W. A., *Proceedings of the National Academy of Sciences of the United States of America* **1999**, *96* (20), 11311-11316.
67. Shan, J.; Zhao, Y. M.; Granqvist, N.; Tenhu, H., *Macromolecules* **2009**, *42* (7), 2696-2701.
68. Gong, K.; Marshall, B. D.; Chapman, W. G., *Journal of Chemical Physics* **2013**, *139* (9).
69. Jones, M. C.; Leroux, J. C., *European Journal of Pharmaceutics and Biopharmaceutics* **1999**, *48* (2), 101-111.
70. Kataoka, K.; Harada, A.; Nagasaki, Y., *Advanced Drug Delivery Reviews* **2012**, *64*, 37-48.
71. Miyata, K.; Christie, R. J.; Kataoka, K., *Reactive & Functional Polymers* **2011**, *71* (3), 227-234.
72. Lee, C. C.; MacKay, J. A.; Frechet, J. M. J.; Szoka, F. C., *Nature Biotechnology* **2005**, *23* (12), 1517-1526.
73. Laurent, B. A.; Grayson, S. M., *Polymer Chemistry* **2012**, *3* (7), 1846-1855.
74. Wang, Y.; Grayson, S. M., *Advanced Drug Delivery Reviews* **2012**, *64* (9), 852-865.
75. Basu, S.; Vutukuri, D. R.; Shyamroy, S.; Sandanaraj, B. S.; Thayumanavan, S., *Journal of the American Chemical Society* **2004**, *126* (32), 9890-9891.
76. Wang, Y.; Alb, A. M.; He, J. B.; Grayson, S. M., *Polymer Chemistry* **2014**, *5* (2), 622-629.

77. Lee, A. J.; Rick, S. W., *Journal of Chemical Physics* **2009**, *131* (17).
78. Salomon-Ferrer, R.; Case, D. A.; Walker, R. C., *Wiley Interdisciplinary Reviews-Computational Molecular Science* **2013**, *3* (2), 198-210.
79. Earl, D. J.; Deem, M. W., *Physical Chemistry Chemical Physics* **2005**, *7* (23), 3910-3916.
80. Car, R.; Parrinello, M., *Physical Review Letters* **1985**, *55* (22), 2471-2474.
81. Rick, S. W.; Stuart, S. J.; Bader, J. S.; Berne, B. J., *Journal of Molecular Liquids* **1995**, *65-6*, 31-40.
82. Hoover, W. G., *Physical Review A* **1985**, *31* (3), 1695-1697.
83. Wang, J. M.; Wolf, R. M.; Caldwell, J. W.; Kollman, P. A.; Case, D. A., *Journal of Computational Chemistry* **2005**, *26* (1), 114-114.
84. Wang, J. M.; Hou, T. J., *Journal of Computational Chemistry* **2011**, *32* (16), 3505-3519.
85. Caleman, C.; van Maaren, P. J.; Hong, M. Y.; Hub, J. S.; Costa, L. T.; van der Spoel, D., *Journal of Chemical Theory and Computation* **2012**, *8* (1), 61-74.
86. Siu, S. W. I.; Vacha, R.; Jungwirth, P.; Bockmann, R. A., *Journal of Chemical Physics* **2008**, *128* (12).
87. Pophristic, V.; Vemparala, S.; Ivanov, I.; Liu, Z. W.; Klein, M. L.; DeGrado, W. F., *Journal of Physical Chemistry B* **2006**, *110* (8), 3517-3526.
88. Rick, S. W., *Journal of Chemical Physics* **2007**, *126* (5).
89. Willard, A. P.; Chandler, D., *Journal of Physical Chemistry B* **2010**, *114* (5), 1954-1958.
90. Swope, W. C.; Carr, A. C.; Parker, A. J.; Sly, J.; Miller, R. D.; Rice, J. E., *Journal of Chemical Theory and Computation* **2012**, *8* (10), 3733-3749.
91. Gilson, M. K.; Given, J. A.; Bush, B. L.; McCammon, J. A., *Biophysical Journal* **1997**, *72* (3), 1047-1069.

92. Brooijmans, N.; Kuntz, I. D., *Annual Review of Biophysics and Biomolecular Structure* **2003**, 32, 335-373.
93. Wlodawer, A.; Vondrasek, J., *Annual Review of Biophysics and Biomolecular Structure* **1998**, 27, 249-284.
94. Carlson, H. A.; Masukawa, K. M.; Rubins, K.; Bushman, F. D.; Jorgensen, W. L.; Lins, R. D.; Briggs, J. M.; McCammon, J. A., *Journal of Medicinal Chemistry* **2000**, 43 (11), 2100-2114.
95. Hussain, F.; Hojjati, M.; Okamoto, M.; Gorga, R. E., *Journal of Composite Materials* **2006**, 40 (17), 1511-1575.
96. Yang, L.; Fishbine, B. H.; Migliori, A.; Pratt, L. R., *Journal of the American Chemical Society* **2009**, 131 (34), 12373-12376.
97. Wanjari, P. P.; Sangwai, A. V.; Ashbaugh, H. S., *Physical Chemistry Chemical Physics* **2012**, 14 (8), 2702-2709.
98. Fiore, A.; Venkateshwaran, V.; Garde, S., *Langmuir* **2013**, 29 (25), 8017-8024.
99. Karatasos, K., *Journal of Physical Chemistry B* **2013**, 117 (8), 2564-2575.
100. Ballauff, M.; Likos, C. N., *Angewandte Chemie-International Edition* **2004**, 43 (23), 2998-3020.
101. Discher, D. E.; Ortiz, V.; Srinivas, G.; Klein, M. L.; Kim, Y.; David, C. A.; Cai, S. S.; Photos, P.; Ahmed, F., *Progress in Polymer Science* **2007**, 32 (8-9), 838-857.
102. Srinivas, G.; Discher, D. E.; Klein, M. L., *Nature Materials* **2004**, 3 (9), 638-644.
103. Wang, Y. L.; Li, B.; Zhou, Y. F.; Lu, Z. Y.; Yan, D. Y., *Soft Matter* **2013**, 9 (12), 3293-3304.
104. MacKerell, A. D.; Bashford, D.; Bellott, M.; Dunbrack, R. L.; Evanseck, J. D.; Field, M. J.; Fischer, S.; Gao, J.; Guo, H.; Ha, S.; Joseph-McCarthy, D.; Kuchnir, L.; Kuczera, K.; Lau, F. T. K.; Mattos, C.; Michnick, S.; Ngo, T.; Nguyen, D. T.; Prodhom, B.; Reiher, W. E.; Roux, B.; Schlenkrich, M.; Smith, J. C.; Stote, R.; Straub, J.; Watanabe, M.; Wiorkiewicz-Kuczera, J.; Yin, D.; Karplus, M., *Journal of Physical Chemistry B* **1998**, 102 (18), 3586-3616.

105. Matsen, M. W.; Bates, F. S., *Macromolecules* **1996**, 29 (4), 1091-1098.
106. Marrink, S. J.; Tieleman, D. P., *Chemical Society Reviews* **2013**, 42 (16), 6801-6822.
107. Lee, H.; de Vries, A. H.; Marrink, S. J.; Pastor, R. W., *Journal of Physical Chemistry B* **2009**, 113 (40), 13186-13194.
108. Rossi, G.; Monticelli, L.; Puisto, S. R.; Vattulainen, I.; Ala-Nissila, T., *Soft Matter* **2011**, 7 (2), 698-708.

Biography

Lixin Liu was born in Fuxin city of Liaoning province in China on October 17th 1984. In September 1998, he moved to Dalian city with family and attended the 6th Middle School of Dalian Developing District. In September 2001, he attended the 8th High School of Dalian City, where he completed his high school educations.

Lixin was admitted by Dalian University of Technology in September 2004, major in Chemical Engineering and English. He obtained a double major degree and student scholarships for excellent organization of class activities. In 2009, he joined Tulane University and started pursuing his Ph.D. degree in chemical engineering. In 2010, he joined Ashbaugh's Lab and worked under supervision of Prof. Henry S. Ashbaugh. His research focus was using Molecular Dynamics Simulation to study self-assemble polymeric materials and corresponding thermodynamics and statistical mechanics theories. He has completed three research projects and has authored in 2 peer-reviewed journals. He has presented his research results in 2012 and 2013 AIChE meetings and he was awarded for 2011 IBM Ph.D fellowship.